The PREFOS Project

Fiber optic monitoring system for prefabricated buildings

C. Mazzotta, M. A. Caponero, D. Lavorato, M. Capasso, A. Castaldo,
P. Clemente, R. Darban, C. Nuti, P. Parvanhero, A. Polimadei, G. Terranova

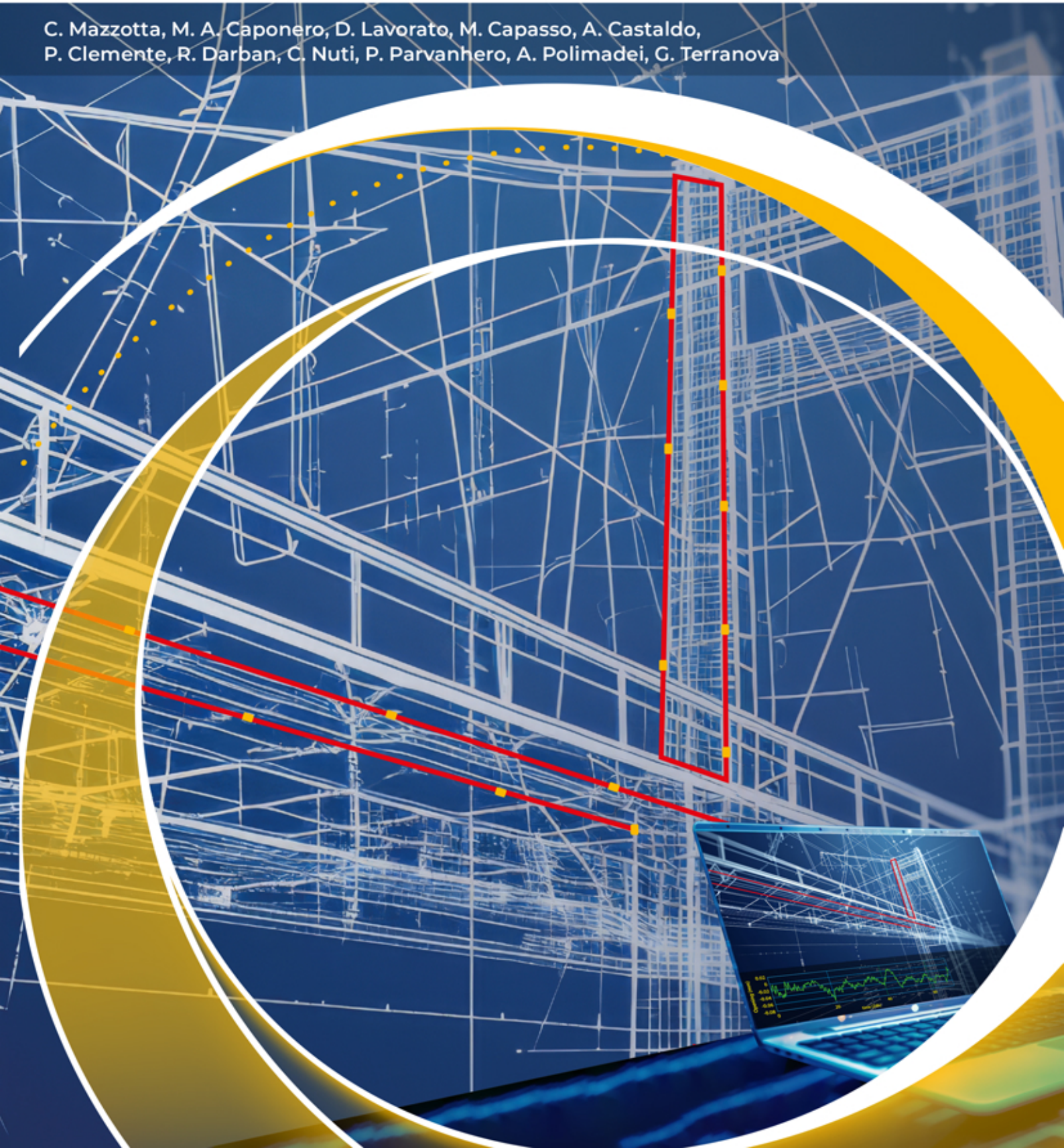

Research, Development and Innovation Project

PREFOS

Fiber optic monitoring system for prefabricated buildings

ENEA, ITALIAN NATIONAL AGENCY FOR NEW TECHNOLOGIES, ENERGY AND SUSTAINABLE ECONOMIC DEVELOPMENT.
FUSION AND TECHNOLOGY FOR NUCLEAR SAFETY AND SECURITY DEPARTMENT (NUC), PHYSICAL TECHNOLOGIES FOR SAFETY AND HEALTH DIVISION, PHOTONICS MICRO AND NANOSTRUCTURES LABORATORY.
DEPARTMENT OF SUSTAINABILITY, CIRCULARITY AND ADAPTATION TO CLIMATE CHANGE OF PRODUCTION AND TERRITORIAL SYSTEMS (SSPT).

DEPARTMENT OF ARCHITECTURE, UNIVERSITY OF ROMA TRE, ROME, ITALY

PARTNER Coordinator: ENEA

Michele Arturo Caponero, Antonio Castaldo, Paolo Clemente, Cristina Mazzotta, Andrea Polimadei, Gaetano Terranova
ENEA, C.R. Frascati, Frascati (RM), Italy

Davide Lavorato, Monica Capasso, Reza Darban, Camillo Nuti, Parsa Parvanhero
Department of Architecture, University of Roma Tre, Rome, Italy

Acknowledgments
Financial support for the research was receipt by FESR Fondo Europeo di Sviluppo Regionale - Programma Operativo Regione Lazio

Cover graphic design: Flavio Miglietta

Printed in September 2024

ISBN: 978-88-8286-476-7

Table of Contents

Introduction

Structural health monitoring (SHM) is a crucial aspect of understanding the safety of in-service civil engineering structures (Ferdinand 2014). Real-time monitoring offers an effective solution for the timely detection of defects and structural damages, facilitating focused routine maintenance and mitigating the need for costly extraordinary structural repairs. While various technologies have been developed to monitor structural safety, identifying and quantifying anomalies in different materials, many of them exhibit high intrusiveness and sensitivity to electromagnetic interferences.

Furthermore, the installation of multiple sensors in buildings and infrastructures is often required to establish an effective detection system, adding complexity. Therefore, a more convenient approach is to implement a sensor monitoring system during the industrial production of pre-cast reinforced concrete (RC) structures. Embedding sensors in pre-cast beams, columns, etc., during construction enables quality control, aiding in the early detection of defects that may compromise load capacity and durability.

An additional noteworthy aspect is that embedding sensors in pre-cast processes facilitates continuous monitoring throughout the serviceability life of structures and infrastructures. Consequently, this study aims to develop a solution for self-monitoring pre-cast RC beams, enabling the control and notification of damages. This approach also proves valuable for assessing the quality of structural elements in advance. To address issues related to intrusiveness and electromagnetic interference, the research project employs fiber optical systems (FOS), utilizing quasi-distributed Fiber Bragg Grating (FBG) technology sensors.

FBG sensors are well-suited for both static and dynamic measurements, allowing for the monitoring of strains, displacements, and temperature variations. The Bragg Grating within the fiber makes it sensitive to various parameters, akin to those observed by point optical sensors.

The concept of 'self-monitoring' emphasizes the benefits derived from integrating quasi-distributed FBG sensors into pre-built RC beams. The sole requirement for their Structural Health Monitoring (SHM) system is to connect the pre-planned wiring of optical sensors to optical interrogators for temperature, static, and dynamic measurements. This approach ensures that the final precast elements are inherently ready for monitoring at the construction site, eliminating the need for subsequent instrumentation steps.

The Implementation of the PREFOS Project

The PREFOS Project is a Regional Research initiative based in the Latium Region, Italy, supported by the European Regional Development Fund POR 2014-2020. The project involves collaboration with various partners, including the University of Roma Tre-Department of Architecture, ENEA C.R., and MAGNETTI Building S.p.a.

The University of Roma Tre, specifically the Department of Architecture located in Rome, plays a crucial role in the project by providing a structural laboratory essential for the development and testing of certain aspects. ENEA, identified as the National Agency for New Technologies, Energy and Sustainable Economic Development, is a public body dedicated to research, technological innovation, and the provision of advanced services in the fields of energy, environment, and sustainable economic development.

MAGNETTI Building S.p.a., a construction company situated in northern Italy near Bergamo, focuses on finding solutions through in-depth studies for suitable and more complex architectural structures. Additionally, the company's scope of activities extends to the recovery and redevelopment of existing structures.

The collaboration of these diverse entities contributes to the comprehensive design of a self-monitoring precast pre-stressed RC beam within the PREFOS Project.

The project involves testing the FBG optical technology and its application. Optical sensors will be embedded in the concrete section and will monitor steel reinforcing bars, facilitated by Polyester smart saddles instrumented with FBG sensors securely attached to them.

Fiber Bragg Grating principles

A Fiber Bragg Grating (FBG) is an optical sensor technology created by exposing a short segment (typically 100 to 150 mm) of the optical fiber's core to a specific pattern of ultraviolet (UV) light. During this exposure, the refractive index of the core undergoes periodic modification, forming a diffraction grating known as a Bragg grating. When broadband light is input through the grating, a specific wavelength is reflected (see Figure 1).

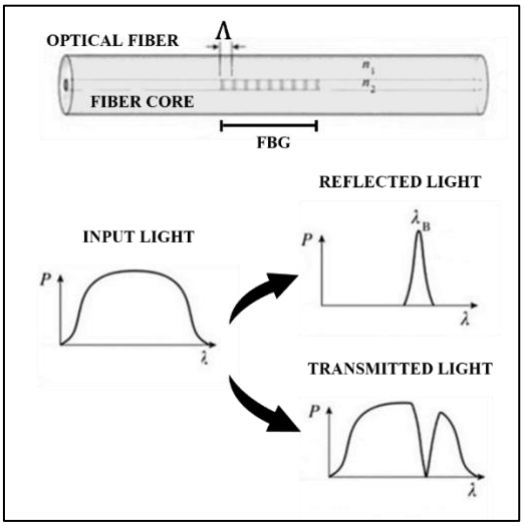

Figure 1. FBG principles

This reflected wavelength is referred to as the "Bragg Wavelength," while the remaining wavelengths continue to travel through the fiber and grating region (Keiser 2003; Kashyap 2009). The central Bragg wavelength adheres to the Bragg condition, which can be expressed as:

$$\lambda_B = 2\, n_{eff}\, \Lambda \qquad (1)$$

where λ_B is the central wavelength of the FBG sensor, n_{eff} is the effective refractive index and Λ is the grating period. An FBG spectrum displayed by an optical interrogator is shown in Figure 2.

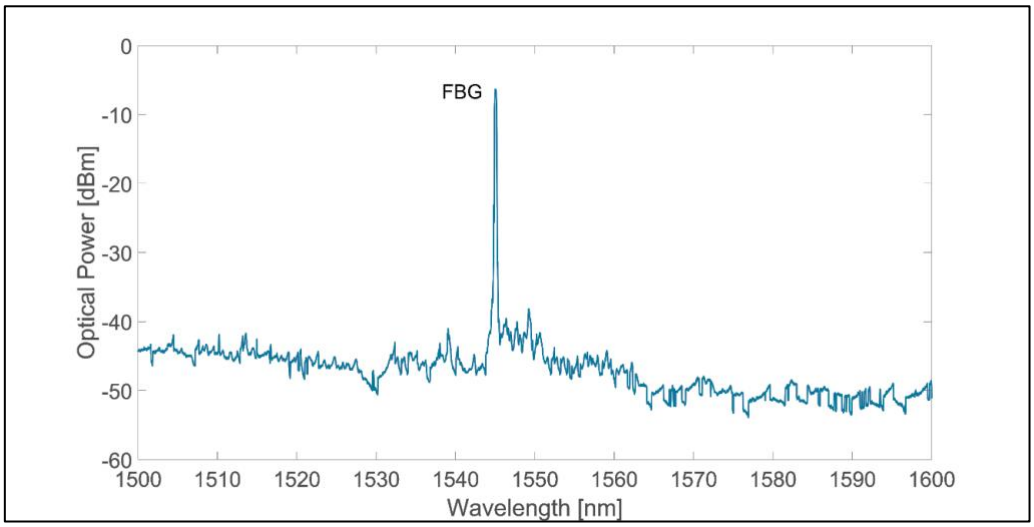

Figure 2. FBG spectrum shown by interrogator.

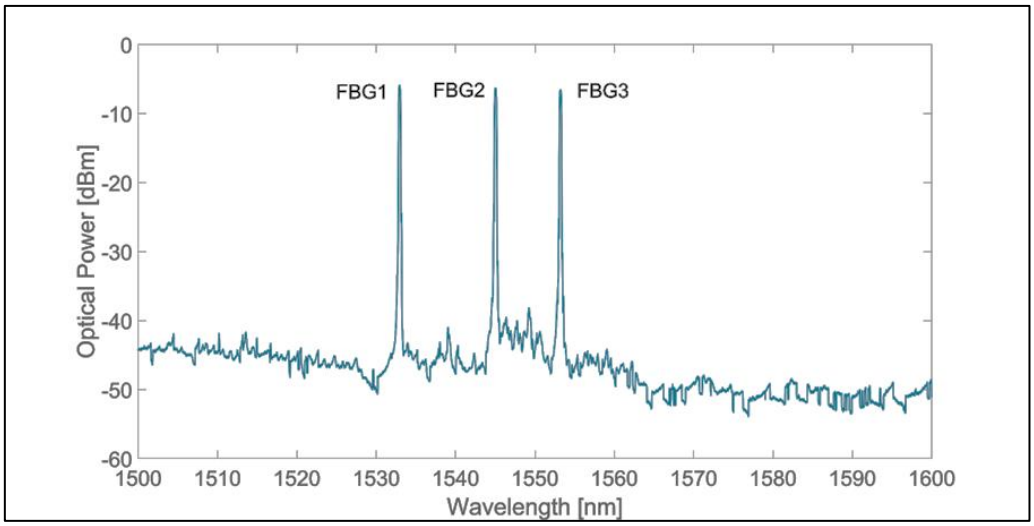

Figure 3. Spectrum of three Fiber Bragg Gratings connected in series on the same optical fibre cable

The spacing between each grating (Λ) undergoes changes in response to alterations in temperature and strain on the fiber. Consequently, there is a shift in the Bragg wavelength of the FBG sensor. The variations in the Bragg wavelength (ΔλB) facilitate the monitoring and detection of changes in strain and temperature parameters.

Utilizing multiplexing technology, it is possible to connect more than one FBG sensor in series on the same optical cable. Each sensor can be identified by its specific Bragg wavelength (λB1, λB2, …, λBn) when interrogated by an interrogator. Figure 3 illustrates the spectrum of three FBGs connected in series.

Furthermore, quasi-distributed Fiber Bragg Grating optical sensors are capable of high-speed acquisitions, allowing them to measure strains and temperature variations dynamically. They are suitable for both static and dynamic measurements, with a strain resolution of about 0.1 µm/m and a temperature resolution of approximately 0.01°C (Ferdinand P. 2014).

Steel strand monitoring by FBG

Over the last two decades, numerous applications of optical fiber sensors have been developed for monitoring structures (Barrias, Casas, & Villalba, 2016; Berrocal, Fernandez, Bado, Casas, & Rempling, 2021; Broth & Hoult, 2020; Deng & Cai, 2007; Uva, Porco, Fiore, & Porco, 2014). FBGs are a valuable choice for structural health monitoring of civil structures as they offer a small size, high accuracy, high acquisition rate and a broad operational temperature and strain range. What makes FBGs more valuable is their capacity to transmit signals over extended distances while isolated by electromagnetic and radio frequency interference (Deng & Cai, 2007). In addition, multiple sensors can be integrated along a single fiber. Notably, FBGs are well-suited for internal strain measurements as they impose minimal impact on the stress and strain dynamics of the host material. The FBG application is not limited to the strain measurement, but also for temperature (Lupi et al., 2019; Wang, Dai, & Wang, 2021), acceleration (Mita & Yokoi, 2000).

The strain data can be directly used for material stress or strain level or indirectly for structural condition assessment. For example, the strain data of a group points along a beam can be employed in vibration-based techniques for structural dynamic identify (natural frequency and shape modes) (Anastasopoulos, De Smedt, Vandewalle, De Roeck, & Reynders, 2018). These data then can use for structural health and damage identification.

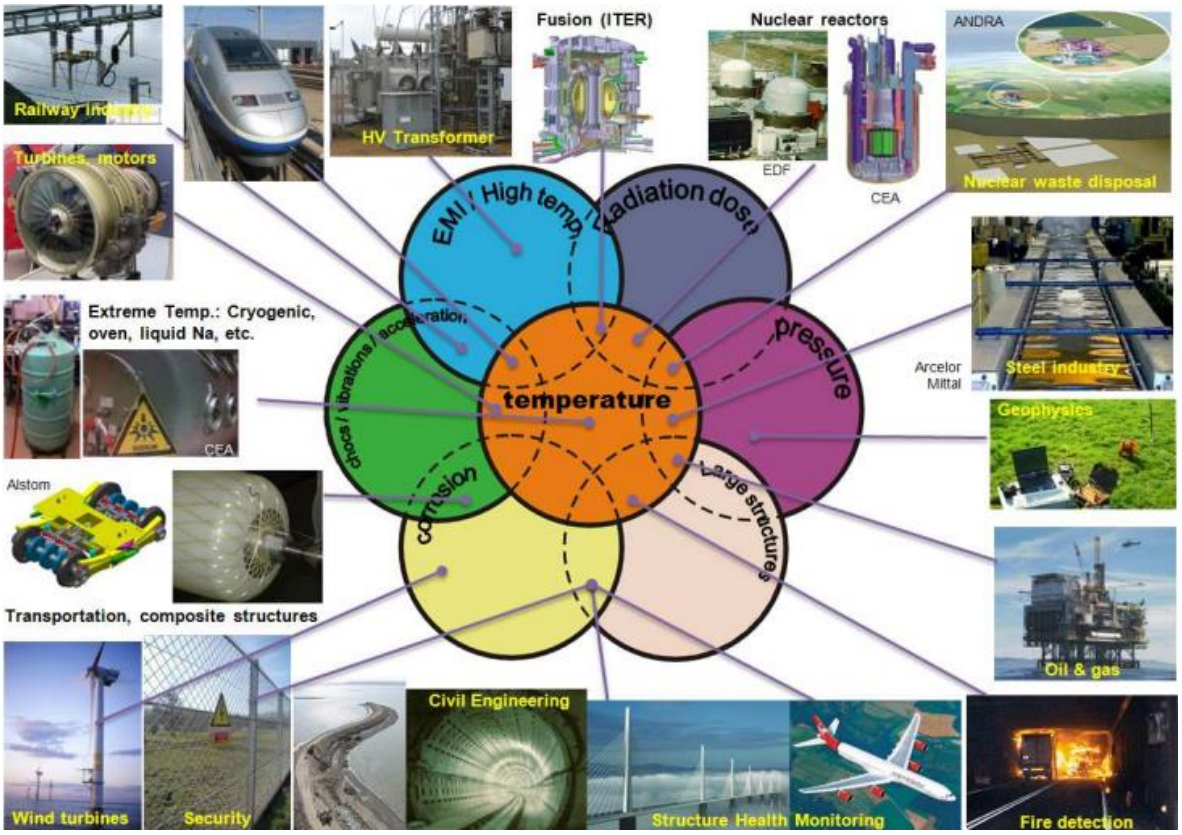

Figure 4. Application of FBG sensors in industry for structural health monitoring (Ferdinand, 2014)

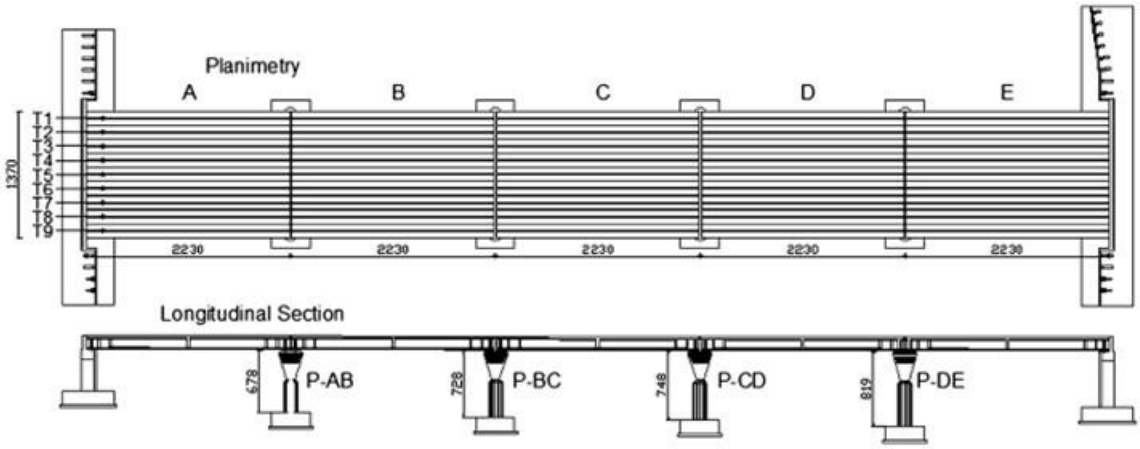

a) Structural health monitoring of concrete bridge using FBG sensors, Italy (Uva et al., 2014)

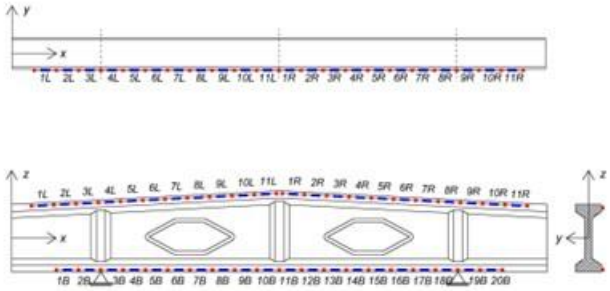

b) Bridge Girder damage assessment using FBG strain data (Anastasopoulos et al., 2018)

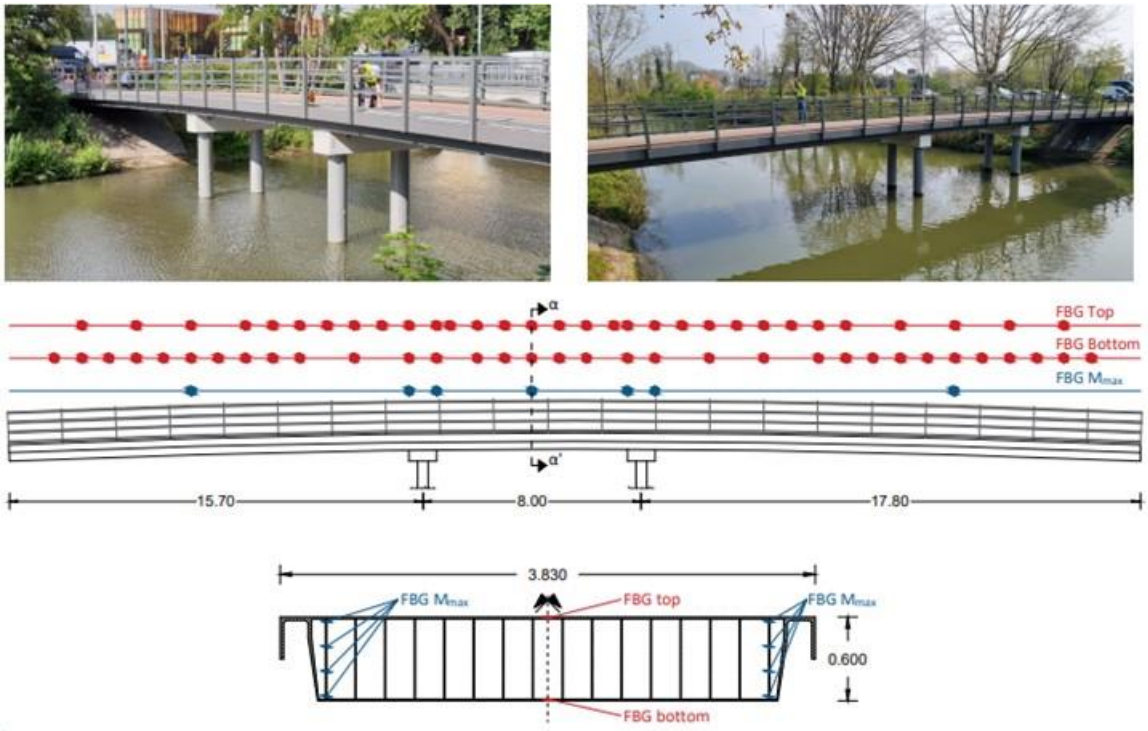

c) Vibration-based monitoring of a footbridge with embedded FBG in Canada

d) Bridge load test and strand internal force monitoring using FBG sensors in Korea (J.-m. Kim, Kim, Choi, & Park, 2016)

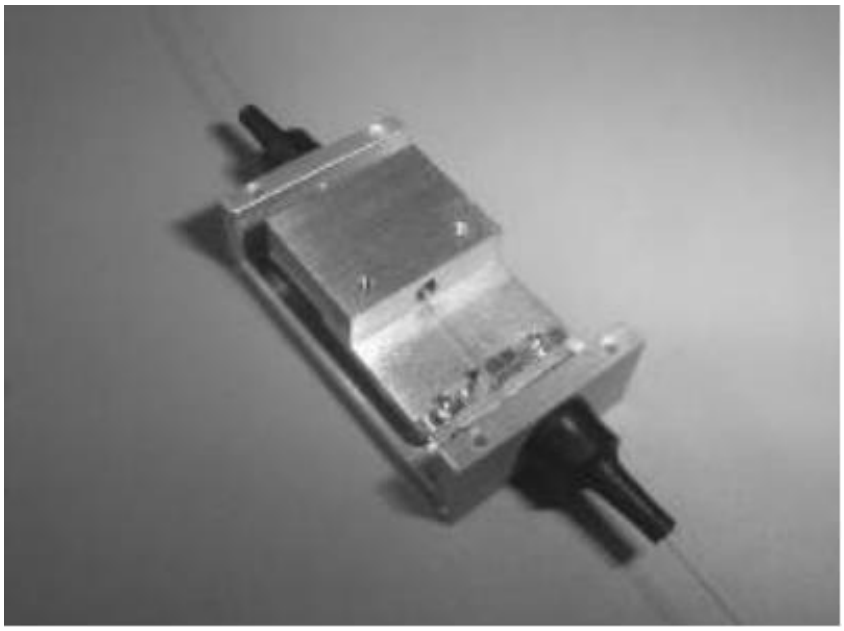

e) A mechanism based on FBG for acceleration measurement (Mita & Yokoi, 2000)

Figure 5. Application of FBG sensors in structural engineering

Besides all inherent advantages of FBG, there are some limitations regarding its application, especially for strain monitoring in steel strands. Some of them are as follows:

1. Bragg Grating portion of the FBGs are short (1-24mm) and cannot attach to ribbed surface especially for steel strand in which the surface is helical shape (Figure 6).
2. For a steel strand, the strain value at a specific point is the average of the strain of all wires at that particular point. However, the Bragg Grating portion of the common FBG sensor is short (1-24), meaning that only 1-2 wires can be sensed at the same time in our case, given that the FBG length is 10 mm.

- Bare fiber must be glued to the element surface. In this situation, FBG might be damaged during the concrete casting process.

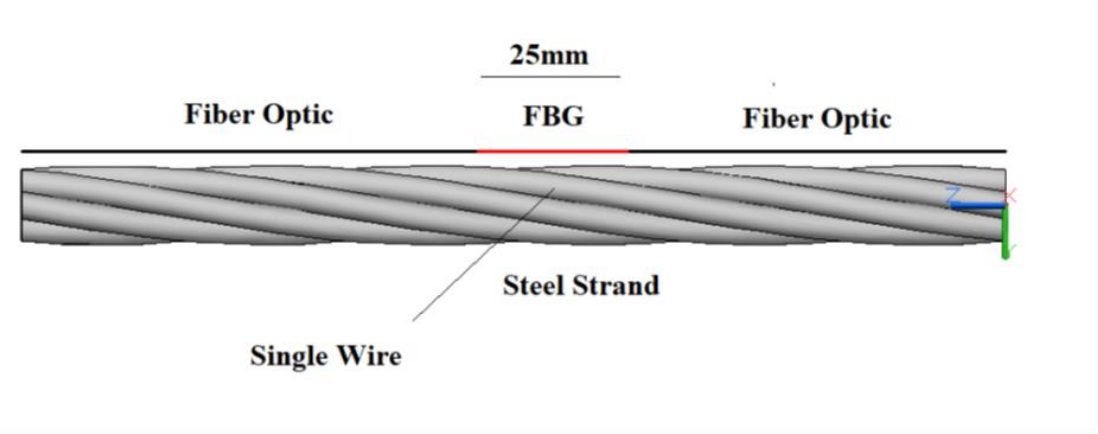

Figure 6. Steel strand and FBG dimension

A possible solution for reinforcing bar is to make the surface plain (Figure 7.b) or make a groove inside it and embed the fiber into the groove by epoxy resin (Figure 7.a). This solution seems well, but this solution is not acceptable for steel strand as its surface consists of a group of wires twisted helically and since the resulting surface is not plain and any grinding might damage wires and affect the strength of strand and the main element (Figure 7). In addition, fiber optics cannot be used without coating or protecting tube as they are brittle. In some cases, fiber is positioned inside the coating tube and then tube is glued or clamped to the steel strand (Berrocal et al., 2021; Uva et al., 2014). The quality and accuracy of the measurement might be affected since the contact between bare fiber and coating tube is not bonded (Deng & Cai, 2007). Therefore, bare fiber must be attached to the surface of the element with glue which increases the risk of breaking during concrete casting.

Based on the above-mentioned explanations, for monitoring strand strain using FBG sensors, a new solution or technology is highly demanded which supported with experimental test reference data.

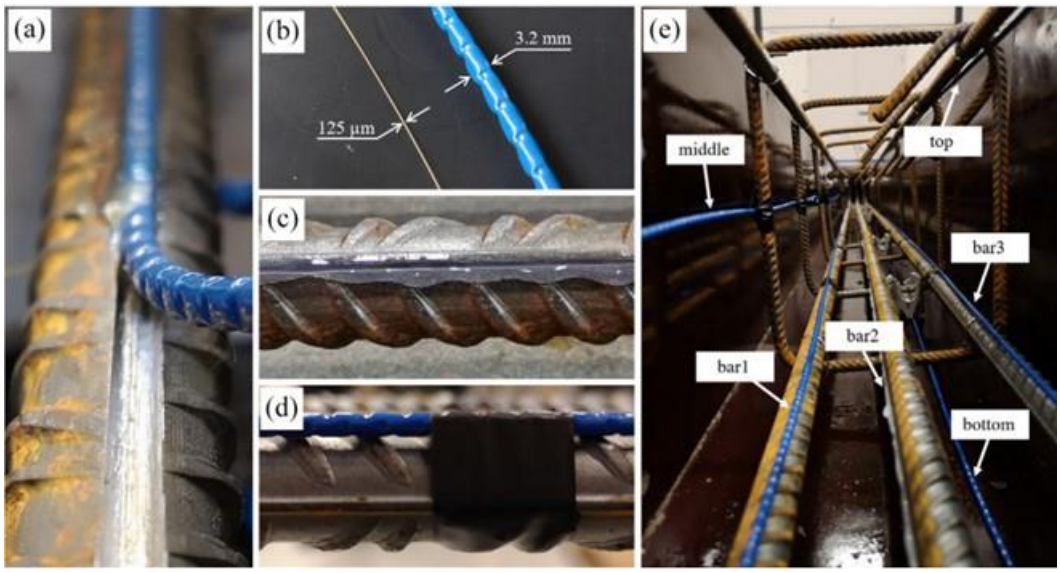

a) Embedding FBG inside a groove in reinforcing bar (Berrocal et al., 2021)

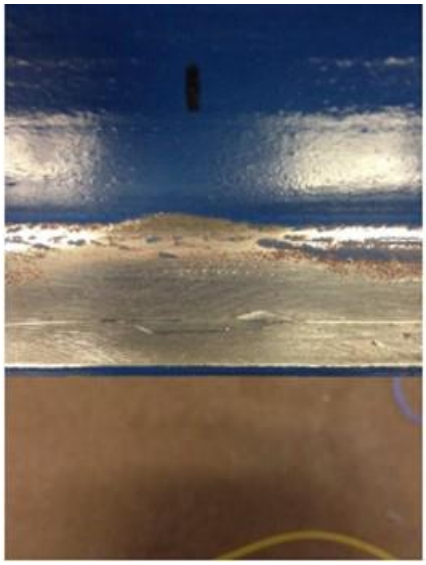

b) Grinding of steel surface for FBG sensor attachment (Anastasopoulos et al., 2017)

Figure 7. Solutions for attaching FBG on ribbed surfaces

In recent years, multiple solutions have been investigated by other researcher's world widely introducing a new smart strand (Figure 10.a). One solution might be to embed the FBG fiber sensor inside a 0.5 mm groove in inner wire and use epoxy resin to glue the fiber to center wire. In this solution, the center wire must be taken out and again the strand must be refabricated. These lead to the reduction of effective area of the strand, which is not favorable (Figure 8).

Kim, et al (J.-M. Kim, Kim, Park, Yang, & Kim, 2012) embedded a FBG sensor inside a steel tube and replaced the inner wire with instrumented steel tube (Figure 9 and Figure 10.b). This makes it possible for effective monitoring of pre-stress forces during both service conditions and the jacking process. Experimental results with prototypes demonstrate the viability of the proposed method as a self-monitoring system for steel strands. In a similar study conducted by same researchers, they embed the FBG inside the carbon core wire of the PC strand (S. T. Kim, Park, Park, Cho, & Cho, 2015) (Figure 11.c). This is a new technology for strand fabrication that produces a smart strand. The carbon core wire was chosen to maintain the performance of the strand equivalent to conventional strands. In another study, a mechanical mechanism was developed for monitoring strain in steel strands utilizing piezoelectric-based sensors (Figure 10.d). This solution underscores the significance of addressing the need for strain monitoring in steel strands.

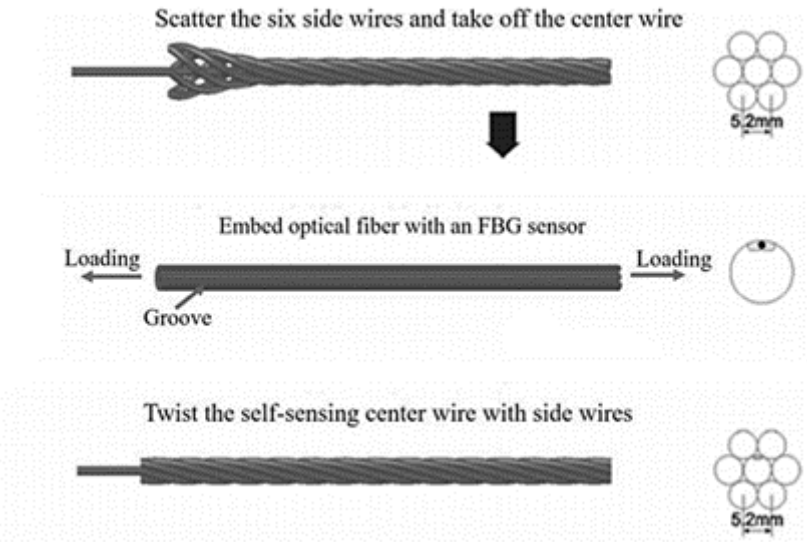

Figure 8. Instrumenting a 7-wire steel strand with optical fiber, milling the central wire (Whanxu et al. 2021).

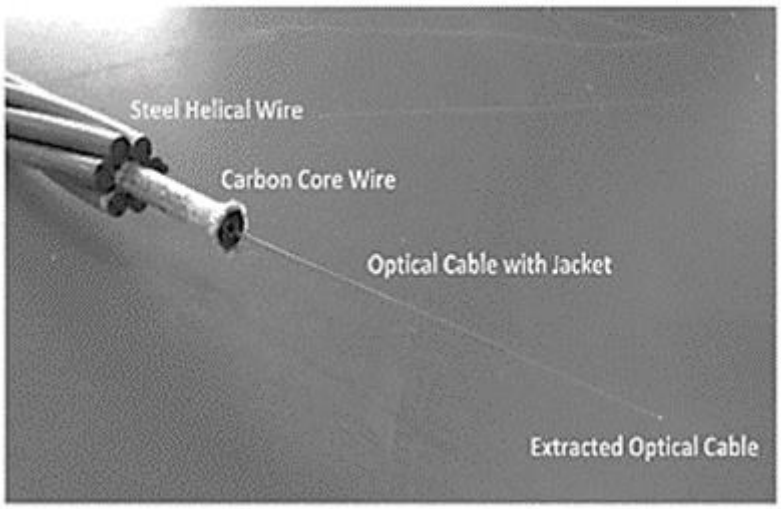

Figure 9. Instrumenting a 7-wire steel strand with optical fibre, by substituting the central steel wire with a carbon wire instrumented with an optical cable (Kim S.T. et al. 2015).

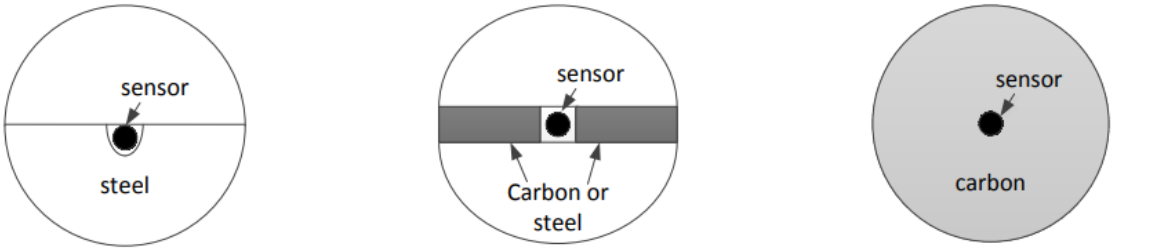

(a) by cutting (b) by reinforcing after cutting (c) by fabrication using carbon

a) Three conceptual solutions for embedding FBG inside inner wire of strand (S. T. Kim, Park, Park, Cho, & Cho, 2014)

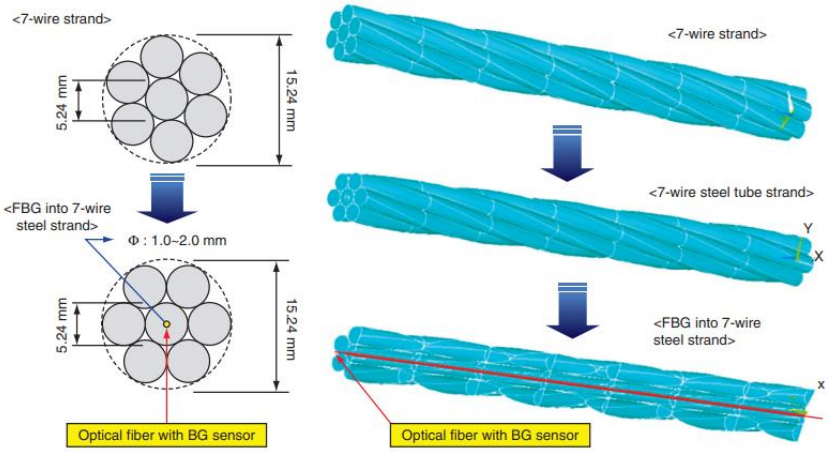

b) steel tube with embedded FBG replaced with inner wire (J.-M. Kim et al., 2012)

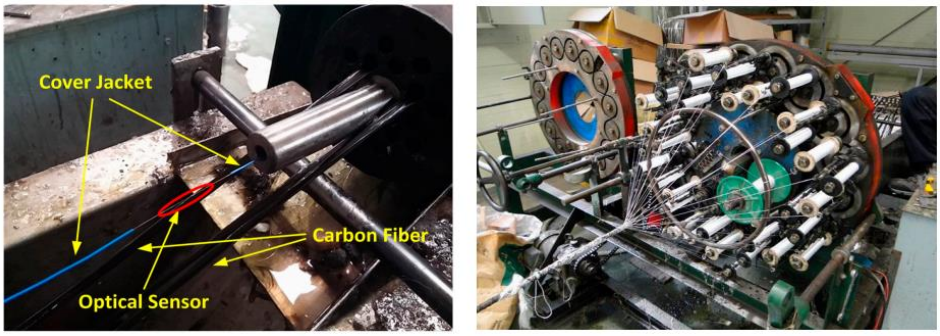

c) Replacing inner steel wire with carbon fiber with embedded FBG (S. T. Kim et al., 2015)

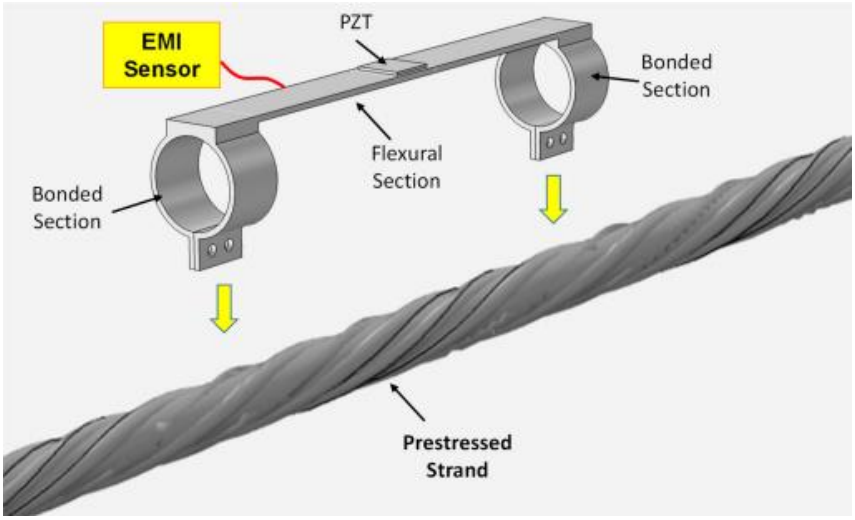

d) pre-stressed monitoring in steel strand using Piezoelectric- based sensors (Le, Phan, Nguyen, Ho, & Huynh, 2021)

Figure 10. Different solutions for strain monitoring in steel strands

Shen, Wang (Shen et al., 2018) used long-gauge fiber Bragg grating for strain monitoring in strands (Figure 11). The length of these gauges is about 30-35cm which covers all the 6 helical wires. The results show this length is equivalent to an average strain of 6 wires and strain can vary up to 40% from wire to wire. In addition, the strain profile can vary considerably along the long gauge while the gauge cannot capture it precisely.

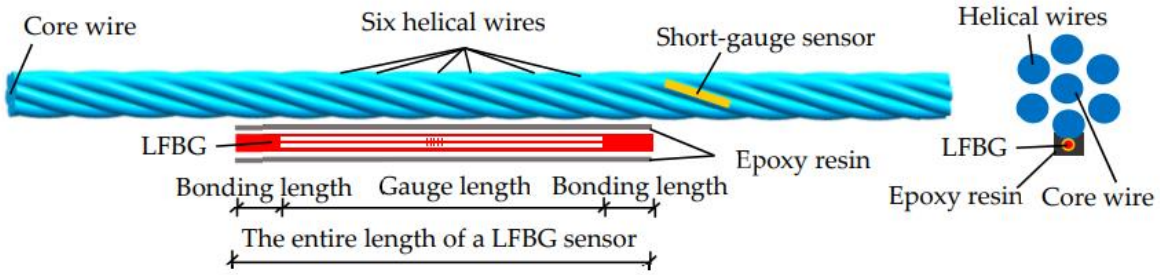

Figure 11. Long-gauge Bragg Grating for strand strain measurement (Shen et al., 2018)

The proposed solutions for strain monitoring of steel strands using FBG sensors either involve modifying the steel strand itself or rely on impractical methods. The necessity for a novel solution to strain monitoring in pre-stressing strands through the utilization of FBG sensors was concluded. For this purpose, it is mandatory that the new solution addresses and removes all the shortcomings and limitations detailed earlier. Consequently, the following specific objectives are clarified here to for employing in the development process towards achieving the ultimate solution:

1. Accurately measure strain of strand (not one wire) with support of experimental tests.
2. Compatible with strands currently available in the market (no need for a new strand type).
- Ensure protection for FBG sensor during construction and concrete casting, preventing possible damage.
3. Designed for easy production for industrial applications.
4. Cost-effective and affordable for structure owners.
5. Simple on-site usage without the need for skilled workers.

The PREFOS project endeavors to suggest and evaluate various approaches for instrumenting a pre-stressed precast reinforced concrete (RC) self-monitoring beam. In its initial phase, the project puts forth a solution for monitoring pre-stressing steel reinforcing bars, specifically 7-wire steel strands. This involves the utilization of a polyester smart saddle, which is instrumented with an FBG sensor, aiding in the precise positioning of the sensor on the surface of the steel strands. This innovative smart saddle can be securely attached to a strand using Sikadur-330 adhesive. The novelty and advantages of this solution lie in its simple to use design, eliminating the necessity to alter strand geometry or fabrication methods. Moreover, its cost-effectiveness makes it favorable for industrialize purposes. Its application is not limited to strands, and it is adaptable for use with reinforcing bars as well. The production process is detailed step by step, and its performance is assessed through thermal and mechanical tests on strands.

Smart saddle basic production procedure with FBG sensors and preliminary test

Smart saddle basic production procedure (Procedure#1)

The smart saddle manufacturing process and performance analysis are explained by four experiments, which have been performed in the laboratory of ENEA research center in FRASCATI.

The smart saddle is composed of the Polyester and the SIKADUR 330 epoxy resin, shown in Figure 12, with the mechanical properties listed in Table 1.

Figure 12. SIKADUR 330 epoxy resin

Compressive Strength		**60 °F (16 °C)**	**73 °F (23 °C)**	**90 °F (32 °C)**	(ASTM D-695) 50 % R.H.
	8 hour	-	-	8,000 psi (55.2 MPa)	
	1 day	8,100 psi (55.8 MPa)	10,700 psi (73.7 MPa)	10,600 psi (73.1 MPa)	
	3 day	11,200 psi (77.2 MPa)	11,100 psi (76.5 MPa)	11,000 psi (75.8 MPa)	
	7 day	11,600 psi (80.0 MPa)	11,200 psi (77.2 MPa)	11,800 psi (81.3 MPa)	
	14 day	12,400 psi (85.5 MPa)	11,800 psi (81.3 MPa)	11,900 psi (82.0 MPa)	
Flexural Strength	8,800 psi (60.6 MPa) (7 days)				(ASTM D-790) 73 °F (23 °C) 50 % R.H.
Modulus of Elasticity in Flexure	5.06 x 105 psi (3,489 MPa) (7 days)				(ASTM D-790) 73 °F (23 °C) 50 % R.H.
Tensile Strength	4,900 psi (33.8 MPa) (7 days)				(ASTM D-638) 73 °F (23 °C) 50 % R.H.
Elongation at Break	1.2 % (7 days)				(ASTM D-638) 73 °F (23 °C) 50 % R.H.
Heat Deflection Temperature	120 °F (50 °C) (7 days)				(ASTM D-648) [fiber stress loading=264 psi (1.8 MPa)]

Table 1. Mechanical information of SIKADUR 330 epoxy resin.

The used Polyester is shown in Figure 13. This type of Polyester is characterized by high wettability with polyester, epoxy and resin. Due to these characteristics, the Polyester is an ideal product for making smart saddles. This Polyester is produced with medium weight fabric 300 gr per square meter, composed of Polyester threads homogeneously arranged but with a random orientation.

Figure 13. The Polyester

The SIKADUR 330 epoxy resin is made by mixing two chemical components with white and light grey colors. In the mixture, the mass proportion between the white and the light grey components is 1 to 4. The procedure is detailed in Table 2 and Figure 14.

Mixing Ratio	Component 'A' : Component 'B' = 4 : 1 by weight
Coverage	First coat: 40-50 ft^2/gal.; Additional coats: 100 ft^2/gal.; Final coat: 160 ft^2/gal.
Pot Life	57 minutes (325 ml)
Cure Time	**Tack Free Time**: 4–5 hours

Table 2. Details for producing the SIKADUR 330 epoxy resin.

Figure 14. Production of the SIKADUR 330 epoxy resin.

The resulting glue is put on both sides of the Polyester as shown in Figure 15.

Figure 15. Putting the mixed epoxy resin on both side of Polyester.

The rest of the production of the smart saddle contains 5 different steps, as explained in the following. In the first step, the strand has been covered by a plastic film to avoid any connection between the strand and the Polyester surfaces, as depicted in Figure 16.

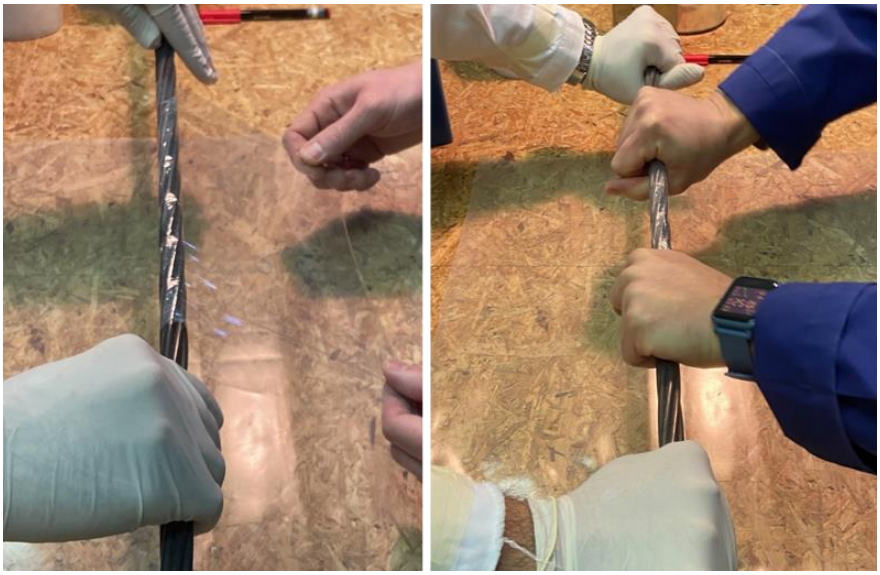

Figure 16. Coating the strand surface with plastic film.

Then, half of the length of the Polyester has been rolled around the strand, as shown in Figure 17.

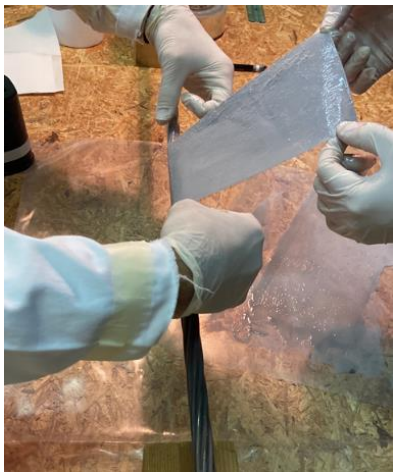

Figure 17. Rolling the half-length of Polyester around the strand.

In the third step, FBG sensor has been put on the Polyester and the remaining part of the Polyester has been rolled around the strand. This step is illustrated in Figure 18.

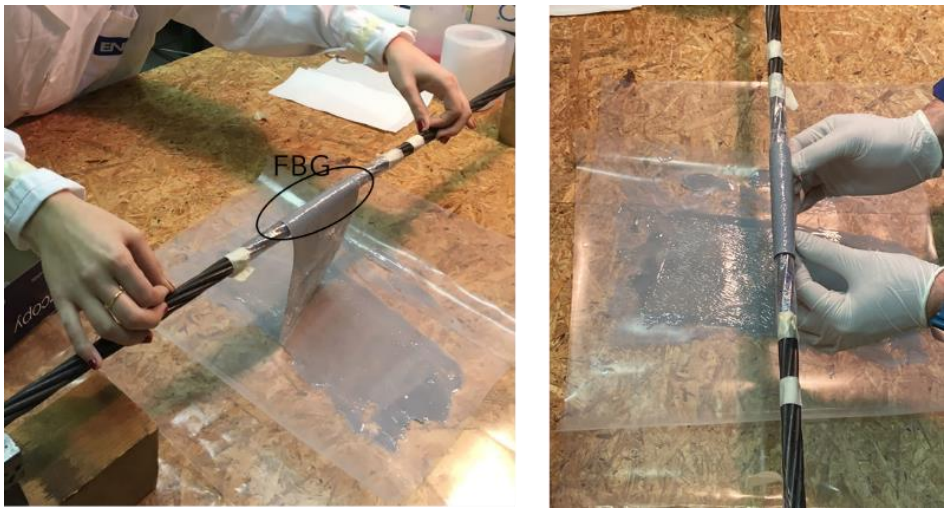

a) b)

Figure 18. a) Putting the FBG sensor on the Polyester, and b) rolling the remaining part of the Polyester around the FBG sensor and strand.

In order to keep epoxy resin homogeneous, a plastic sheet has been used to cover the Polyester during the curing time (see Figure 19).

Figure 19. Covering the smart saddle with plastic sheet until the end of curing.

In the final step, a small part of the smart saddle has been extracted by using an electric cutter as illustrated in Figure 20.

Figure 20. Cutting a small part of smart saddle after curing.

The above-mentioned process has been used to produce smart saddles with two different widths of 30 and 110 mm, and two different diameters of 12.5 and 15.2 mm (see Figure 21). The length of Polyester for producing smart saddles with 110mm width was 240mm and also for smart saddles with 30mm width was 200mm. The Table 3 reports characteristics of all the FBG.

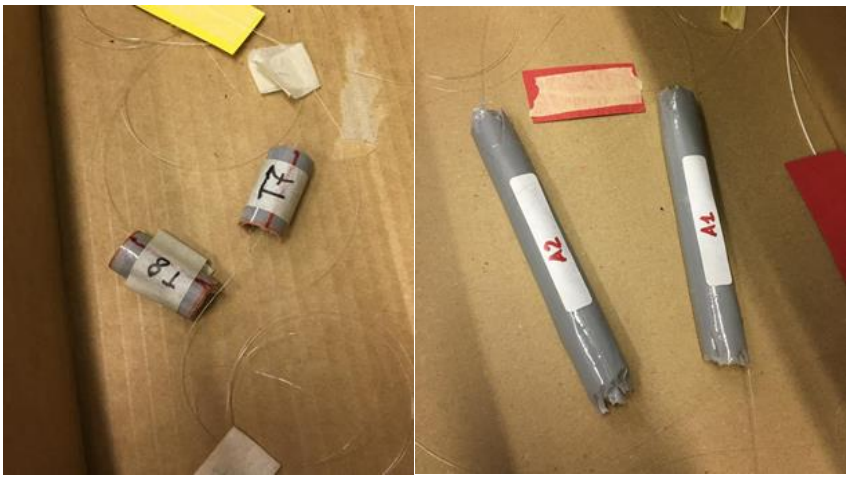

a) b)

Figure 21. a) 30mm, and b) 110 mm smart saddle.

SENSORI FBG											
N	Lungh.onda (lambda_B) [nm]	L FBG [mm]	Diametro sella [m]	Produttore	Trefolo	Sella	Test Funzionamento	L sella [mm]	Ltrefolo [m]	Prova prevista	Posizione [cm]
B1		15	15.2	Broptics	1	sì	non ancora	110	1,30 ca	--	
B2		15		Broptics	2	sì	sì	110	0,50	1)Termica ciclica 2)Bending test	
B3		15		Broptics	3	sì	sì	110	0,50	1)Termica ciclica 2)Bending test	
A1	1539	15	15.2	AOS	--	sì	sì	110	--	1)Termica ciclica	
A2	1558	15	12.5	AOS	--	sì	sì	110	--	1)Termica ciclica	
A3	1532	15	12.5	AOS	--	sì	NON FUNGE	110	--	1)Termica ciclica	
A4	1550	15	--	AOS	--	sì	NON FUNGE	110	--	ROTTO DURANTE PRODUZIONE SELLA	
T1	1557 (+/- 0,25)	10	15.2	Technica SA		sì	sì	30		1)prova carico campione lungo 376,5 cm	Mezzeria = 188,25 cm
T2	1565 (+/- 0,25)	10	15.2	Technica SA		sì	sì	30		1)Trazione ciclica	
T3	1537 (+/- 0,25)	10	12.5	Technica SA		sì	sì	30		1)Trazione ciclica	
T4	1561 (+/- 0,25)	10	12.5	Technica SA		sì	sì	30		1)Trazione ciclica	
T5	1549 (+/- 0,25)	10	15.2	Technica SA		sì	sì	30		1)prova carico campione lungo 376,5 cm	1/4 Lcavo= 94 cm (up)
T6	1545 (+/- 0,25)	10	15.2	Technica SA		sì	sì	30		1)prova carico campione lungo 376,5 cm	1/4 Lcavo= 94 cm (down)
T7	1541 (+/- 0,25)	10	12.5	Technica SA		sì	sì	30		1)Trazione ciclica	
T8	1557 (+/- 0,25)	10	12.5	Technica SA		sì	sì	30		1)Trazione ciclica	
T9	1533 (+/- 0,25)	10	12.5	Technica SA		sì	sì	30		1)Trazione ciclica	
T10	1545 (+/- 0,25)	10	12.5	Technica SA		sì	sì	30		1)Trazione ciclica	
T11	1553 (+/- 0,25)	10	12.5	Technica SA		sì	sì	30		1)Trazione ciclica	
T12	1517 (+/- 0,25)	10	15.2	Technica SA		sì	sì	30		1)Trazione ciclica	
T13	1533 (+/- 0,25)	10	15.2	Technica SA		sì	sì	30		1)Trazione ciclica	
T14	1541 (+/- 0,25)	10	15.2	Technica SA		sì	sì	30		1)Trazione ciclica	

Table 3. The properties of all FBG.

Smart saddle performance analysis

In this section, the results of the tests conducted on the manufactured smart saddles are presented.

Thermal Tests

Cyclic thermal test on strand

In order to perform this test, according to diameter of the strands, two smart saddles with 15.2mm and 12.5mm diameter consist of FBG have been bonded to the strand by means of the epoxy resin (Araldite 2011) as shown in Figure 22a. The epoxy resin has been put in three line inside of the smart saddle (see Figure 22a). Before bonding, any impurities on the strand surface is removed by using an abrasive brush as shown in Fig. 22b. Finally, the smart saddle is placed on the strand surface (see Figure 23). The curing process of the glue requires about 24 hours.

a) b)

Figure 22.a) Putting the epoxy resin inside of the smart saddle, and b) brushing the strand surface.

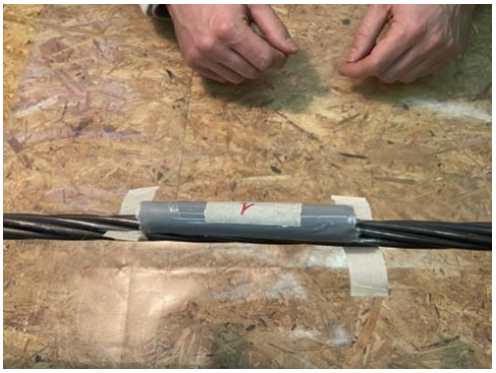

Figure 23.Placing the smart saddle on the strand surface.

After curing time, the strands have been inserted in the oven as illustrated in Figure 24. In this test the FBG sensor number 2 and 3 are bonded on the strands with diameters of, respectively, 12.5 and 15.2 mm as illustrated in Figure 24.

Figure 24.The bonded smart saddles on the strands in the oven.

For recording the variation of temperature during the test, a temperature sensor has been used (Figure 25).

Figure 25.Temperature sensor.

The wavelength shift of FBG sensors has been recorded by means of the data acquisition system during the test, as depicted in Figure 26. The test started on 15/02/2022 at 11:08:00 and stopped on 22/02/2022 at 03:09:00.

Figure 26.The data acquisition.

In the test, the temperature fluctuates for several cycles, as shown in Figure 27, between the minimum and maximum temperature of 20 °C to 70 °C.

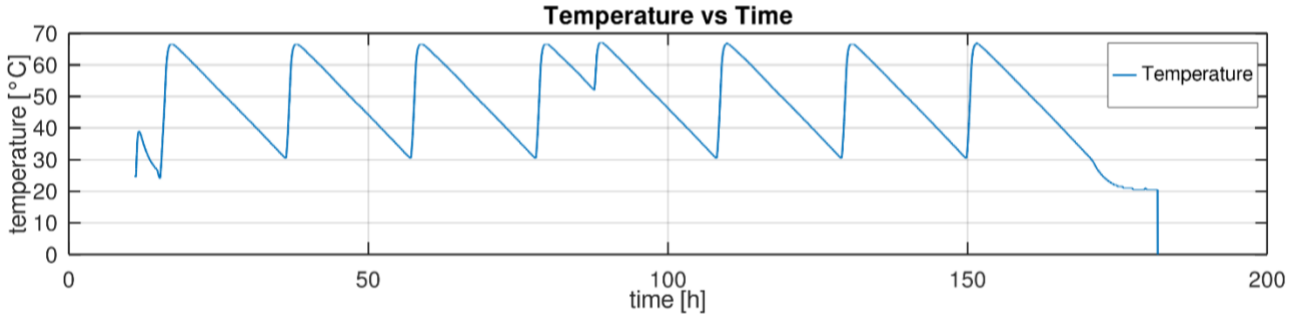

Figure 27.Variation of temperature during time.

According to the data that is read by FBG sensors, the wavelength increased and decreased as a consequence of the temperature variation during the test. Moreover, the wavelength shifts that are read by the two FBG sensors are in good agreement, as reported in Figure 28.

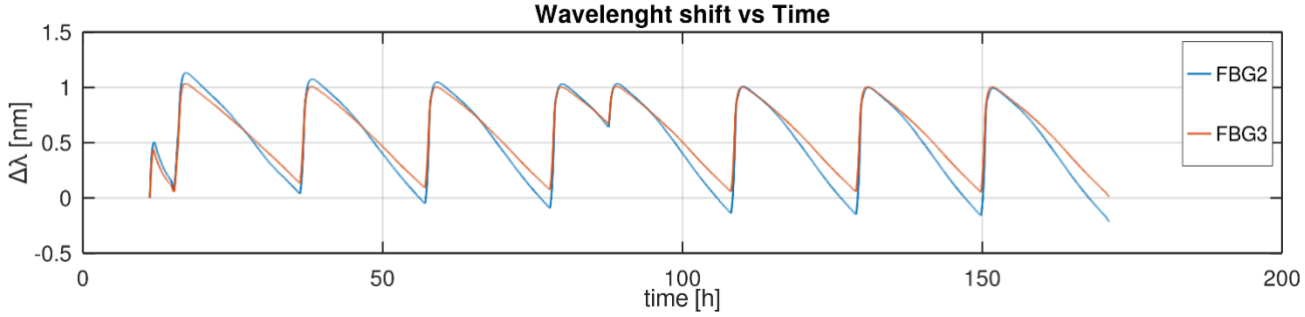

Figure 28.The wavelength during the test.

The µstrains, which is read by FBG sensors during the test, are shown in Figure 29.

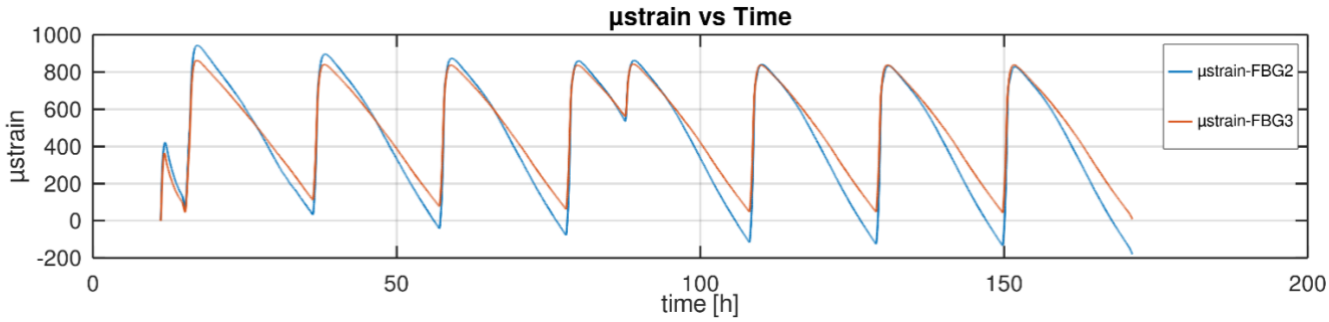

Figure 29.The µstrain has been read by FBG.

For better understanding the relation between the µstrain and the temperature variation, the wavelength shift, and the temperature are plotted against the time in Figure 30. The µstrain has been increased as a consequence of temperature increase. The two FBG sensors recorded the same µstrain during the heating phase. In particular, the difference between the maximum recorded µstrain by the two FBG sensors reduce as the time goes by so that for the time higher than 100 hours, the two sensors recorded the same maximum µstrain.

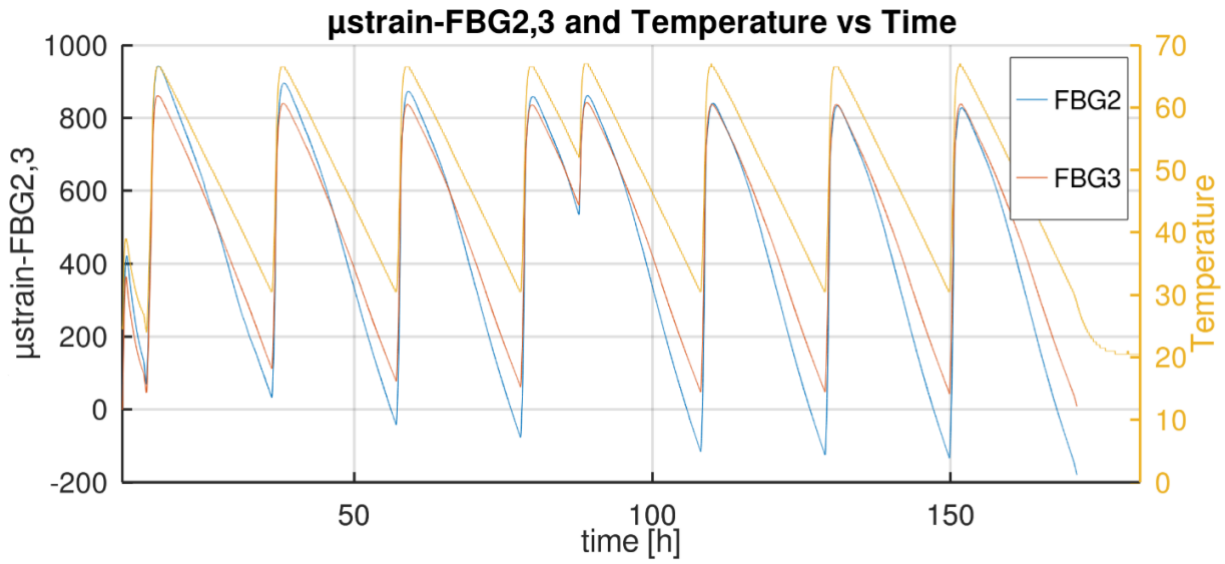

Figure 30. Variation of strain and temperature during the test.

The Figure 31 a, and b show that there is a linear relationship between the temperature and the µstrain during heating phase. But this relationship for the cooling phase is nonlinear. In addition, the cooling phase takes more time than the heating phase, since there was not any cooling system for reaching to the minimum temperature.

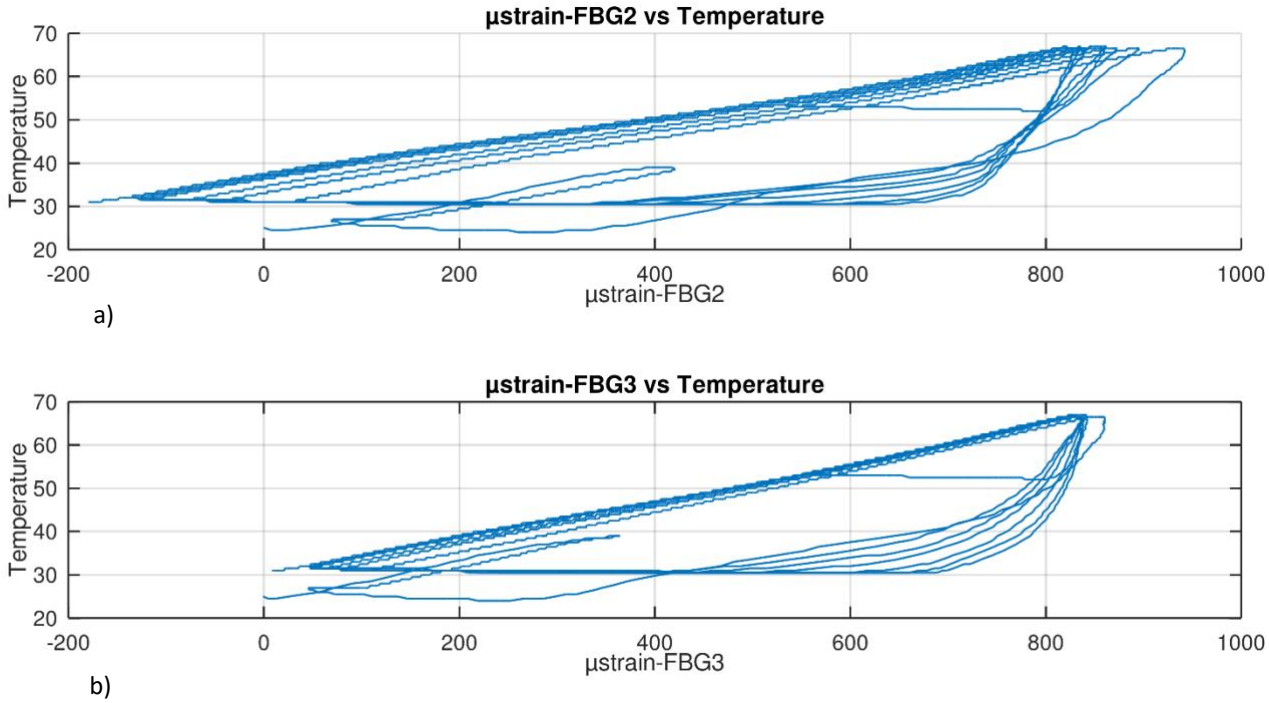

Figure 31.The µstrain read by a) FBG2 and b) FBG3 with various temperature.

Cyclic thermal test on smart saddles

In order to better understand the behavior of FBG sensors due to the temperature variation, several cyclic thermal tests have been performed on the FBG sensors as chains. The first thermal test has been performed on two smart saddles with 110mm width that are named A1 and A2 (see Table 3).

To make a chain between FBG sensors (Figure 32a), a fusion machine has been used (see this machine in Figure 32b).

a) b)

Figure 32.a) Making the chain between FBG sensors by b) fusion machine.

Then the FBG sensors has been put in the oven and the test started on 16/03/2022 at 14:04:58 and finished on 21/03/2022 at 13:00:54. The variation of temperature inside of the oven was similar to the first thermal test on the strands with smart saddles (20 °C < temperature < 70 °C), as shown in Figure 33.

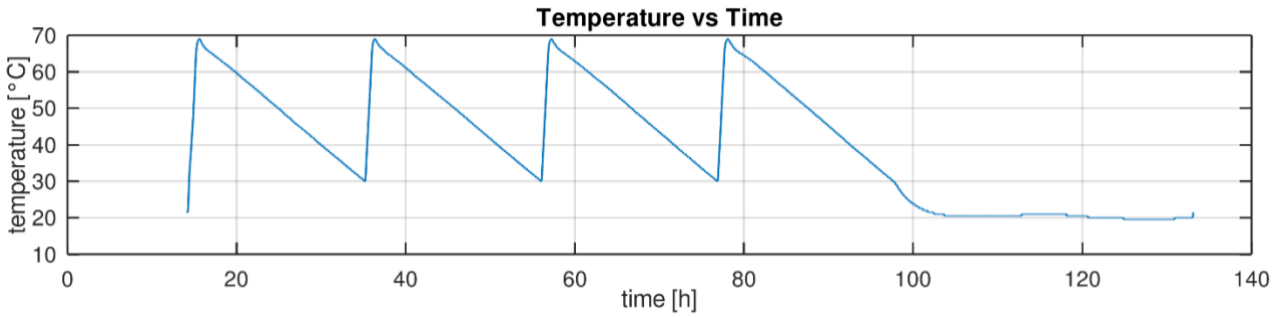

Figure 33.The variation of temperature during the test.

The Figure 34 shows the wavelength shift that is read by FBG A1 & A2 in this experiment. The wavelength shift increased and decreased as a consequence of the temperature variation. As it can be seen in the figure, the results read by both sensors are in good agreement.

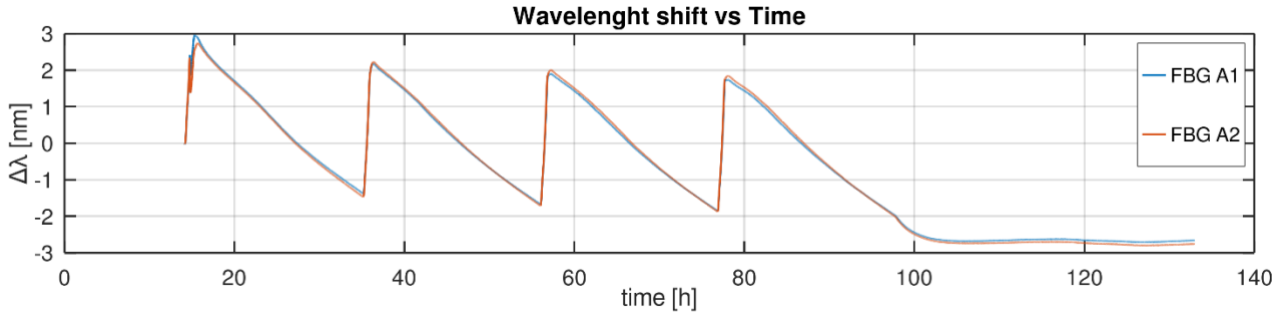

Figure 34. Wavelength shift read by FBG sensors during the time.

The results in Figure 35 indicate that the µstrain was changing according to the temperature variation. The FBG sensors as a chain read almost the same µstrain.

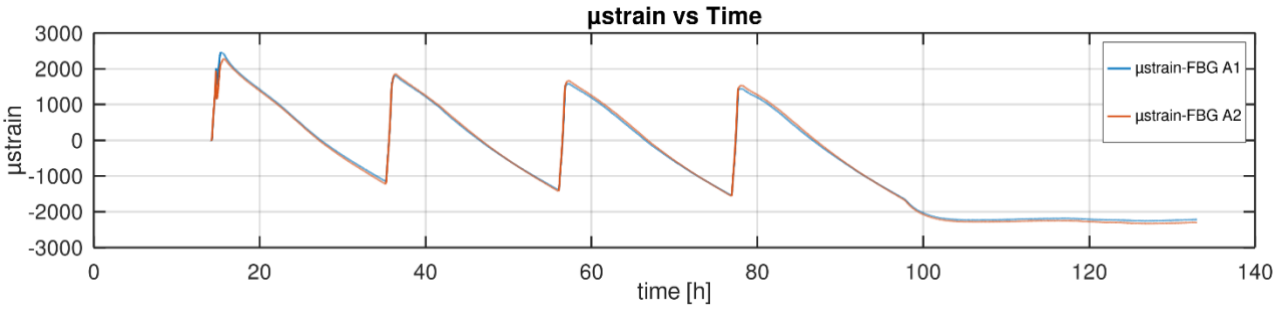

Figure 35. The FBG sensors A1 & A2 read the same µstrain during the test.

The variation of temperature and µstrain are plotted in Figure 36 against the time. It can be understood from the results that the FBG sensors function appropriately together in the chain.

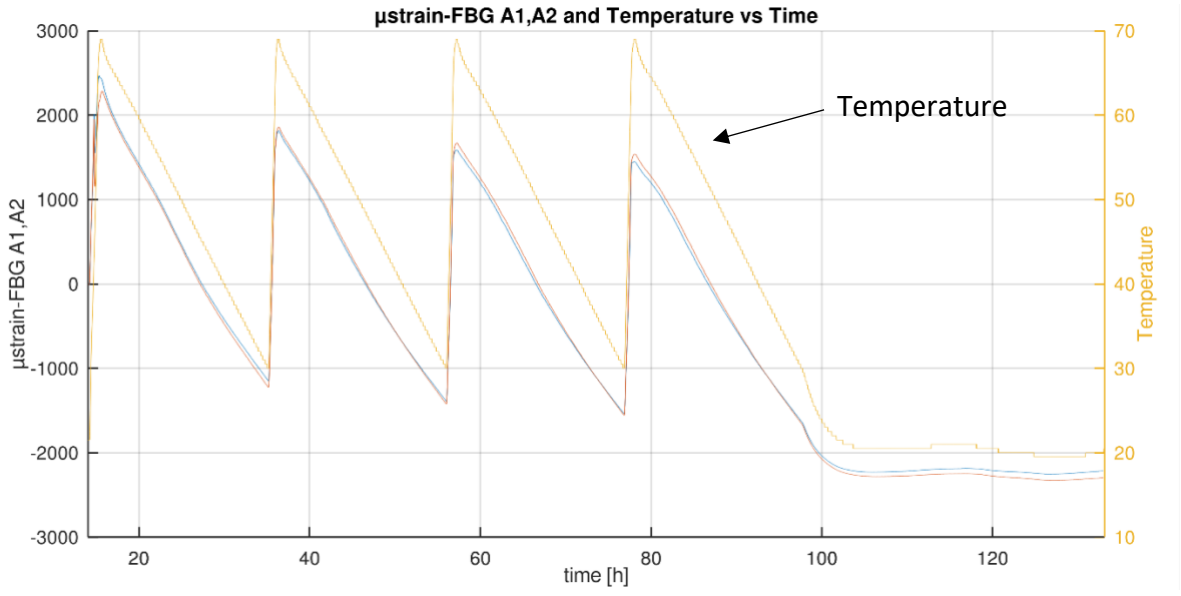

Figure 36.The various temperature ang wavelength shift in the same plot.

Finally, the variations of the temperature versus the µstrain are shown in Figure 37 for both sensors.

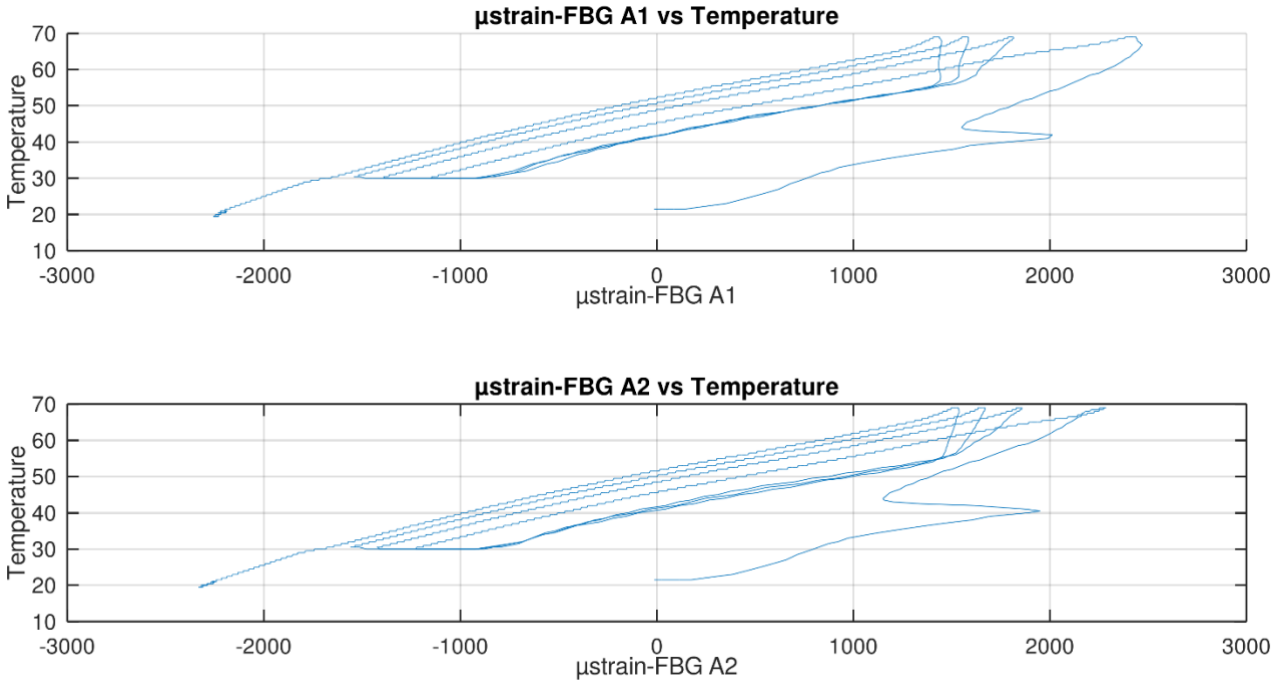

Figure 37.The strain and Temperature variation during test.

In order to study all of the smart saddles which have been manufactured in laboratory of ENEA, four chains have been prepared separately for another cyclic thermal test. The FBG sensors have been selected in each chain according to their spectrum. The chains are shown in Figure 38. The chains number 1, 2 and 4 have been made by FBG sensors with 30mm length whereas, the chain number 3 has been made by FBG sensors with 110mm length. Moreover, the chains number 1 and 2 consist of three FBG sensors while, the rest consist of two FBG sensors.

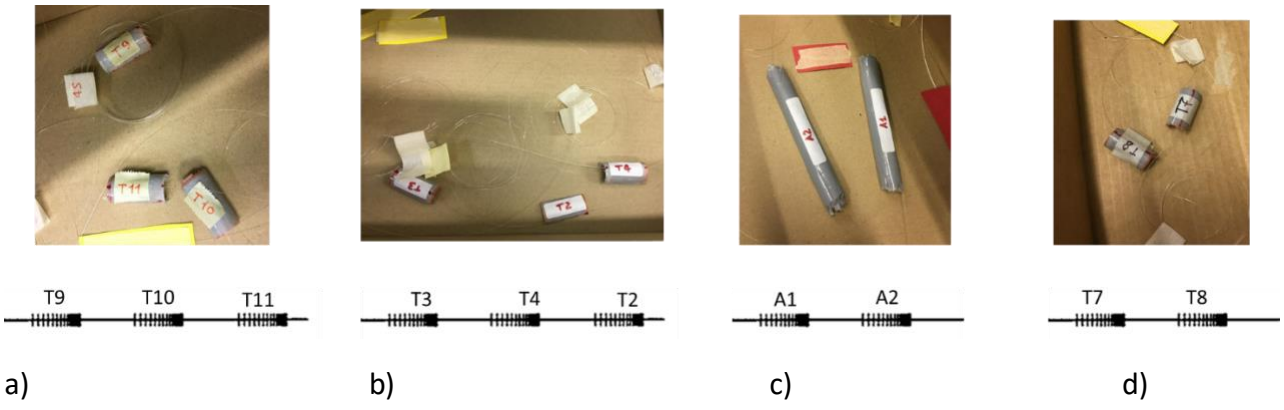

a) b) c) d)

Figure 38. The photo and sketch of a) Chain number 1, b) Chain number 2, c) Chain number 3, d) Chain number 4.

Each chain has been put inside the oven separately in a paper box and connected to one channel of data acquisition. The chain number 1, 2, 3 and 4 have been connected to channel 0, 1, 2, and 3, respectively (Figure 39 and 40).

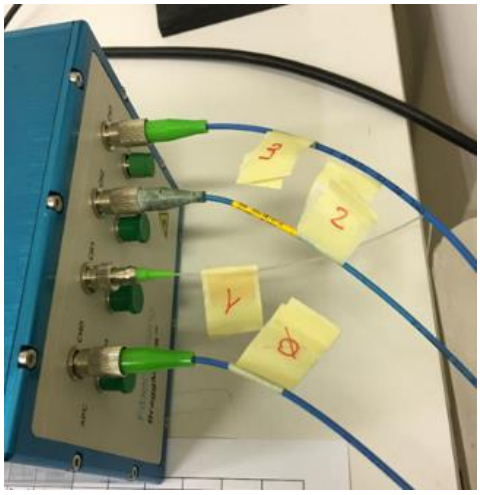

Figure 39. Each chain is connected to one channel.

Figure 40.The chains inside of the oven.

The temperature variation for this test was the same as those of the other thermal tests. The experiment started on 25/05/2022 at 13:00:02 and stopped on 30/05/2022 at 10:07:37. The variation of temperature, which has been recorded by means of the temperature sensor, is reported in Figure 41. In this experiment the temperature reached a maximum degree in 4 cycles.

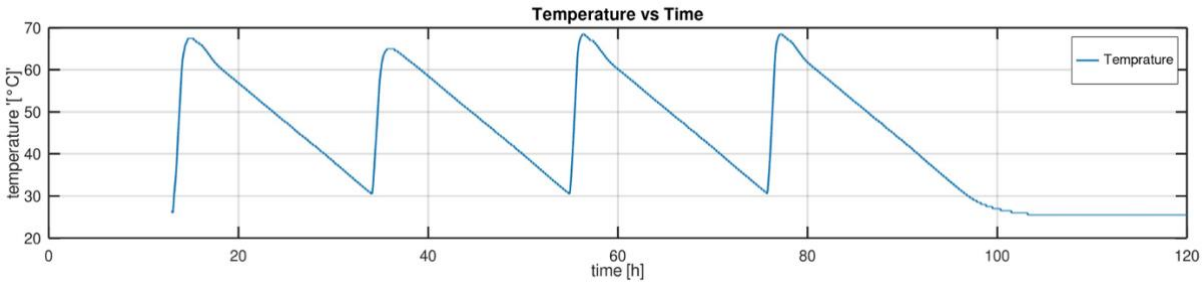

Figure 41. The various temperatures during the test.

The wavelength shift has been read by chains in this test is reported in Figure 42. Note that the wavelength shift has been read by chain number 3 (Figure 42c) is higher than the other chains. This might be due to the higher length of this chain as well as the higher length of the Polyester (40mm longer) used to manufacture the chain number 3.

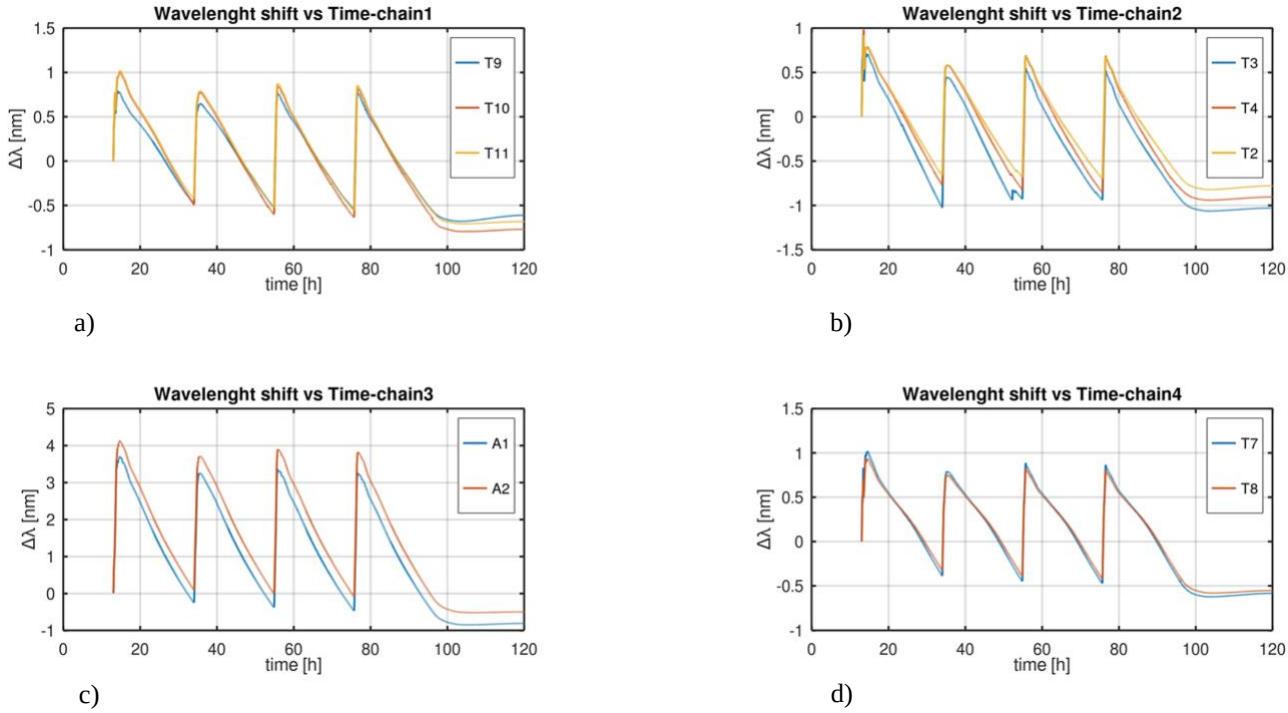

Figure 42.The wavelength shift read by a) Chain number 1 b) Chain number 2 c) Chain number 3 d) Chain number 4.

The variations of the wavelength shift, and the temperature are shown in Figure 43 for all the four different chains.

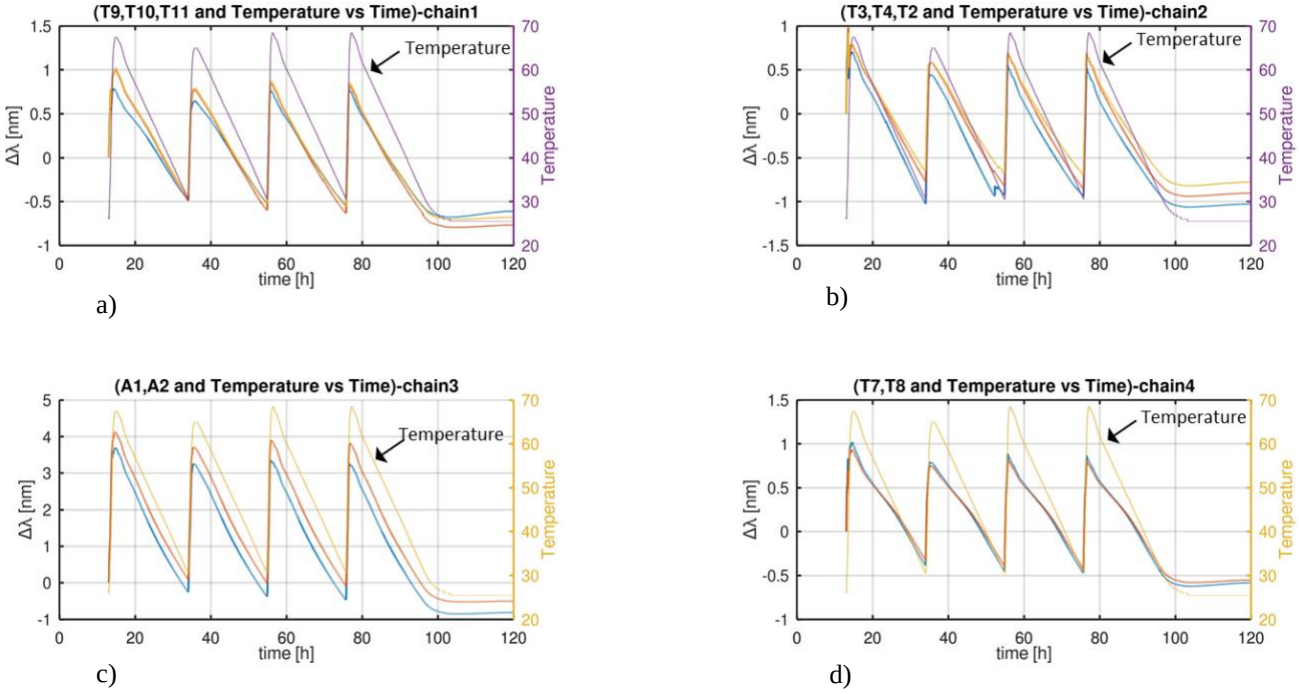

Figure 43. Wavelength shift and temperature against time for a) Chain number 1 b) Chain number 2 c) Chain number 3 d) Chain number 4.

The results in Figure 44 indicate that the µstrain was changing according to the temperature variation in each chain.

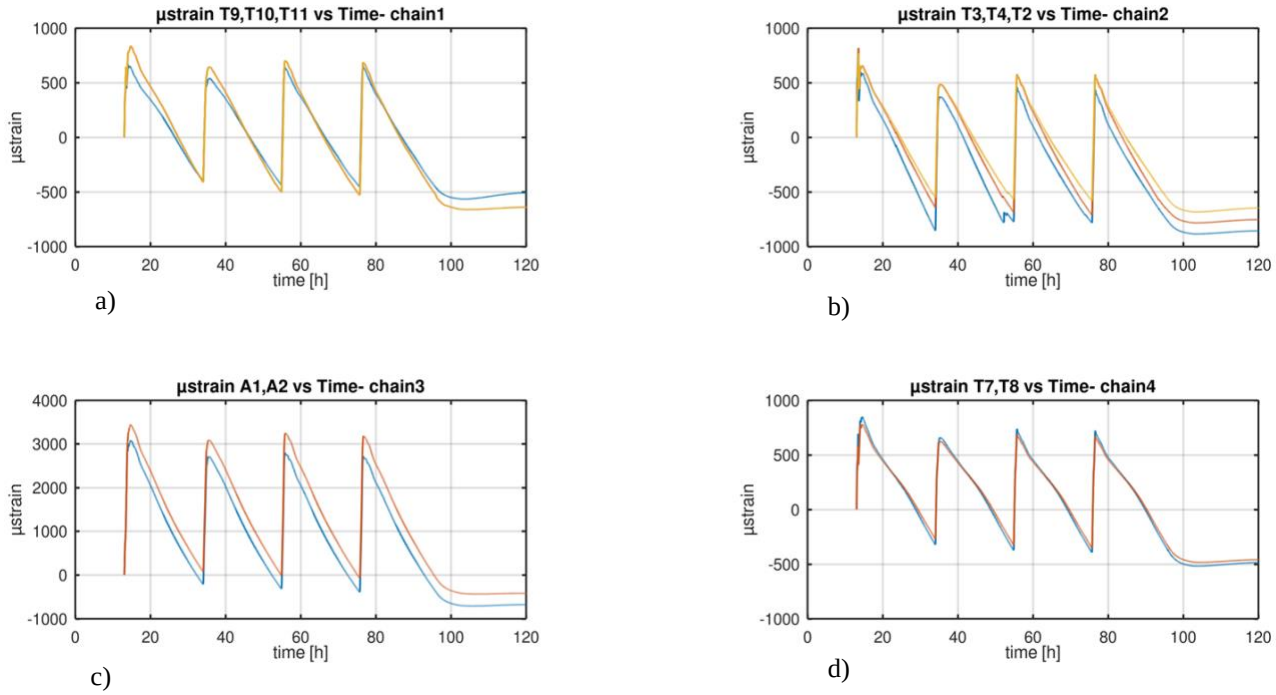

Figure 44.The strain against time for a) chains 1, b) chains 2, c) chains 3 and d) chains 4.

In this test, similar to the result of previews thermal tests, during the heating phase there is a linear relationship between increasing the temperature and wavelength shift: Figure 45 and Figure 46.

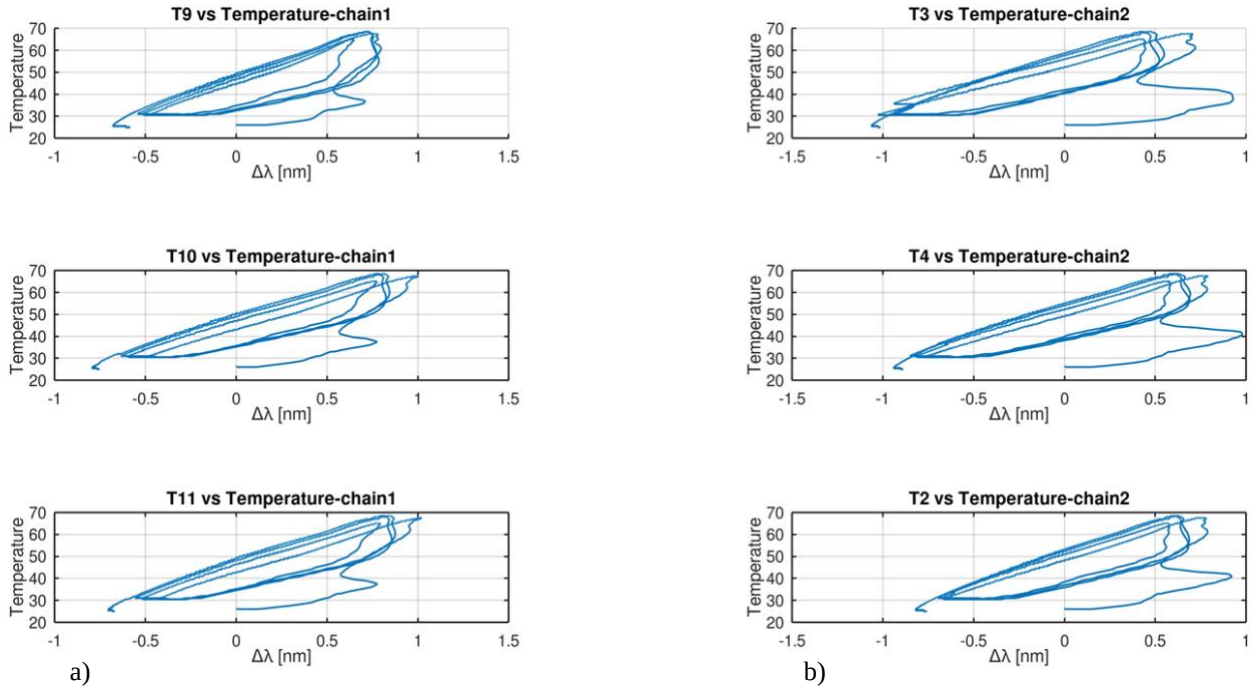

Figure 45. The strain and Temperature variation during test for a) chain 1 and b) chain 2.

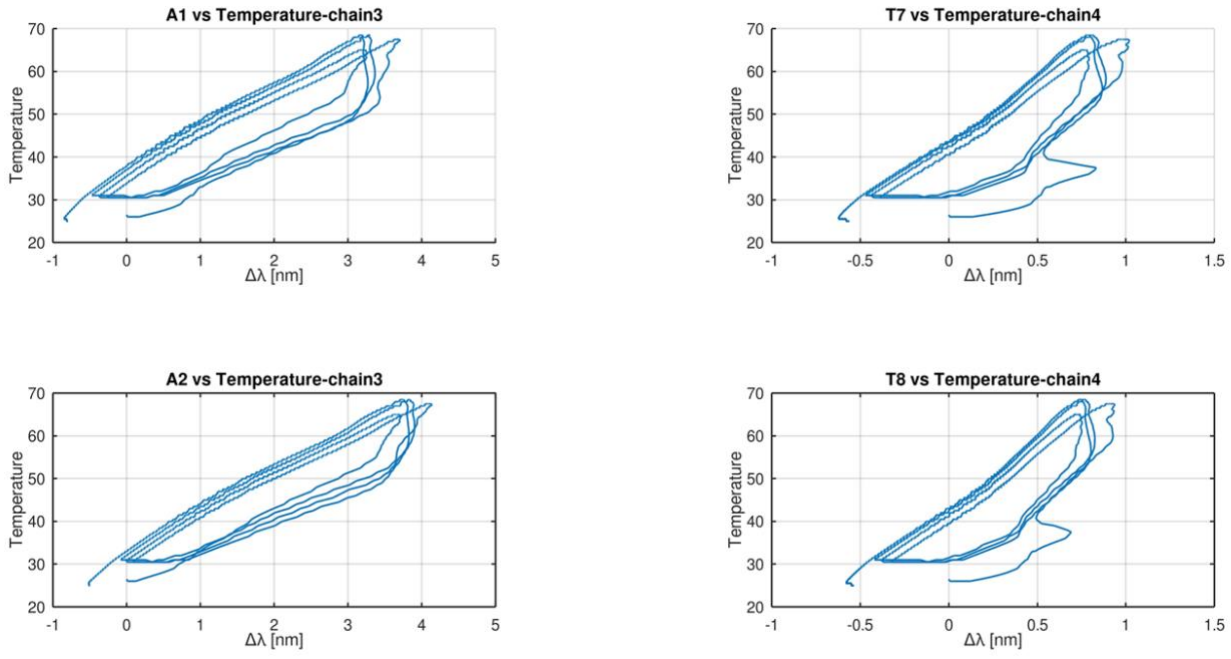

Figure 46. The strain and Temperature variation during test for a) chain 3 and b) chain 4.

Mechanical Tests

Tensile Test at ENEA Research Center in FRASCATI

To characterize the sensors housed within, a testing structure was constructed to tension the steel strand and assess their performance. The strand was equipped with three smart saddles, each outfitted with an FBG and custom-fitted to secure onto the strand like a clip, capitalizing on their elasticity. The smart saddles were crafted using epoxy resin, with a thickness of 1.5 cm, ensuring proper embedding of the optical fiber, and a length of 3 cm to minimize the space occupied on the strand.

Initially, structural glue was applied to the concave surface of the smart saddles, after which they were positioned on the strand, allowing the glue to cure. It's noteworthy that the FBGs applied to the smart saddles were connected in series to enhance the manageability of the steel strand. For this purpose, the following reference wavelengths were utilized: $\lambda_{ref,FBG1} = 1545\ nm$, $\lambda_{ref,FBG2} = 1549\ nm$ and $\lambda_{ref,FBG3} = 1557\ nm$.

In the testing structure, one end of the strand is secured, while at the opposite end, a mechanical system comprising a nut and a screw facilitates the tensioning of the strand. Specifically, a step-by-step tensioning approach is employed, with each step corresponding to a full turn of the screw. Figure 47(a) illustrates the schematic of the metallic structure housing the strand, and in Figure 47(b), a magnified image of the smart saddle applied to the steel strand (upper figure) and a photograph of the structure used for static tests are presented (lower figure).

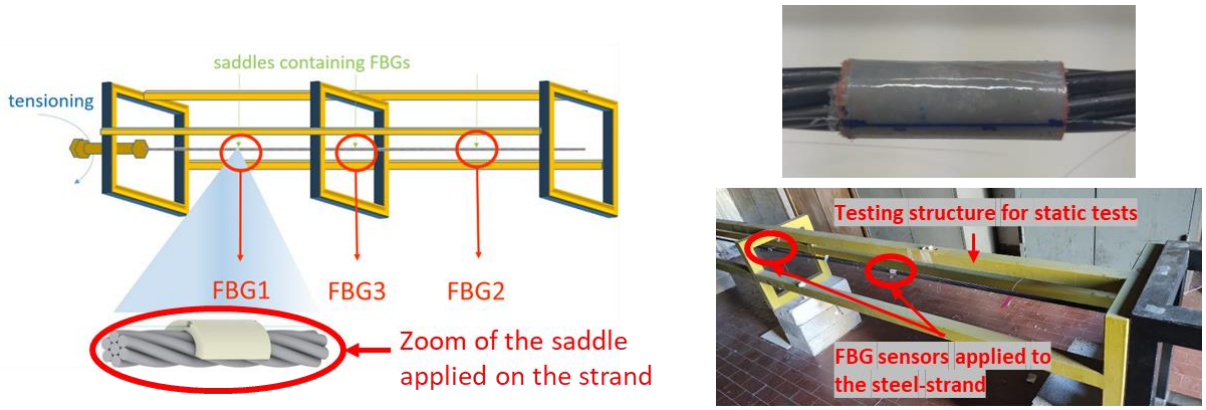

a) b)

Figure 47. The drift of wavelength shift in each cycle, a) smart saddle at the top, b) smart saddle at the bottom of strand.

The execution of tests is crucial to characterize the performance of sensors equipped with FBGs and housed in smart saddle-like structures. These tests are expected to align experimentally with the well-established mechanical behavior of the simple system under examination. Our focus lies in characterizing FBGs for civil applications, particularly their capability to measure micro-strains on strands. When we refer to "static tests," we are alluding to the analysis of the wavelength parameter as a consequence of the strand stress. Tension scales are created by applying different levels of screwing through a mechanical structure (Figure 47 (a)). In this setup, the cable has a fixed terminal, and on the other end, a system allows for the extension of the strand by turning a screw.

On the other hand, by "dynamic tests," we mean the examination of frequency peak variations under different tensioning levels. In Section 2.1, the static analysis will be presented, and the results obtained in terms of wavelength variations will be evaluated. In Section 2.2, two types of dynamic tests (hammer impact and hanging weight) will be showcased, and the frequency behavior will be scrutinized through spectral analysis using FFT: Fast Fourier Transform.

Static tests were conducted by applying varying levels of tension to the steel strand. This was achieved by simply screwing and unscrewing the nut at one of the ends of the strand. Figure 2 illustrates the wavelength variation of FBG1 under different tensioning levels. (Since the behaviors of FBG2 and FBG3 are similar, only FBG1 is presented.) It's worth noting that a "+1 screwing" denotes a complete turn of the nut, resulting in an increased tension on the strand, and this pattern continues for the other labels.

The results depicted in Figure 48 indicate that an increase in tensioning on the cable corresponds to a rise in wavelength. Conversely, a decrease in stress on the strand leads to a decreasing trend in wavelength.

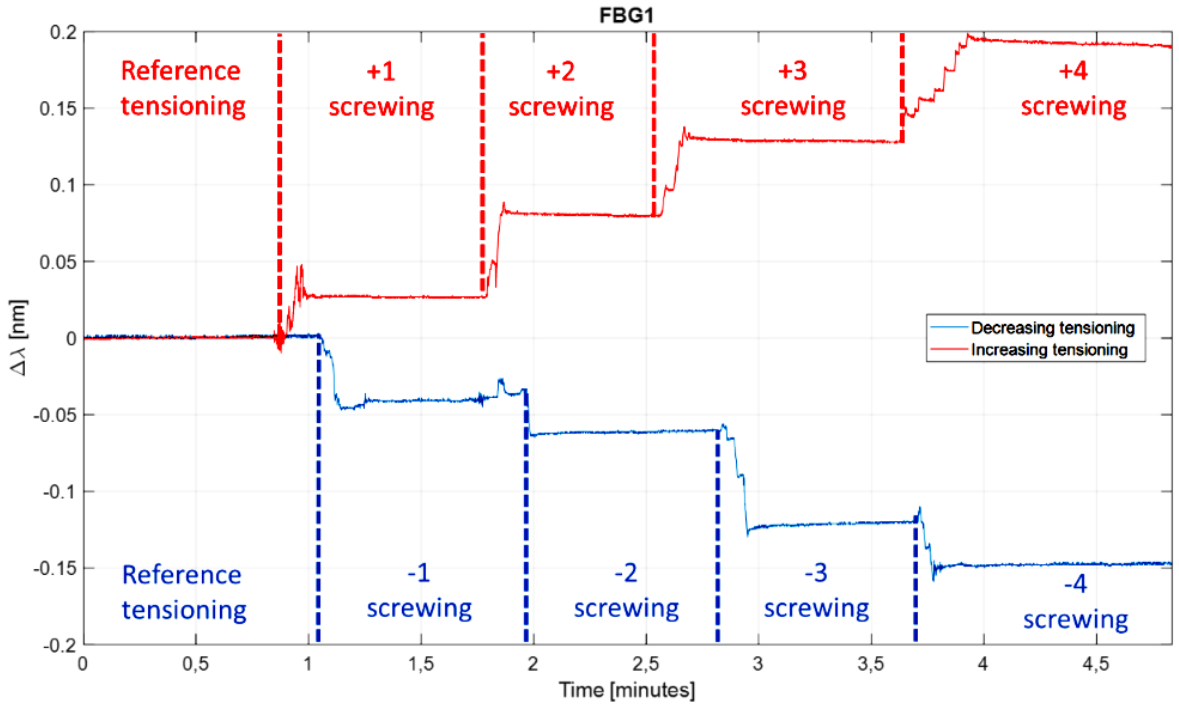

Figure 48. Wavelength variations on FBG1. The rad trace indicates an increase of the tensioning on the steel strand while the blue trace refers to a decrease on the stress level of the cable.

The objective of dynamic tests is to demonstrate the effective capability of the smart saddle prepared sensors to monitor the operational frequencies of the strand. This assessment is crucial for their potential use in common Structural Health Monitoring (SHM) procedures based on dynamic monitoring. The analysis involved striking the strand with a hammer blow and suspending a weight (3.75 kg) at the center, which was then instantaneously released, inducing an elastic oscillation.

For hammer blow measurements, tests were conducted with three different decreasing tension levels, as further slackening of the applied tension would introduce excessive noise in the acquired experimental data. Hanging weight measurements involved increasing the strain on the multi-wire cable. In both tests, Fast Fourier Transforms (FFTs) were assessed, revealing a strong correlation between the frequency values of the FFT peaks and the tensioning levels. This correlation was expected based on the basic theory of vibrating strings but was experimentally validated to confirm the suitability of the smart saddle sensor for frequency-based SHM techniques.

Figure 49.a & b, the time traces of the wavelength variations of FBG1 installed on the steel strand for both experiments are presented, while in

Figure 49.c & d, the FFTs of the time signals from the dynamic tests are displayed. Figure 50 employs interpolation with the least-square method to establish a correlation between the frequencies of the first peak and the tension applied to the strand. Similar to static measurements, only FBG1 is shown for dynamic ones since FBG2 and FBG3 exhibit comparable behavior.

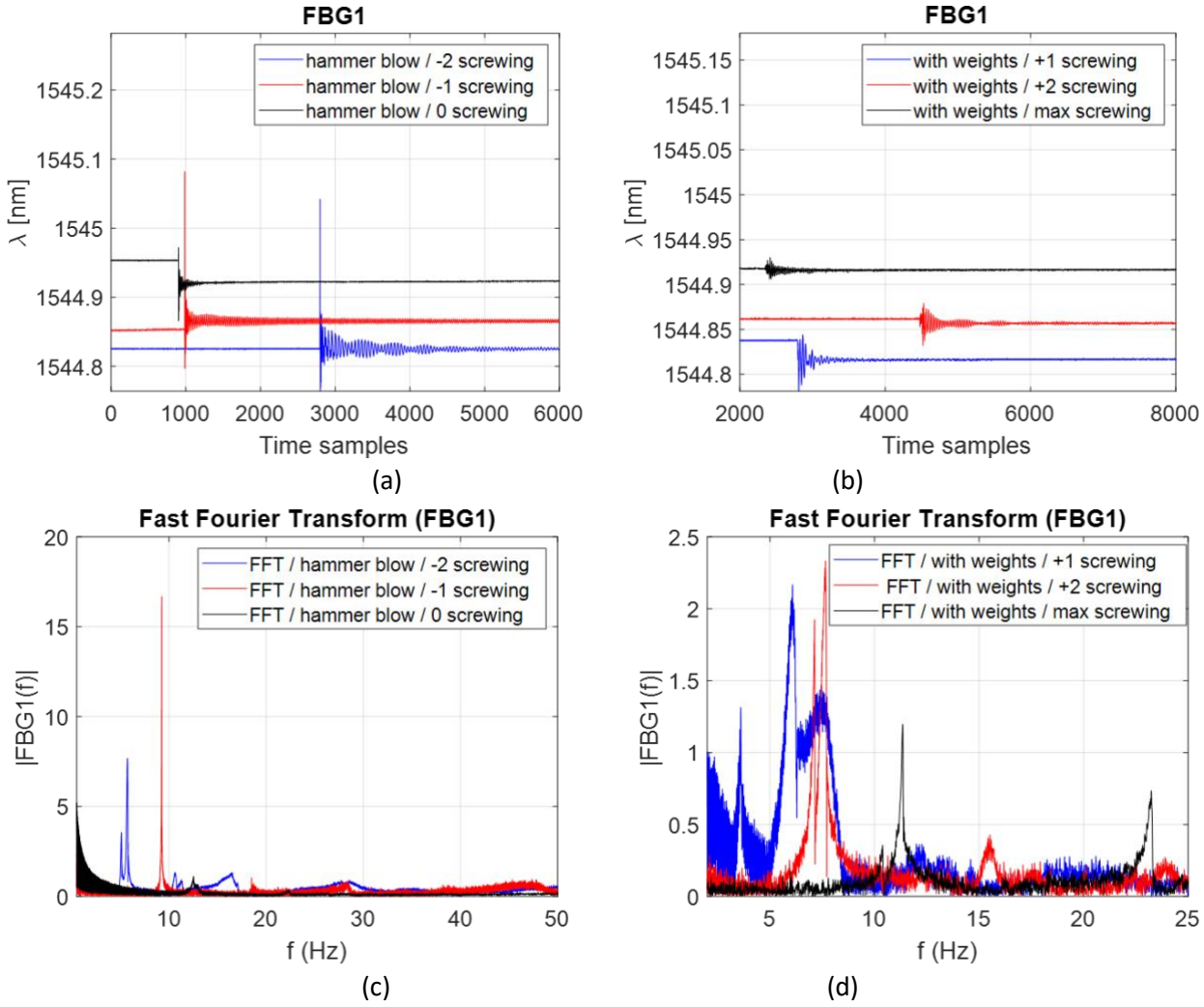

Figure 49. Time behavior of wavelength and FFTs with different tensioning (increasing and decreasing) levels of FBG1 for (a-c) hammer blow experiments and (b-d) hanging weights tests.

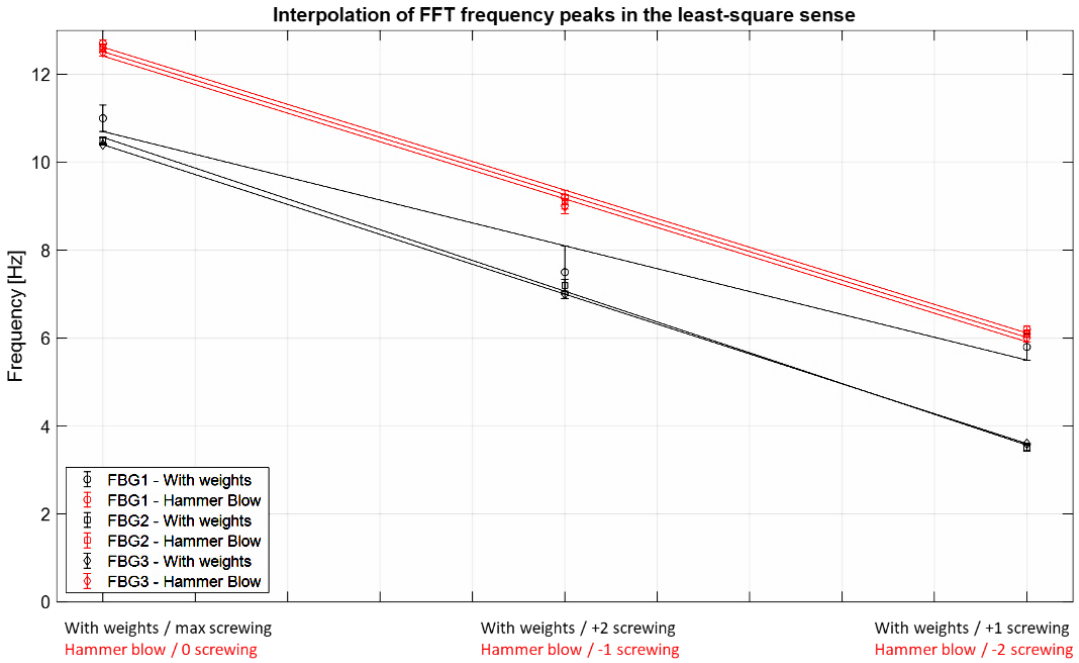

Figure 50. Interpolating curves (in the least-square sense) of FFTs frequency peaks with tensioning levels.

The results of the static tests indicate that as the stretch is slackened, the wavelengths exhibit a decreasing trend, while an increase in screwing leads to a rise in wavelengths. Dynamic tests were carried out by striking the strand with a sharp blow or by suspending a weight at the center to induce elastic oscillation. To analyze the dynamic behavior of the strand, a spectral analysis was conducted. As per the results of the spectral analysis, the frequency values at which the FFTs are located scale proportionally to the applied tension.

Bending test

In order to better understand the behavior of smart saddles and FBG sensors during bending condition, two bending tests have been performed. The strands which are used in thermal test are also used in these bending tests; the FBG sensors number 1 and 2 have been bonded on strand surfaces.

For each strand, the bending test has been performed in two phases as shown in Figure 51. In the first phase (Figure 51.a), during applying load, the position of the smart saddle is on the top of strand. Therefore, the FBG sensor is in compression condition during the test. In the second phase as depicted in Figure 51b, the smart saddle is placed in the bottom of strand and during the test is in tension condition.

a) b)

Figure 51. The smart saddle on the a) top and b) bottom of strand during the bending test.

The bending machine can apply a maximum force of about 1000N at the speed of 0.5 mm/min. The force has been applied during 30 cycles for tests. The results of displacement against force on the strand with smart saddle number 3, as shown in Figure 52 when FBG sensor is in compression condition. The maximum force of about 300N has applied in this test and the displacement during the test is reported in Figure 52.

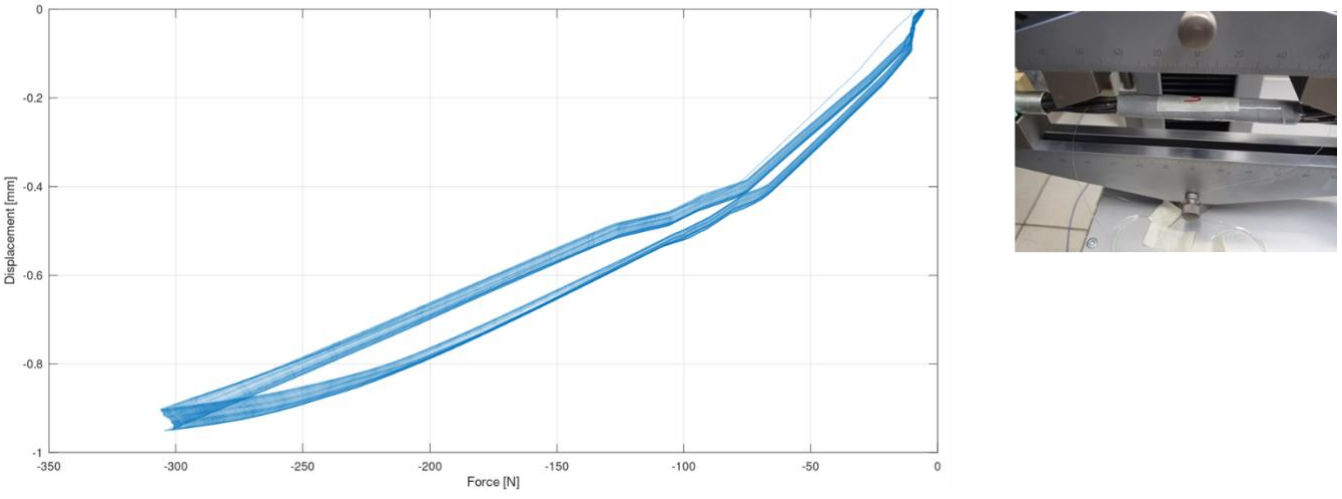

Figure 52. The displacement during test. The smart saddle number 3 has been in compression condition.

The Figure 53 illustrates the wavelength shift read by FBG sensor during test. In this test as expected, the FBG sensor recorded negative wavelength shift because the sensor is in compression condition.

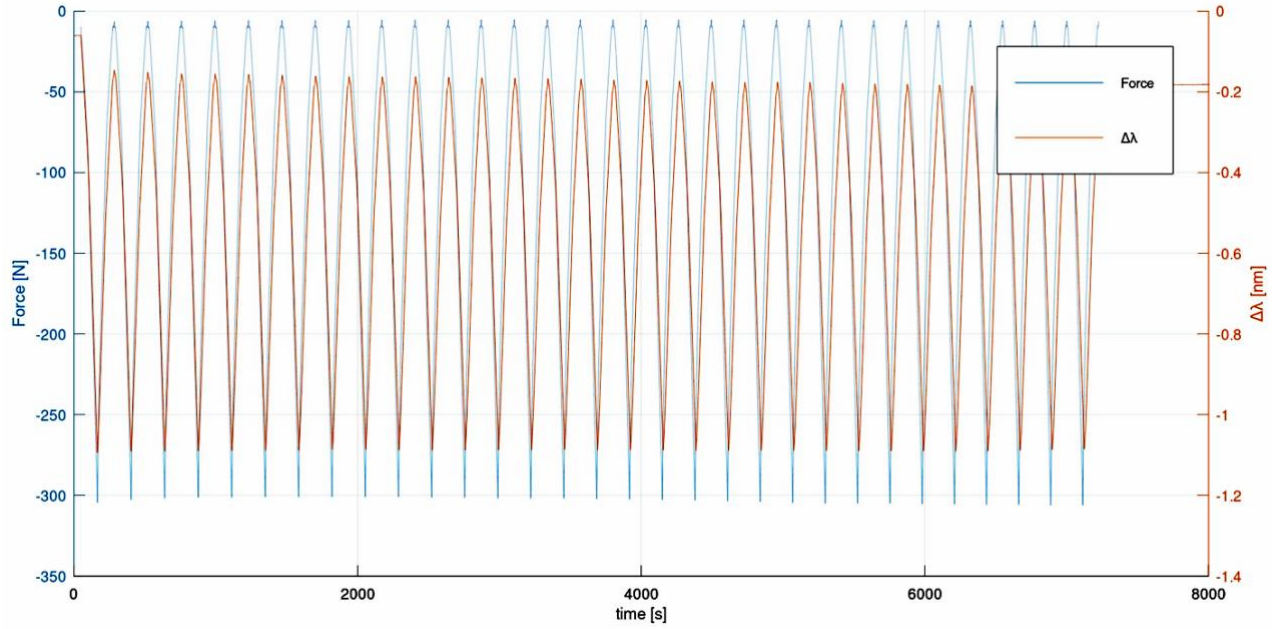

Figure 53.The wavelength shift against force during the test.

The variation of wavelength shift against displacement during 30 cycles of applying the force is depicted in Figure 54.

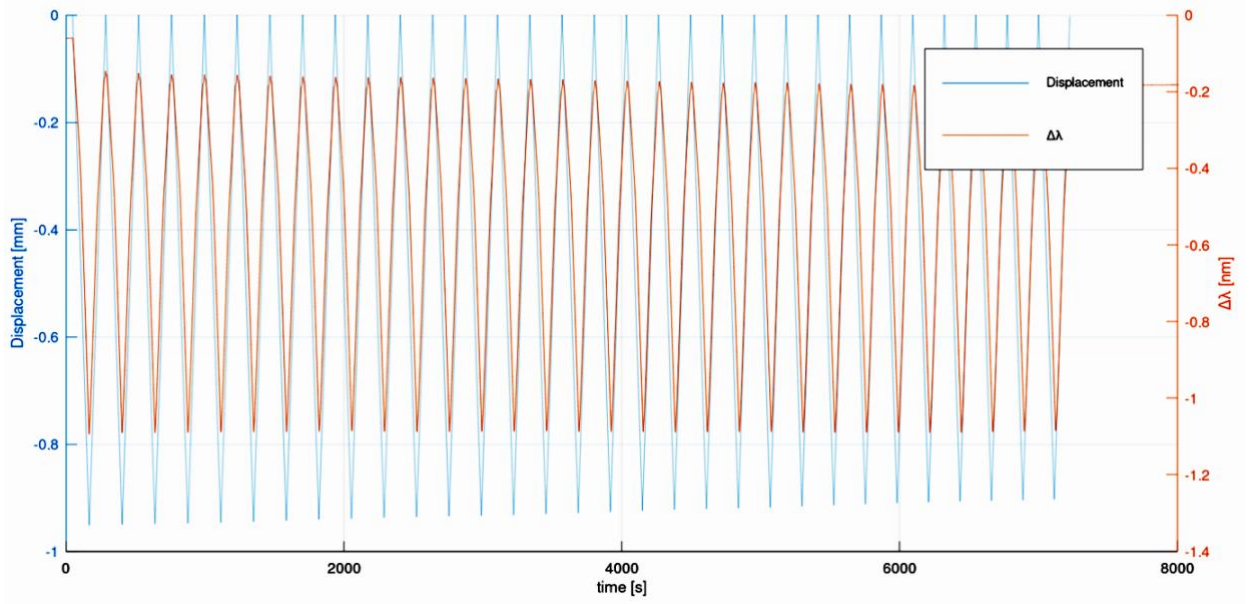

Figure 54.The wavelength shift against displacement during test.

The Figure 55 reports that the drift of wavelength shift in each cycle of applying force is small and it decreased as a consequence of cycle number increased. Moreover, FBG sensor can read wavelength during cyclic bending test perfectly.

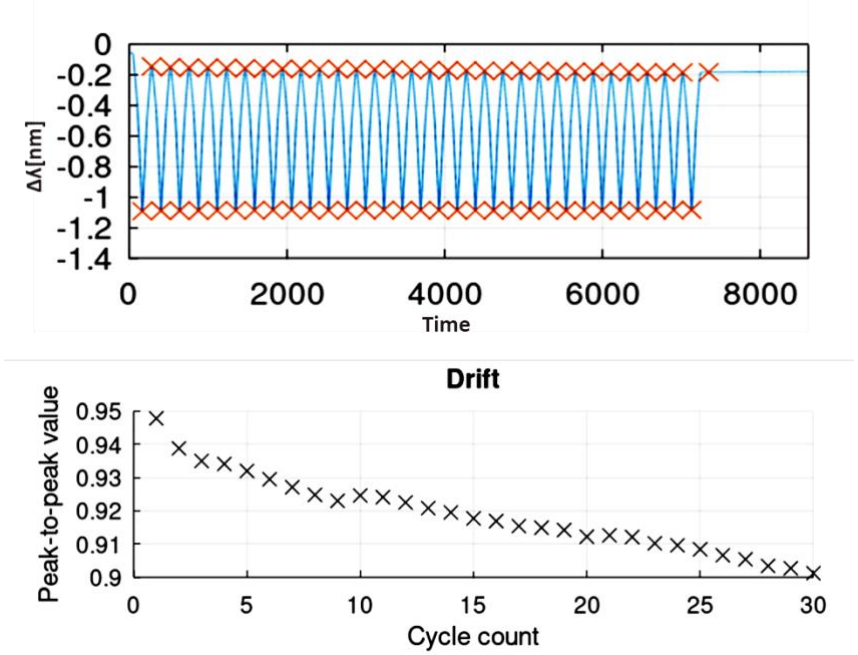

Figure 55. The drift of wavelength shift during 30 cycles of applying force.

When the smart saddle has been placed at the bottom of the strand, the FBG sensor has been in tension condition and the displacement against force reported in Figure 56. The maximum force of this cyclic bending test has been applied about 240 N.

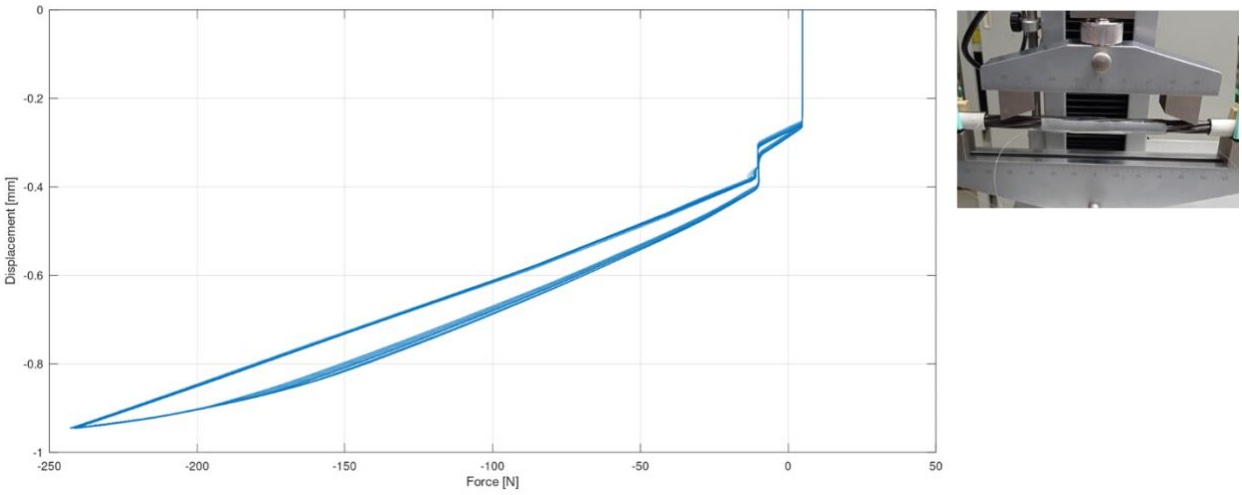

Figure 56.The displacement during applying the force in cylices.

The FBG sensor has been read the positive wavelength shift because the sensor is in tension condition in this test. When the maximum force applied on the strain (240 N) the FBG sensor number 3 has read the wavelength about 0.8 nm as shown in Figure 57.

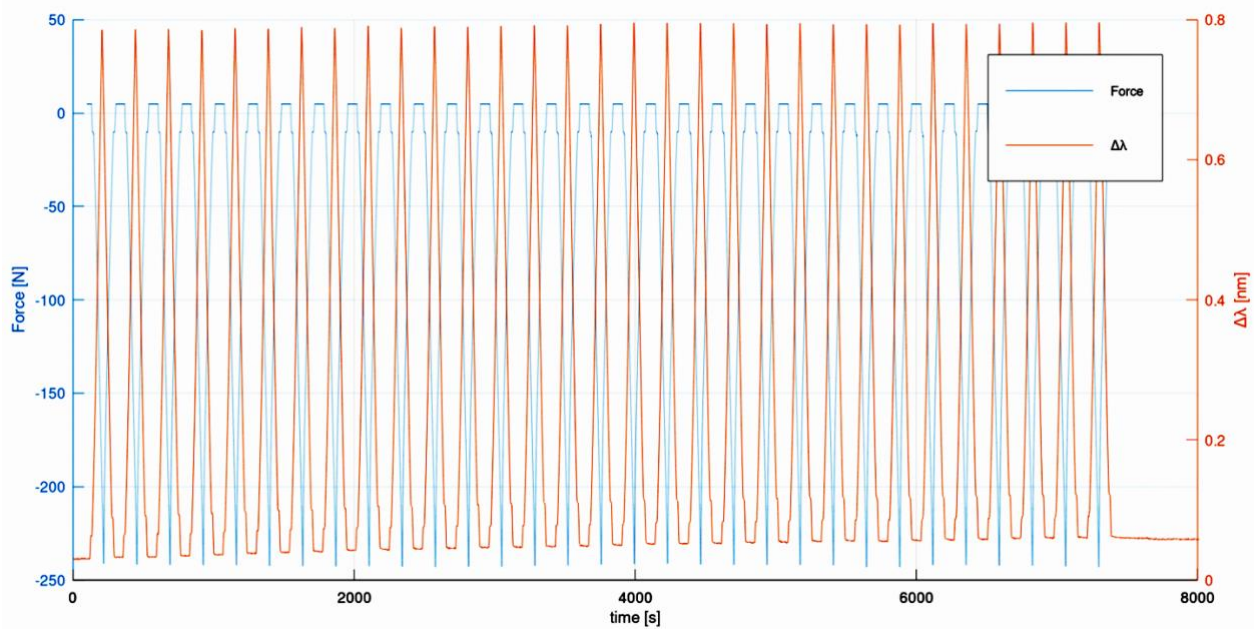

Figure 57. The variation of wavelength during the test.

The Figure 58 illustrates the displacement during test against the wavelength shift for all cycles of applying the force.

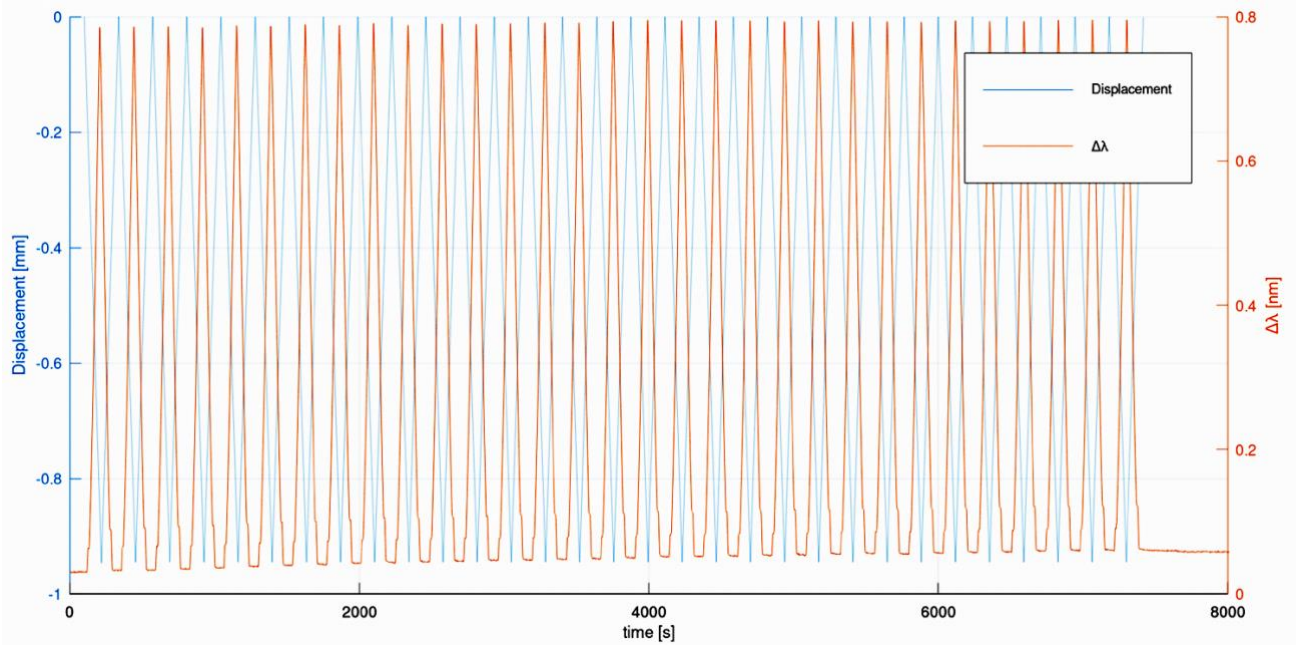

Figure 58.The displacement against wavelength shift during the experiment.

The Figure 59 reported that the drift of wavelength shift in each cycle of applying force is small and it decreased as a consequence of cycle number increased. Moreover, the drift value of wavelength shift in this test is smaller than the previews test when the smart saddle has been on the top of strand.

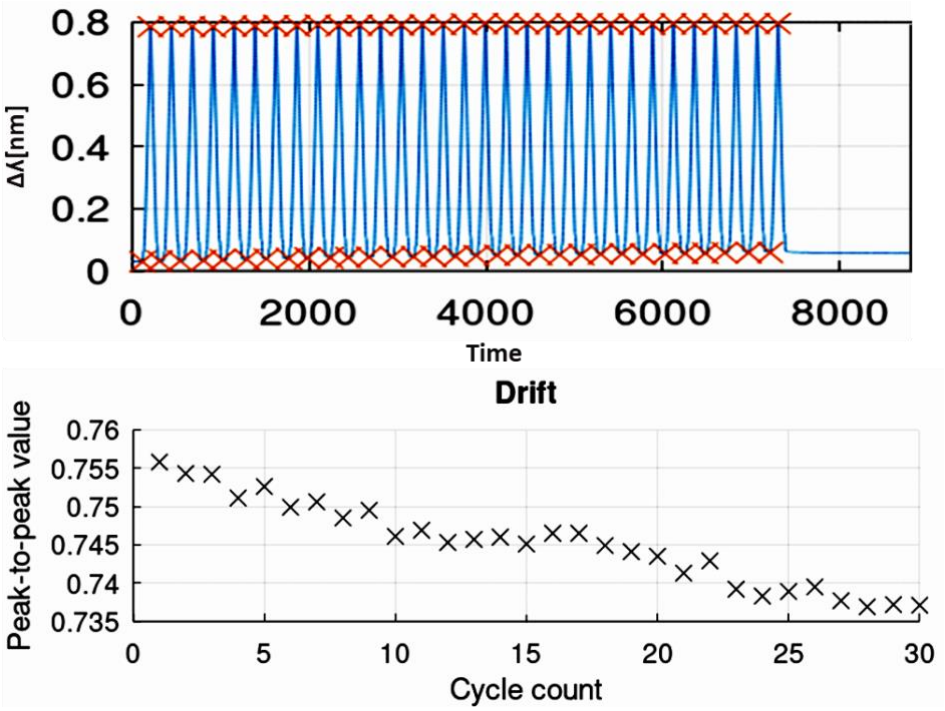

Figure 59.The drift of wavelength shift during 30 cycles of applying force.

Furthermore, two bending tests have been performed on strand with the smart saddle number 2. The smart saddle has been placed on the top and bottom of strand. The Figure 60 shows the displacement against applied force during the experiments. The maximum force has been applied about 700 N (Figure 60a), when the smart saddle was on the top of the strand with compression condition. In the other hand, when the smart saddle was in tension condition, the maximum applied force in each cycle was about 800 N as shown in Figure 60b.

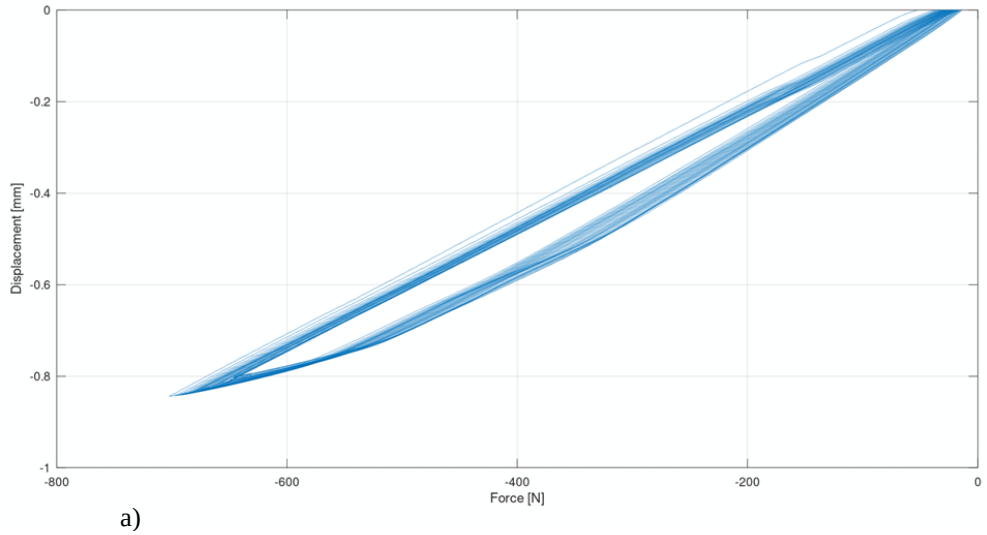

a)

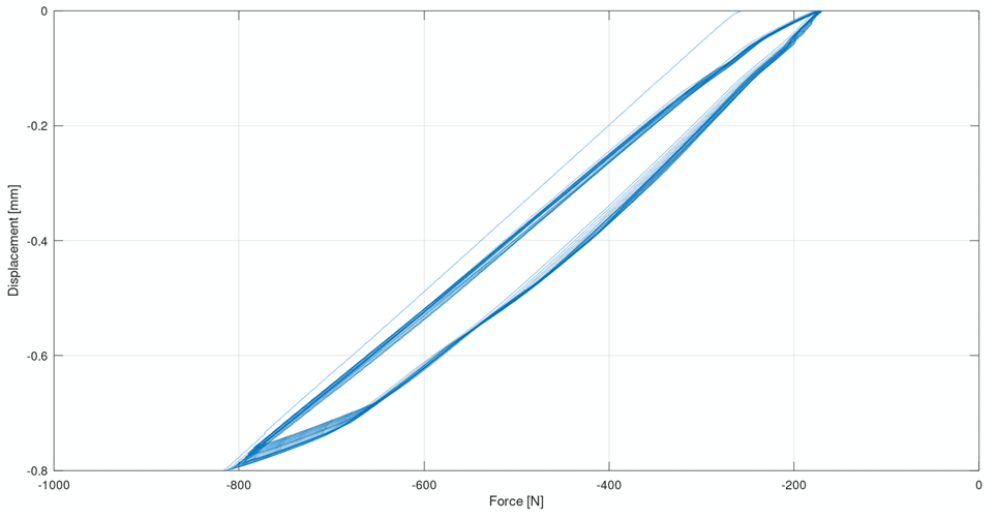

b)

Figure 60. The displacement against force, a) smart saddle at the top of strand and b) smart saddle at the bottom of strand.

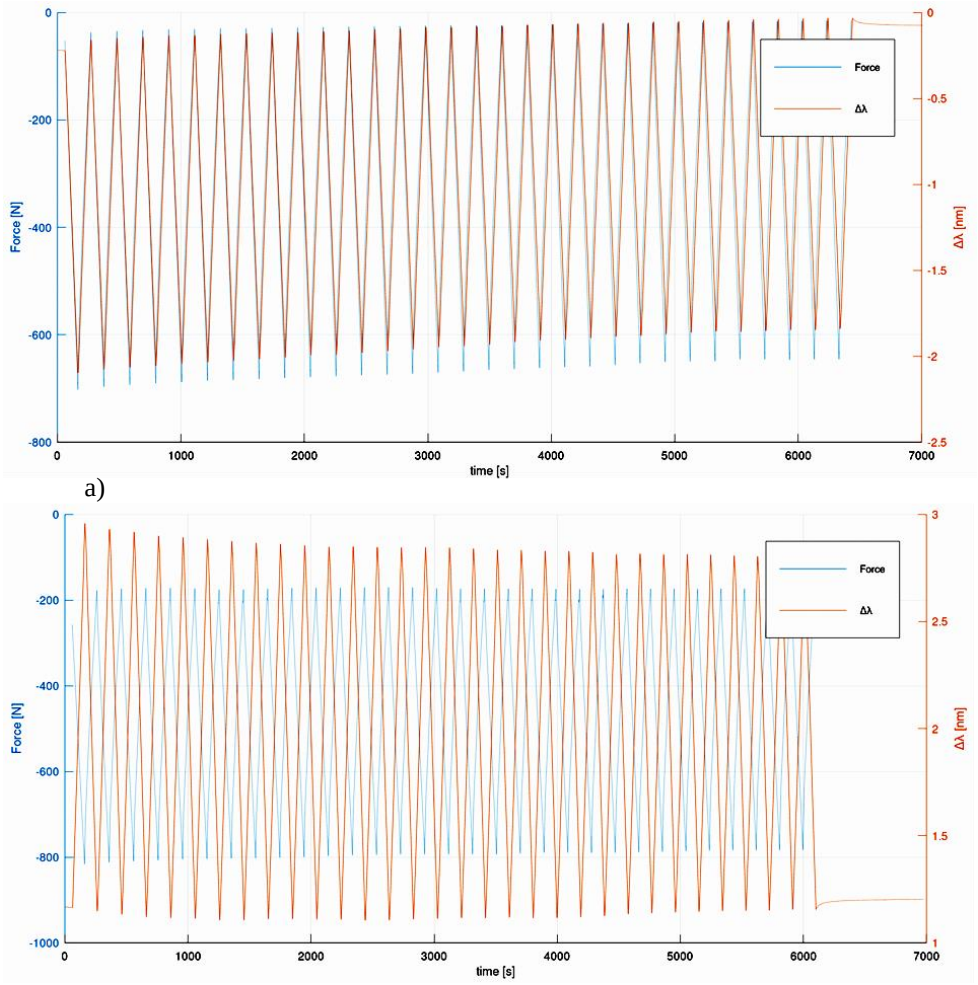

a)

b)

Figure 61.The wavelength shift during test, a) smart saddle at the top, b) smart saddle at the bottom of strand.

The Figure 61 is depicted the wavelength shift against force during the time for compression (Figure 61a) and extension (Figure 61b) condition of smart saddle.

The wavelength shifts against displacement during applying the force during 30 cycles as shown in Figure 62 for both tests.

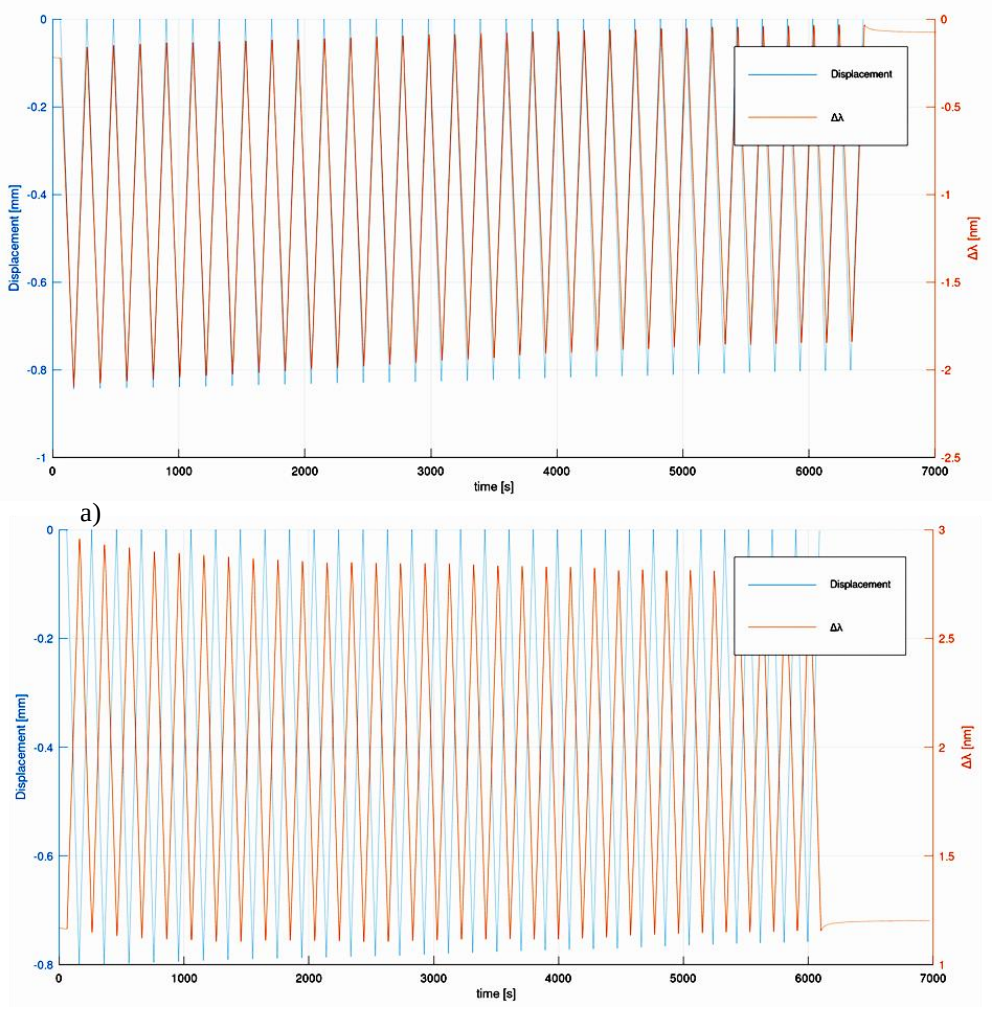

Figure 62. The wavelength shift against displacement during test, a) smart saddle at the top, b) smart saddle at the bottom of strand.

The Figure 63 reported that the drift of wavelength shift in each cycle decreased as a consequence of cycle number increased but the value of drift is bigger than previews bending test on smart saddle number 2 because the applying force is bigger.

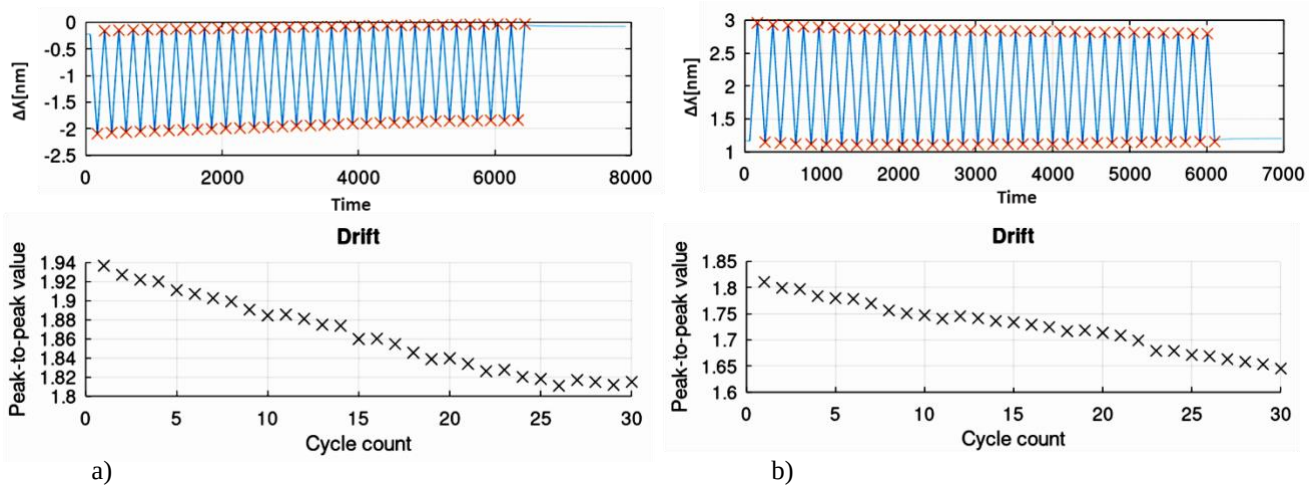

Figure 63. The drift of wavelength shift in each cycle, a) smart saddle at the top, b) smart saddle at the bottom of strand.

Tests with the heavy hanging

The aim of the dynamic investigations is to experimentally identify the free frequencies of vibration: indeed the dynamic parameters, being linked to all the geometric and mechanical elements of the structure, represent a valid tool for controlling any variation in the general conditions over time.

The motivation is to verify the possibility of appreciating the variation in voltage from the variation in the natural frequency (we would say 'resonant' for a model, in practice for real objects we use 'operational'). The perspective is the dynamic analysis for Structural Health Monitoring which identifies a de-tensioning of the cable (or other alteration of the beam as a whole) from the variation of its own vibration frequency. At this purpose an experimental set up was realized in the ENEA FRASCATI research center, by hanging a heavy on a real strand. By varying the heavy as well as by applying striking with a sharp blow, the behavior of the strand is studied. In

Figure 64 and Figure 65 the experimental set up is shown.

Figure 64. On the left: attachment of the heavy to the strand; in the middle: tensioning of the cable using the overhead crane; at right: progressive increase in load using lead blocks of 11.34 kg each.

Figure 65.On the left: progressive increase in load using lead blocks heavy to the strand; in the middle: the overhead crane that supports tensioned cable; at right: dynamic test by striking with a sharp blow.

In the following plots (Figure 66) the static $\Delta\lambda$ analysis for measurements of the cable is exposed.

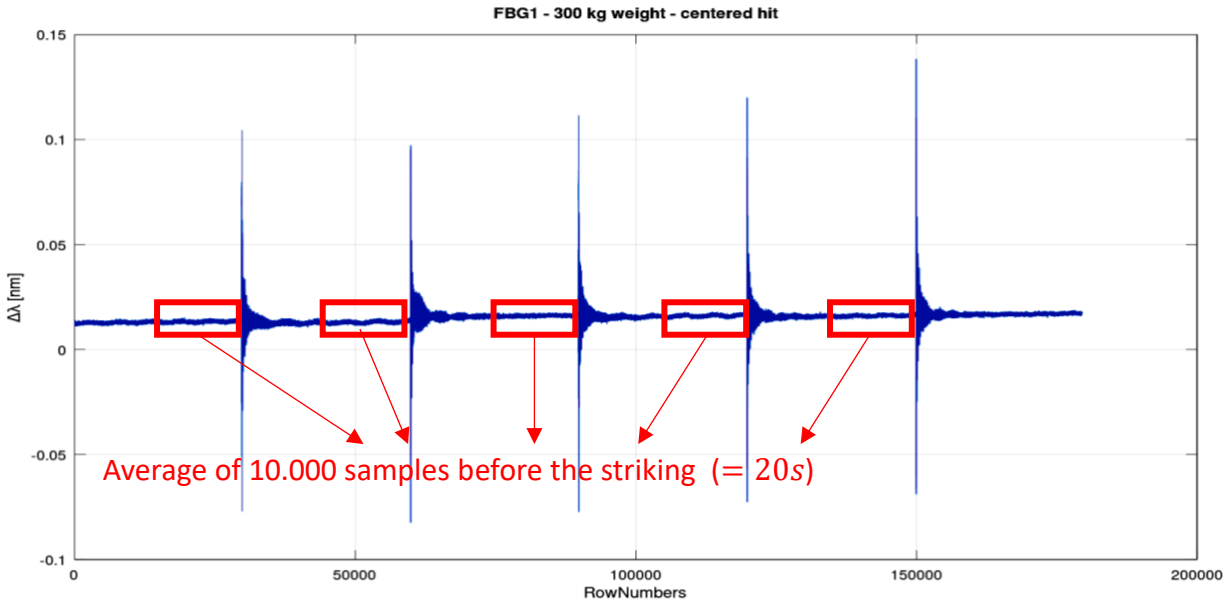

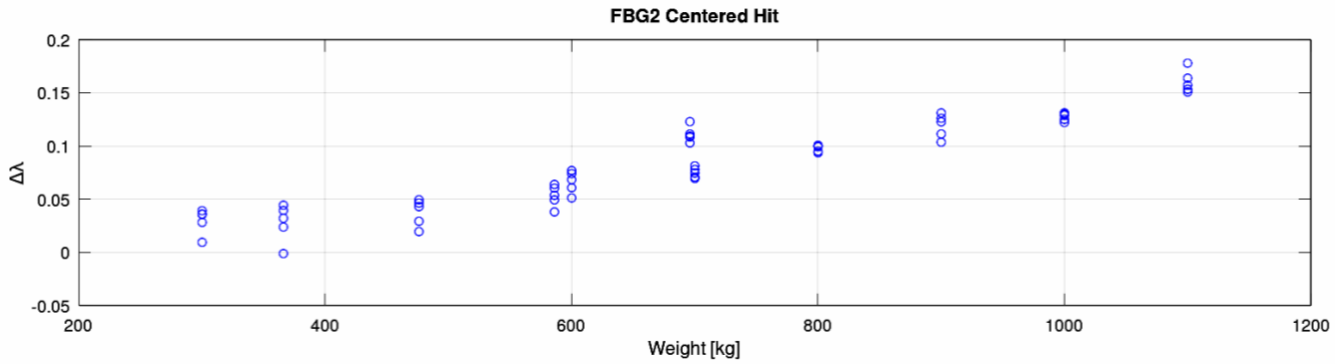
FBG2 Centered Hit
Δλ
Weight [kg]

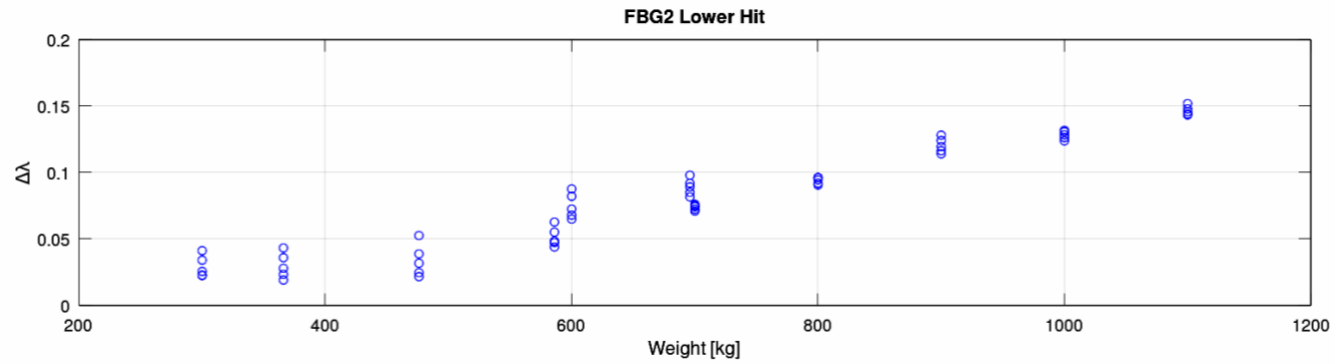
FBG2 Lower Hit
Δλ
Weight [kg]

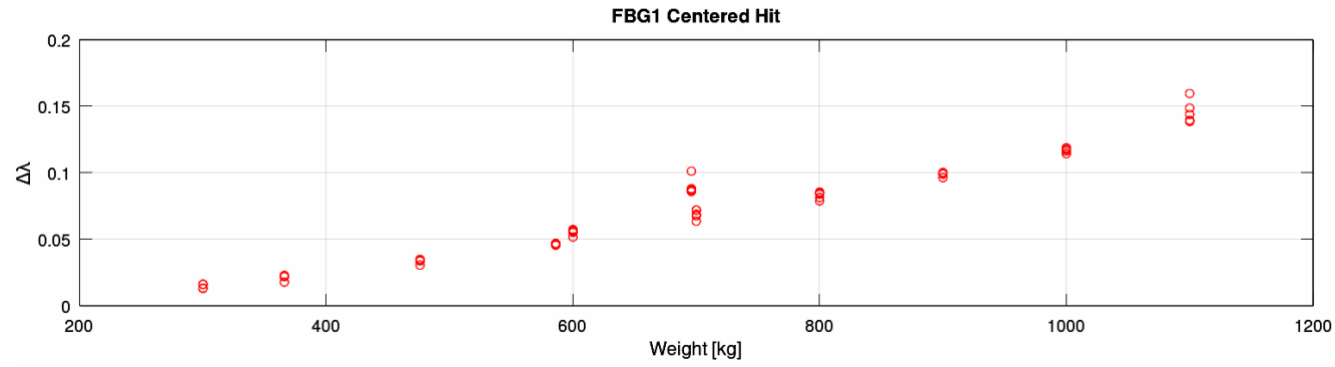
FBG1 Centered Hit
Δλ
Weight [kg]

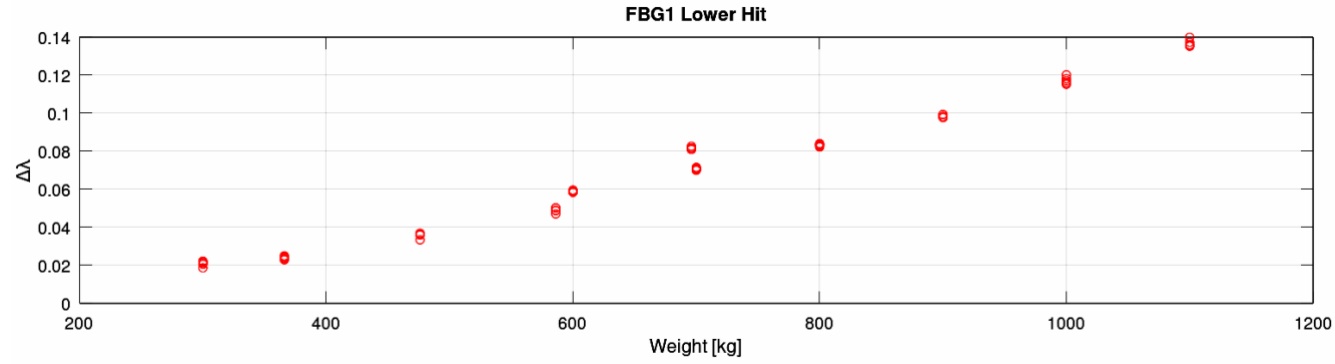
FBG1 Lower Hit
Δλ
Weight [kg]

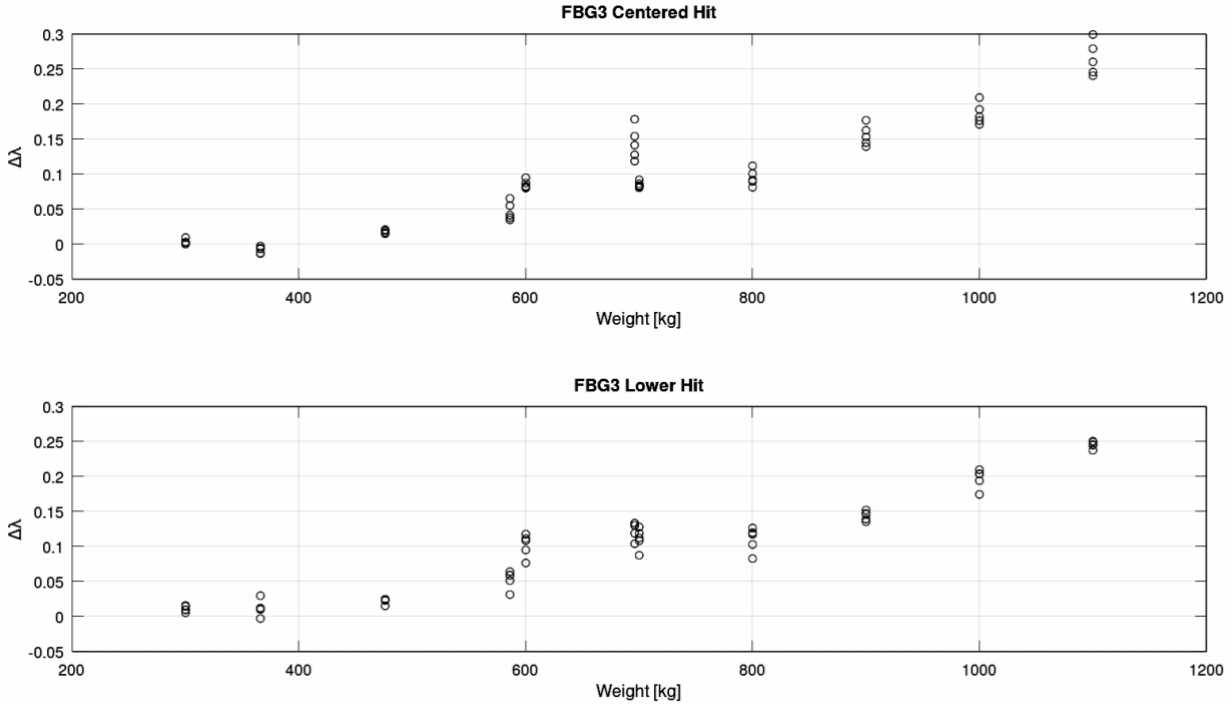

Figure 66. For each FBG an increase in the resting wavelength with weight is identifiable.

Finally, the frequency behavior, through spectral analysis using FFT: Fast Fourier Transform is shown in the plots of Figure 67.

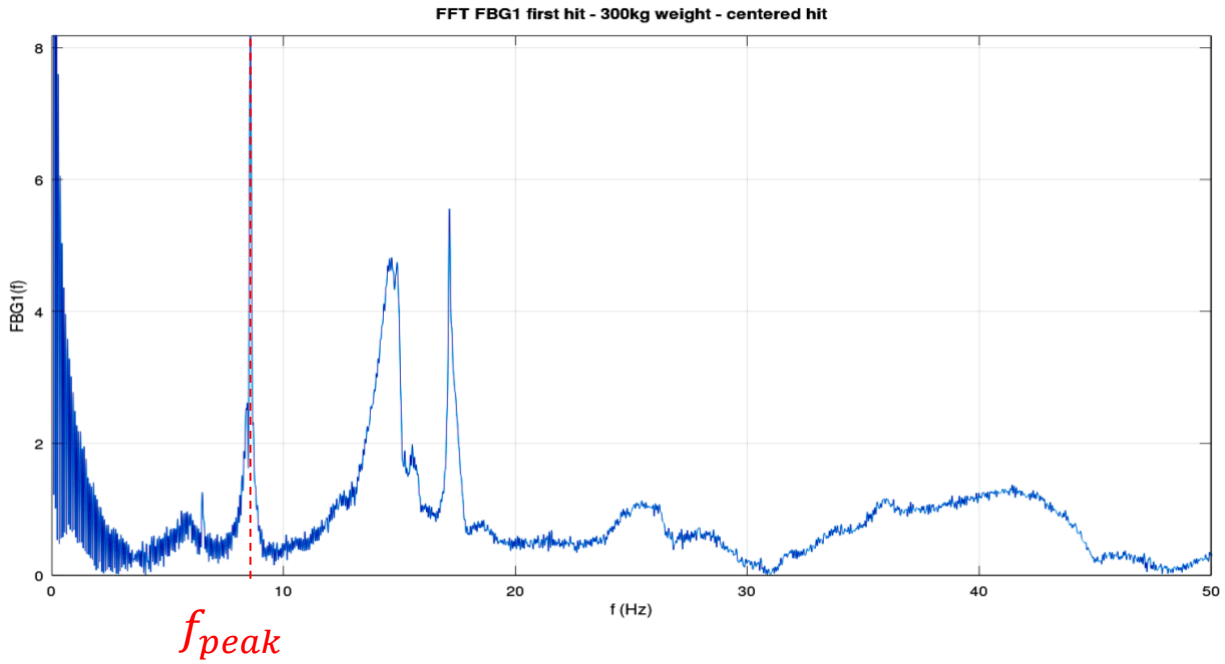

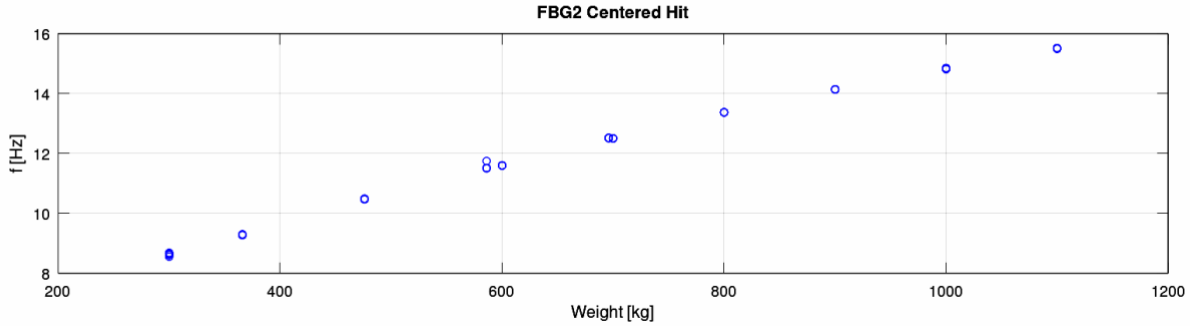
FBG2 Centered Hit
f [Hz]
Weight [kg]

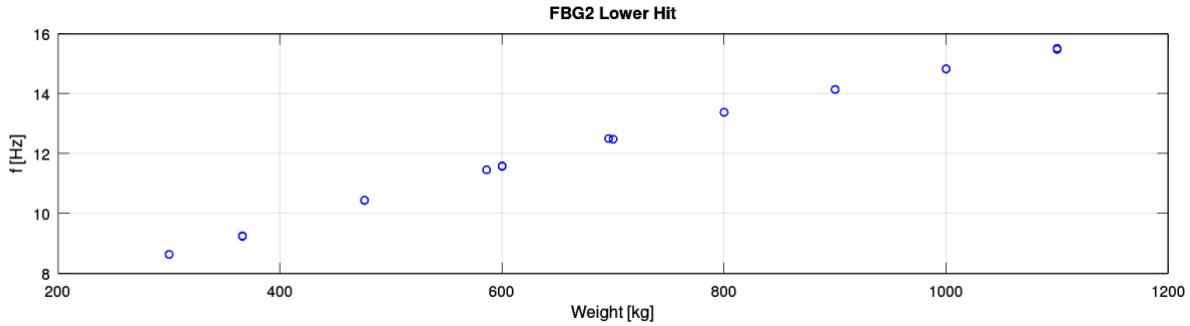
FBG2 Lower Hit
f [Hz]
Weight [kg]

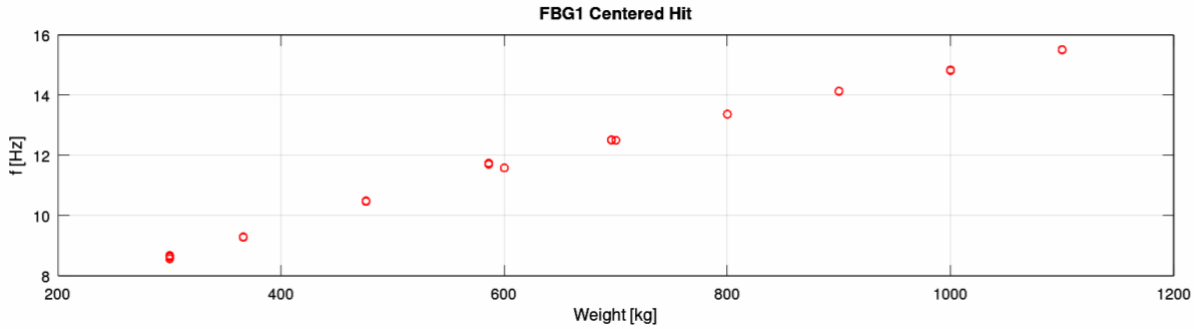
FBG1 Centered Hit
f [Hz]
Weight [kg]

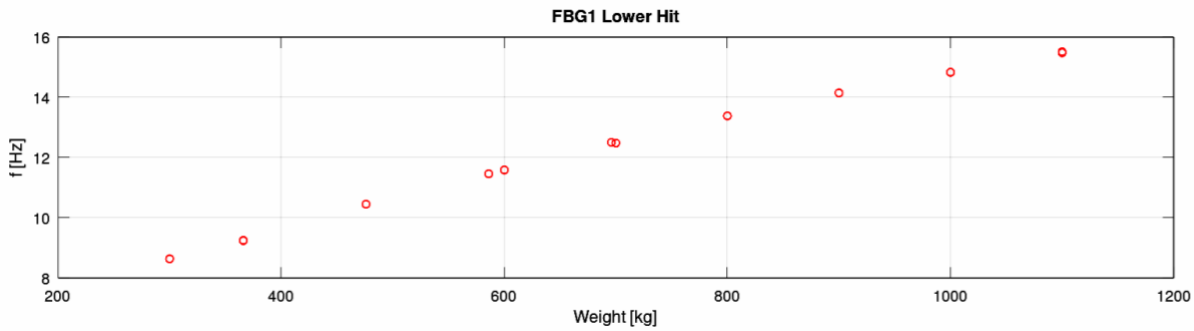
FBG1 Lower Hit
f [Hz]
Weight [kg]

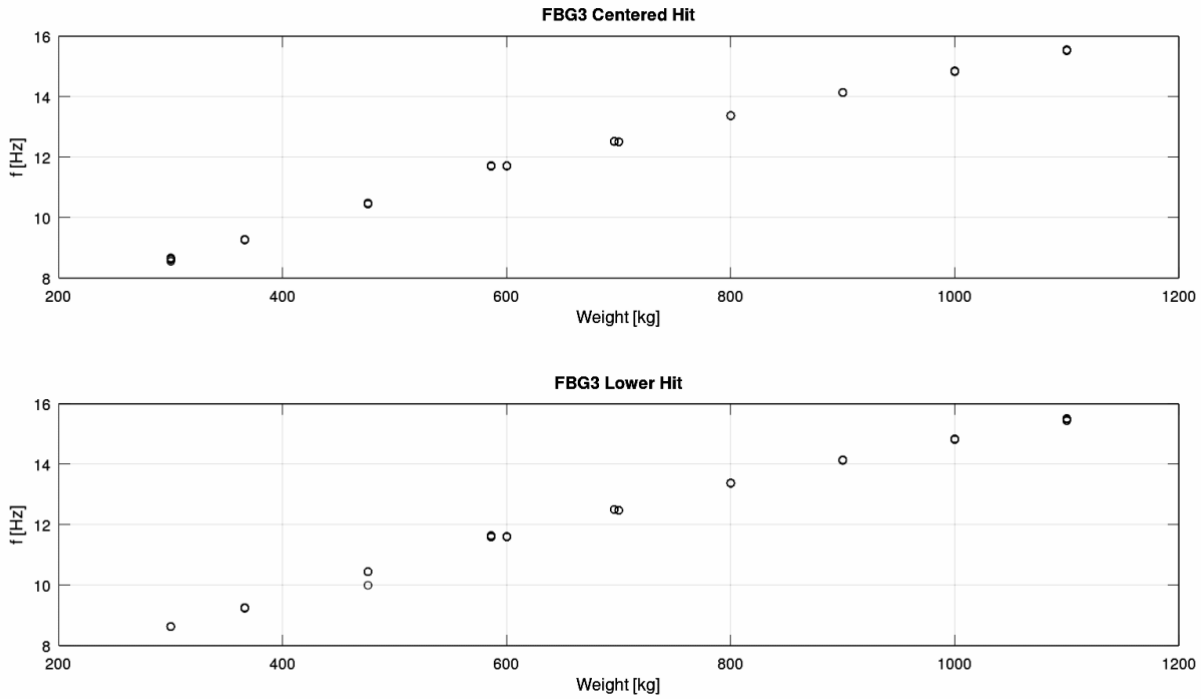

Figure 67: For each FBG, an increase in the peak frequency of the Fourier transform is identifiable as the load increases.

Tensile tests on steel strand at Roma Tre university lab

In this section, the results of the tensile tests conducted using the MTS machine (Figure 68) at Roma Tre University on steel strands are presented. The wavelength variation is measured by the smart saddle for two strand samples. The samples are identical in every aspect. Each sample is equipped with three smart saddles, with lengths of 4cm, 3cm, and 4cm respectively, mounted on the strand at different positions (Figure 69). The extensometer is positioned on the mid smart saddle for direct strain measurement (Figure 70). The applied displacement tensile histories are shown in Figure 71.

Figure 68. MTS tensile test machine in Roma Tre University

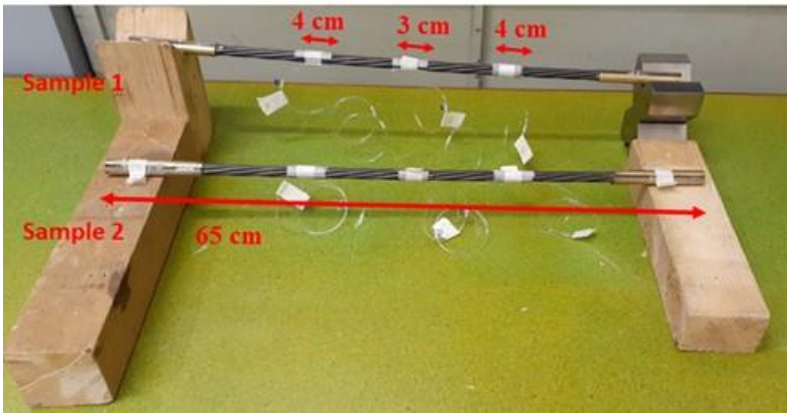

Figure 69. Strand Sample 1 and 2 equipped with 6 smart saddles

Figure 70. Extensometer positioning for direct strain measurement

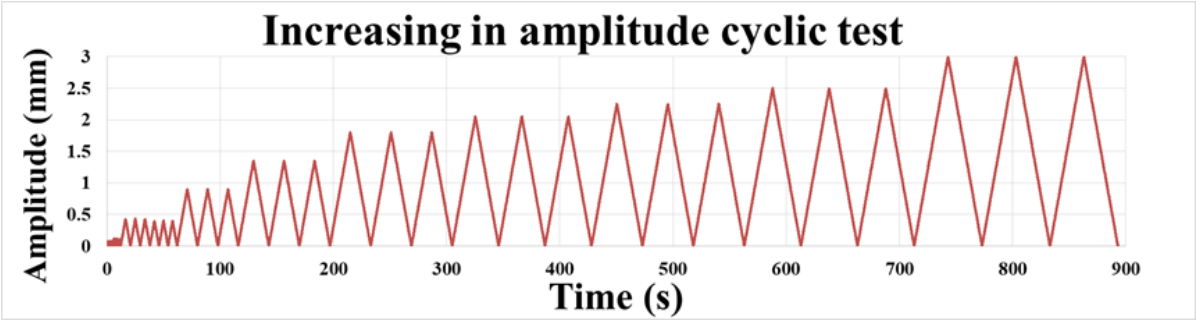

a) Displacement Load history test 1

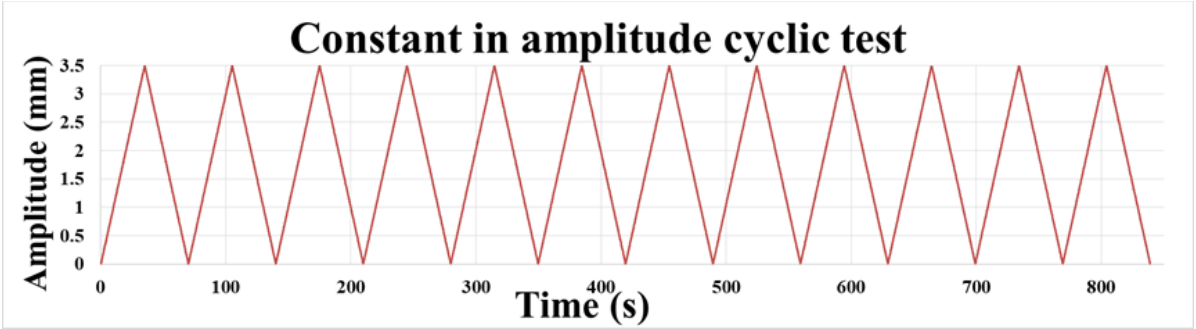

b) Displacement Load history for test 2

Figure 71. Displacement tensile histories

The tensile results on two samples are illustrated in Figure 72. The smart saddles are produced based on the basic procedure. It is evident that differences exist between the results obtained from the MTS machine and those from the extensometer. These differences primarily arises from factors such as machine head deflection and the non-uniform distribution of strain along the strand in the grip zones.

The measurements from the top smart saddles often yield irrational values. Notably, the maximum percentage difference between measurements taken at the bottom and middle positions is approximately 10% (Test01, figure 72.b). Although, the extensometer has not measured negative strains (Figure 72.a), but negative values recorded by the smart saddles indicate that the smart saddles undergo compression during testing. This event is likely related to the smart saddle or its interface glue structural responses evolution.

In Test02 conducted on sample 1, it was observed that the differences between measurements increased over time, indicating a nonlinear behavior of smart saddle. This suggests that either the smart saddle or the interface glue experienced some form of deterioration or breakage, as illustrated in Figure 72.d. Furthermore, it was noted that after a certain number of cycles, the extensometer values began to slip, thus its data unreliable for further analysis.

In the test conducted on sample 2, negative values were once again measured by the smart saddles (Figure 72 e & f). However, this time, the extensometer also recorded some small negative values, indicating that the strand experienced compression. This phenomenon can be attributed to strand slippage within the machine grips. When the machine head moves upwards, the strands slip from their grip, experiencing no tension. Conversely, when the machine head moves downwards, the grips and anchorage system function more effectively, exerting compression on the strand without any slippage between the strand and the grips. Nonetheless, the max percentage difference in $\Delta\lambda$ relative to bottom smart saddle is %20 and %26 for mid and top smart saddles respectively (Figure 72.f). These percentages remain relatively constant across all time instances.

The maximum percentage difference in $\Delta\lambda$ relative to the bottom smart saddle is 30%, while it increases to 63% for the mid smart saddle and top smart saddle, respectively, in Test02 (Figure 72.h). Comparing these values with those of Test01, where the maximum percentage differences were lower. This indicates that smart saddles might be damaged more in the Test01 last cycle, but this difference remains constant across all time instances (Figure 72.h). Moreover, it appears that the strand undergoes compression after some initial cycles in the testing process.

Furthermore, in both samples, no significant correlation was found between the measurements of the 3cm smart saddles and the 4cm smart saddles. This suggests that geometric differences between the two sizes do not have a notable effect on the observed measurements.

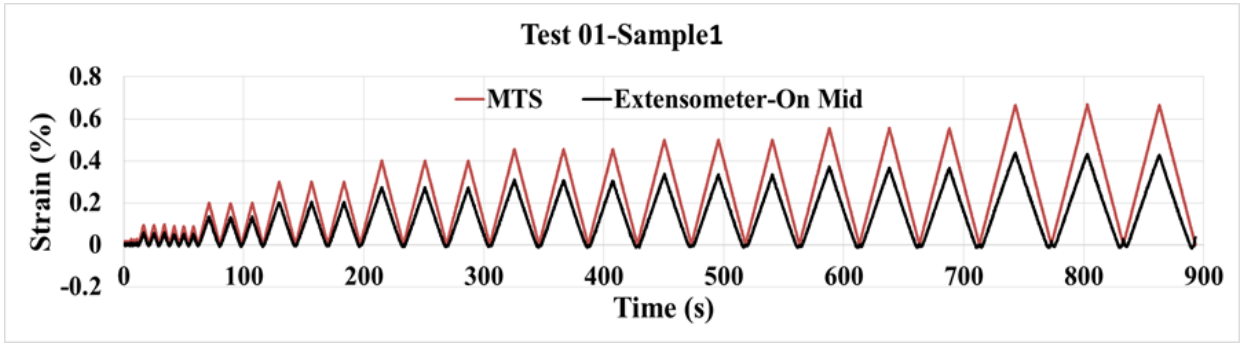

a) Extensometer and MTS machine strain results in Test01 on Sample1

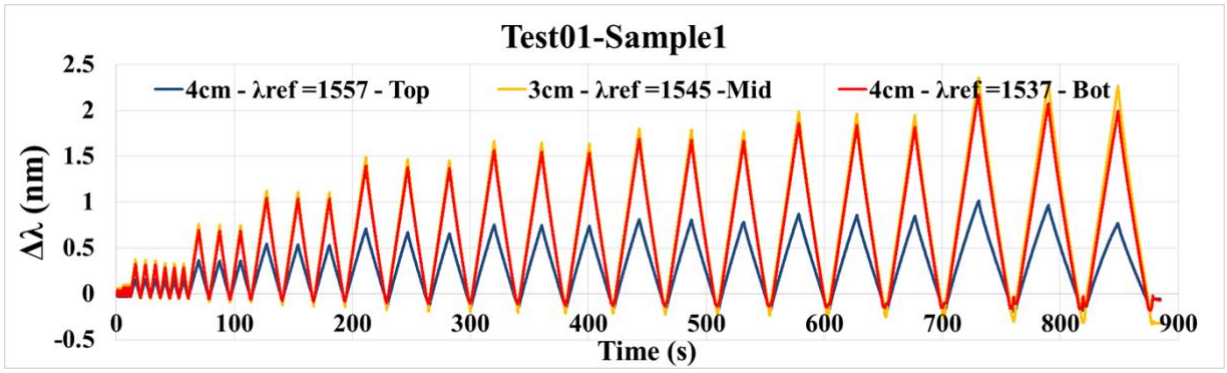

b) Wavelength variation measured by smart saddles in Test01 on Sample1

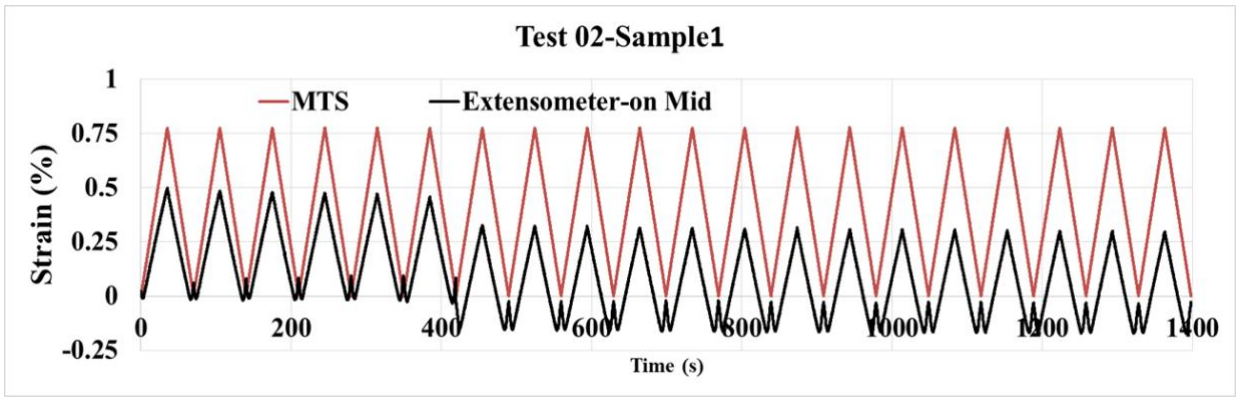

c) Extensometer and MTS machine strain results in Test02 on Sample1

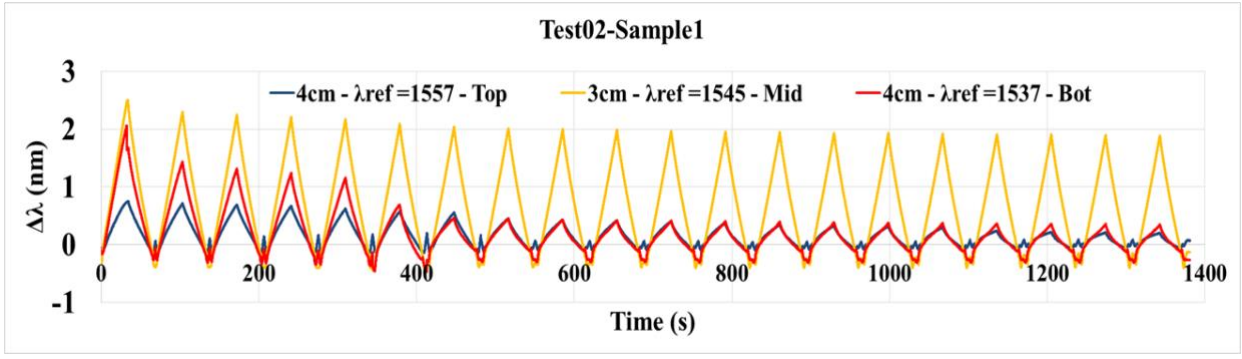

d) Wavelength variation measured by smart saddles in Test02 on Sample1

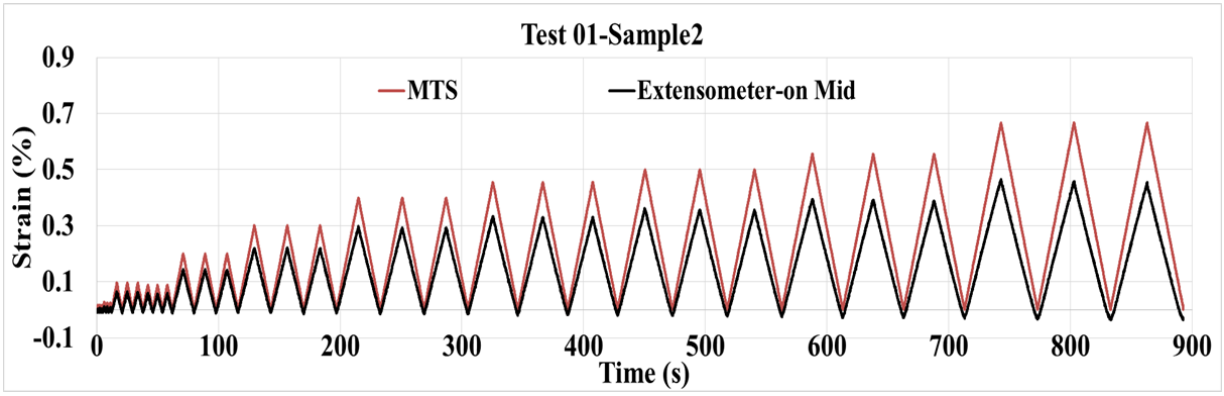

e) Extensometer and MTS machine strain results in Test01 on Smaple2

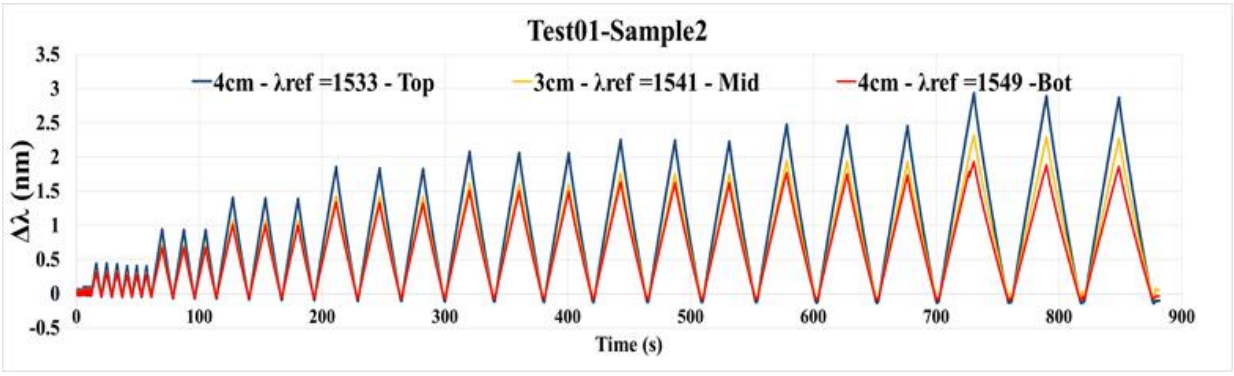

f) Wavelength variation measured by smart saddles in Test01 on Sample2

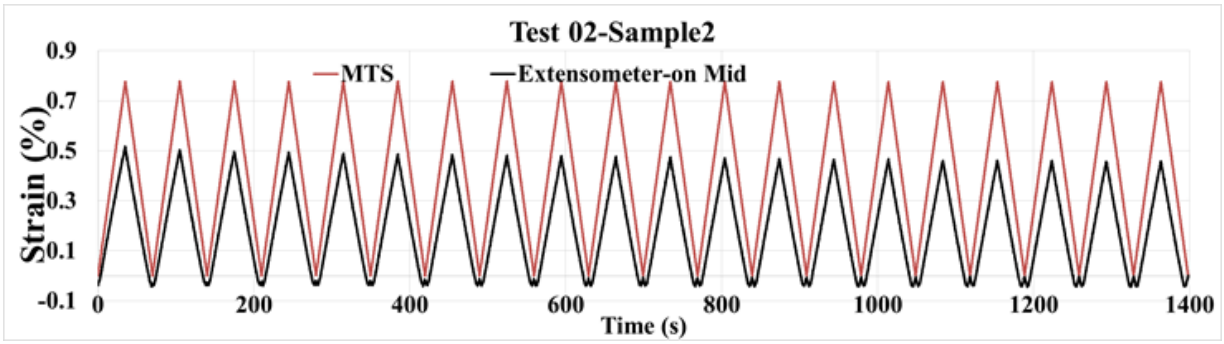

g) Extensometer and MTS machine strain results in Test02 on Sample2

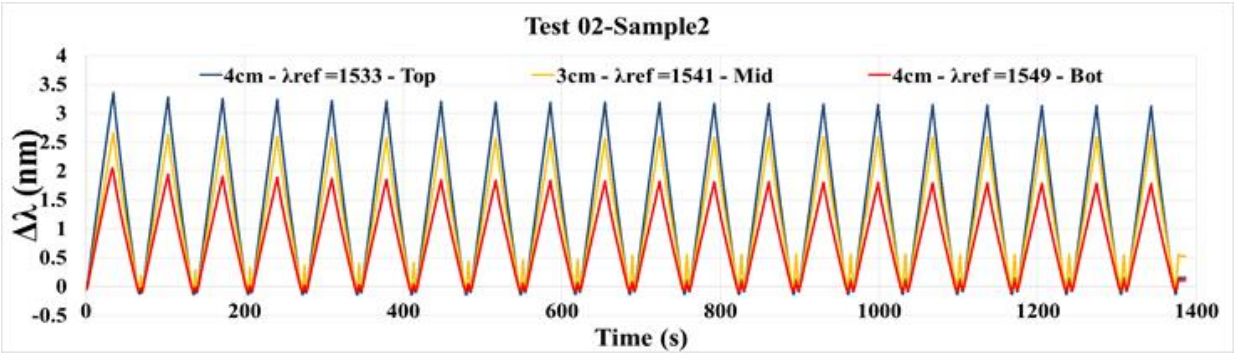

h) Wavelength variation measured by smart saddles in Test02 on Sample2

Figure 72. The tensile test results for samples 1 and 2

Improving production procedure and supplementary tensile tests

The basic production procedure introduces challenges due to the brittleness and vulnerability of the unprotected fiber. Deviations or bends in the fiber during wrapping are unacceptable as they lead to measurement errors. Additionally, the inability to visually monitor the entire wrapping process may result in incomplete resin coverage over the fiber. Tensile test results indicate inconsistencies between smart saddle measurements, with differences increasing with the number of cycles. This uncertainty surrounding smart saddle production introduces errors in measurements, highlighting the need for a thorough revision and improvement of the production procedure.

Production Procedure#2

In order to eliminate the above-mentioned problems, the second procedure is here introduced. In this new procedure it was tried to apply a modest pre-tensioning load using 190gr weight (Figure 75). The application of pre-stressing fiber not only helps to keep the fiber straight but also improves its spectral characteristics, thereby increasing the accuracy of measurement. Therefore, the steps for this procedure are similar to the previous procedure except a new step is added before wrapping the two polyester layers above the FBG sensor. It means, at first, two layers of impregnated polyester paper Sikadur-330 resin wrapped around the strand and then bare FBG sensor is placed in the middle of the paper and stretched via a mechanism works with weight. In the next step, the paper is wrapped in two additional layers to provide a protective thickness above the FBG sensor.

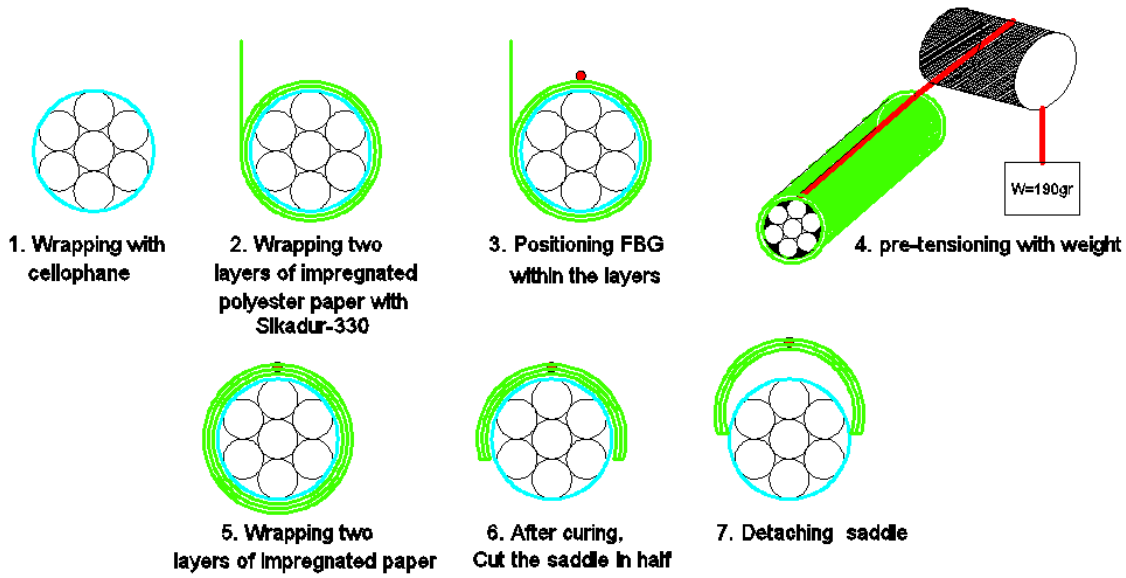

Figure 73. The first hypothesis for procedure#2

This hypothesis was examined in terms of production difficulties and it is found that also applied weight keep the fiber straight along the axes but, again it is hard to work with bare fiber and potential for breaking is high. Furthermore, adjusting the fiber and applying the tensioning load

constitutes a complex mechanism that is not compatible with the industrialization purpose of smart saddle production.

Figure 74. First hypothesis for Procedure #2: Indicating a complex system

Considering the difficulties presented above, the production of the smart saddle according to the proposed procedure proves to be challenging and complex. Therefore, it is imperative to revise it. Based on this, it is necessary to introduce a new step in which the fiber is glued to the plain polyester paper. After the glue cures, the paper is impregnated with Sikadur-330 and wrapping it around the pipe formwork.

A new step is devised for adhering the fiber to the polyester paper. Firstly, the polyester paper is cut, and a 1cm portion of its length is folded to create two layers. Next, a line is drawn parallel to the width of the paper and centered along the folded part to serve as a guide for fiber placement. The paper is then laid on a plastic bed, and two steel plates are positioned on top, aligning the edges of the plates to create a groove along the folded part. The center of this groove coincides with the drawn line. The width of the groove is equal to the coating tube of the fiber. A thin layer of Sikadur-330 is applied onto the paper, and the fiber is positioned along the groove. Finally, a fine layer of Sikadur-330 is applied above the fiber. An important point to note is that the steel material must be wrapped with cellophane to facilitate their removal after the epoxy has cured. In the final step, one end of fiber is tensioned with weight and another end is fixed on the table with scotch tape. This procedure secures that tensioned fiber is fixed on the paper and after hardening of the epoxy resin, it is easier than before to wrap impregnated paper around the formwork pipe.

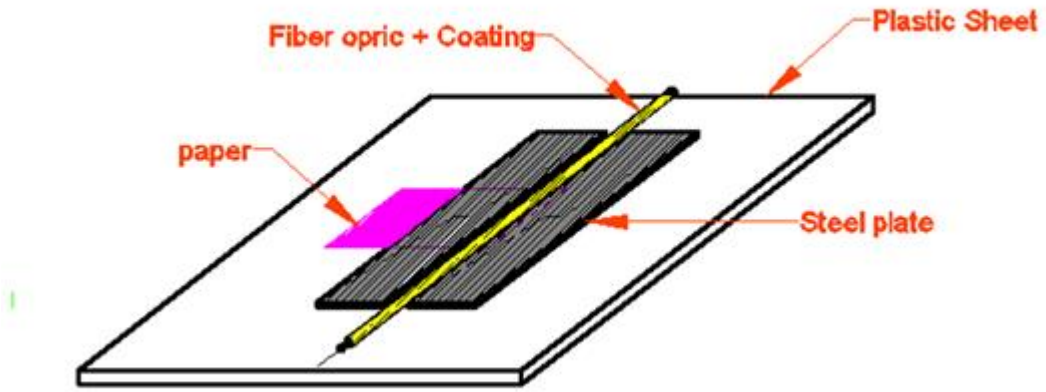

a) A new designed step to improve the procedure#2

b) Cutting the paper and draw guidelines

c) Creating the groove

d) Apply a thin line of epoxy and positioning fiber on the groove

e) Apply the weight fromone end

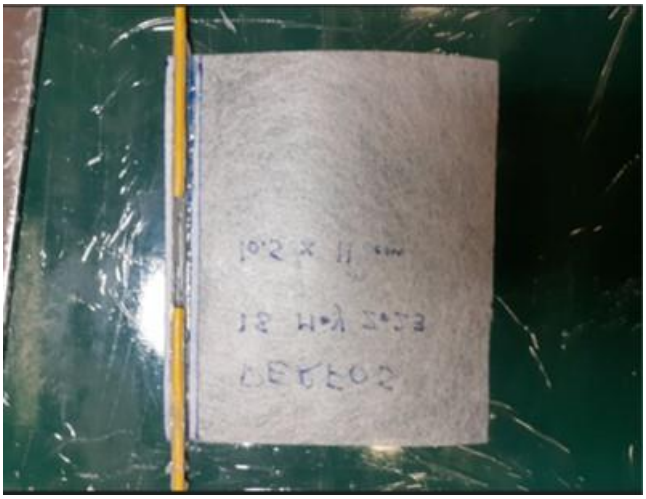

f) Final product

Figure 75. Detailed steps to make paper ready for wrapping

This product guarantee that fiber will not bended or deviated from the straight line of smart saddle and improve the production procedure. Also, this product removes the potential damage of fiber during the wrapping. On the other hand, this new step is time consuming for production and add a new step for production, in addition the new step needs at least 6 hours for curing and hardening of the epoxy resin. An important point to remember during the impregnation of the paper with

epoxy resin is to ensure that all faces are thoroughly impregnated, including the spaces between folded layers. Neglecting to apply epoxy resin between these layers may result in the formation of gaps, significantly impacting the performance of the smart saddle for measurement due to inadequate bonding.

Tensile Tests on strand with smart saddles (procedure#2)

Two strand samples (sample 3 and 4) have been prepared again for the tensile test using the MTS machine. Both samples are identical, and this time the length of the smart saddles is considered to be 4cm, 11cm, and 4cm (Figure 76). In this test three smart saddles were produced according to procedure#2 without applying the weight (indicated with P, in Figure 77) and three smart saddles with applying the weight indicated by (T).

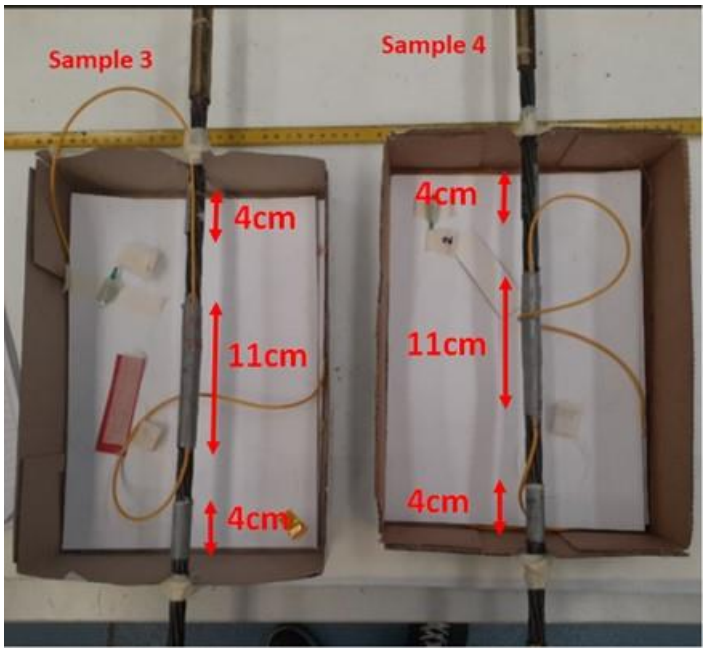

Figure 76. Strand Sample 3 and 4

According to in Test01 on sample 1, it was found that Δλ should ideally range between 2-2.5 nm (Figure 72.), but in Test01 on sample 3 top smart saddle measure unrealistic values which must be ignored from the analysis of the data (Figure 77.b). The difference between mid and bottom smart saddles is approximately 21%. The extensometer slipped during the last two cycles, affecting data reliability. The Test02 was not performed.

Similarly, in Test01 on sample 4, the pre-tensioning load (T) generally improves the performance of the FBG and smart saddle compared with those of without pre-tensioning of the fiber (P), (Figure 77.b). Differences in measurements may be attributed to uncertainties in the production procedure. In Test01 on sample 4, the extensometer recorded compression, consistent with FBG

measurements. The maximum percentage difference in Δλ relative to the top smart saddle is 4% for both smart saddles, while it increases to 25% for the mid smart saddles.

Furthermore, no significant correlation was found between the measurements obtained from the 11cm and 4cm smart saddles (Figure 77.b and d).

Overly, it can be concluded that the measurement quality was improved in smart saddles produced by procedure#2 and applying weight improved the measurement performance.

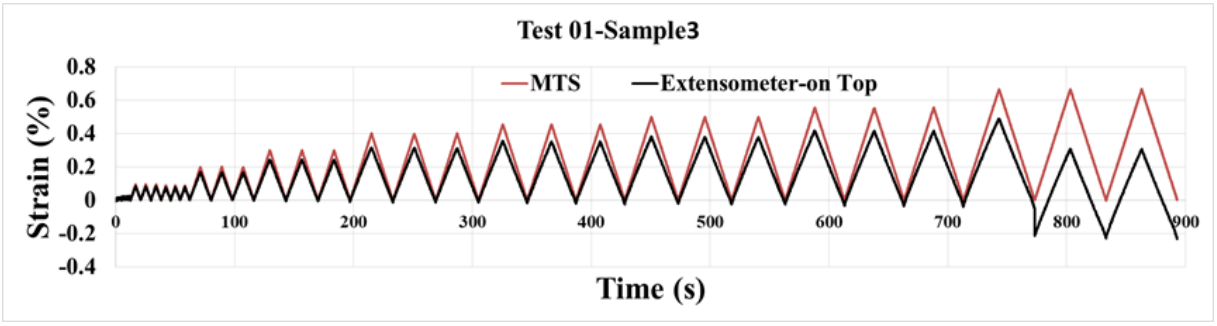

a) Extensometer and MTS machine strain results In Test01 on Sample3

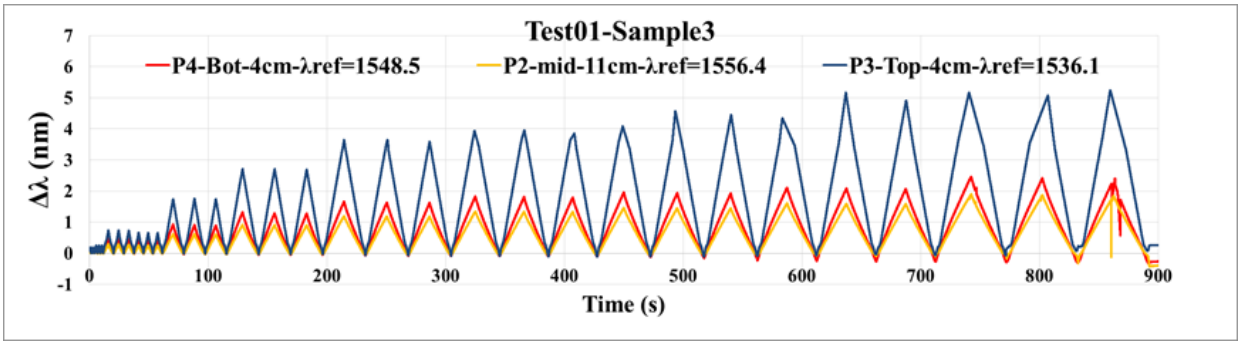

b) Wavelength variation measured by smart saddles In Test01 on Sample3

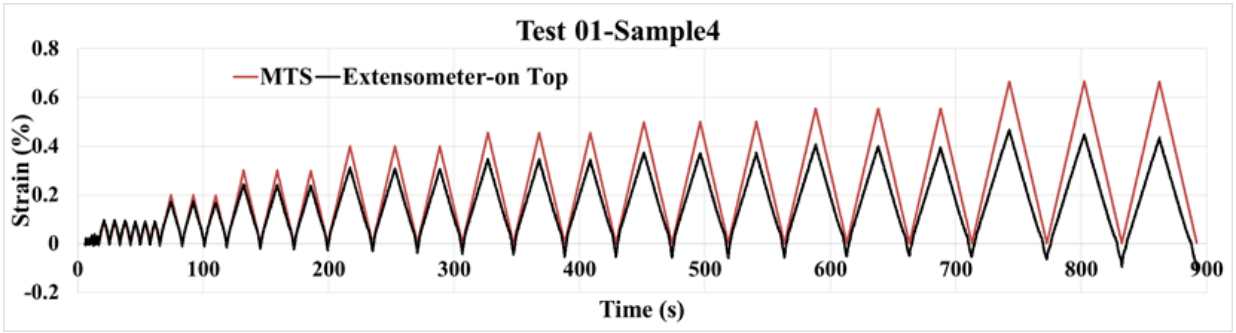

c) Extensometer and MTS machine strain results In Test01 on Sample4

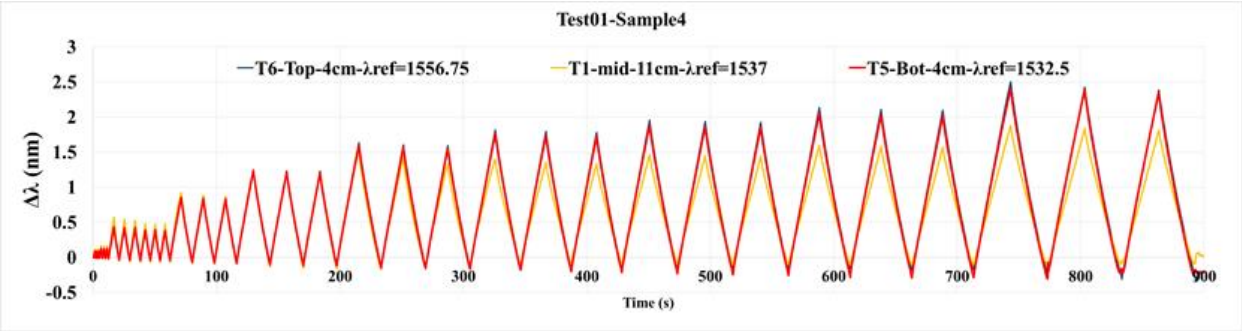

d) Wavelength variation measured by smart saddles In Test01 on Sample4

Figure 77. The tensile test results for samples 3 and 4, equipped with smart saddles produced in accordance with procedure #2 and attached to the Strands using Araldite-2011 glue

Production Procedure#3

In this procedure, efforts have been made to address some of the difficulties encountered in the previous procedure. Following a thorough assessment of the smart saddles produced using the previous approach, it was determined that the use of steel plates and the creation of a groove may not be necessary. Therefore, in this modified procedure, the steel plates are eliminated, and scotch tape is used instead to secure the paper to the table. Additionally, two extra pieces of scotch tape are strategically placed to create a gap along the paper for adding epoxy resin. These tapes are later removed before curing to clean off any excess resin. This modification significantly reduces the time required for this step and eliminates the challenges associated with using steel plates.

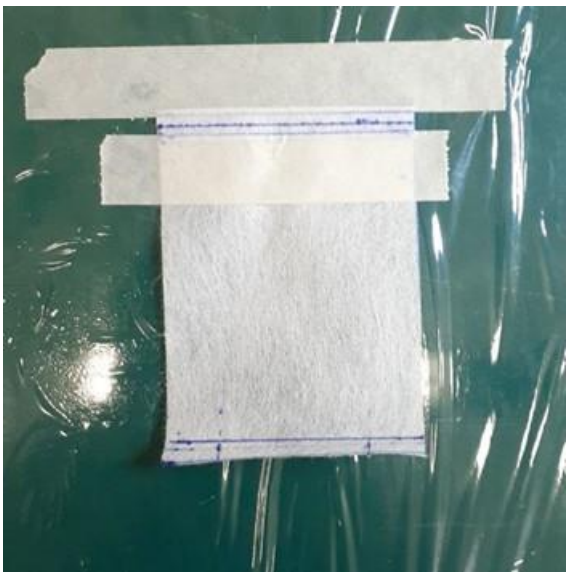

a) Fix the paper on the table

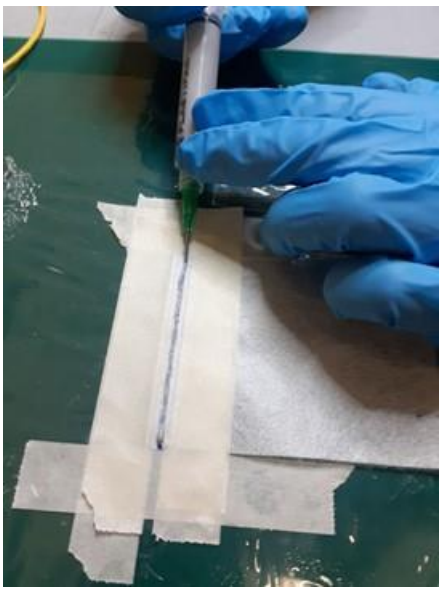

b) Add two extra scotch tapes and epoxy resin

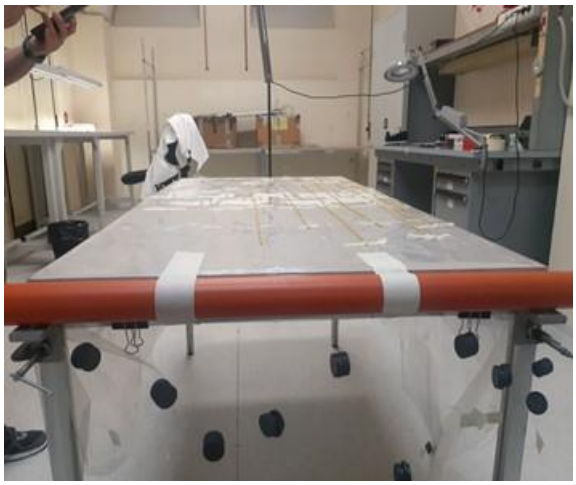

c) Applying the weight

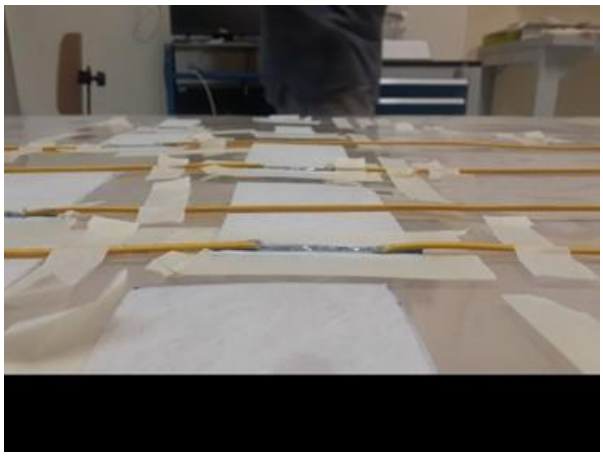

d) Remove two extra scotch tape

Figure 78. Detailed steps for preparing polyester paper before wrapping in production procedure#3

Tensile Tests on strand with smart saddles (procedure#3)

For the performance evaluation of smart saddles produced by the described procedure, a series of tensile tests has been conducted. Seven samples were prepared according to this procedure. The first three of them are strands, the next two are rebar, and the last two are a combination of rebar and strand. However, only Sikadur-330 was used for smart saddle production and as the interface glue for the last two samples. Table 4 presents the strand or rebar samples equipped with smart saddles. The samples are differentiated based on smart saddle length, smart saddle number of layers, and the type of resin or glue used as impregnating resin or interface glue for smart saddle mounting on the strand.

Table 4. Detailed description of strand or rebar samples equipped with smart saddles

Sample Number	Samples Type	Production Procedure	Impregnating Epoxy resin	Interface Glue	Smart saddles Length (cm), (Location on specimen: Top, Mid, Bot)	Smart saddle number of layers
5	65cm-7-wire Strand (D=12.5mm)	3	Sikadur-330	Araldite-2011	4, 7, 7	4
6	65cm-7-wire Strand (D=12.5mm)	3	Sikadur-330	Araldite-2011	4, 7, 7	4
7	65cm-7-wire Strand (D=12.5mm)	3	Sikadur-330	Araldite-2011	4, 7, 7	4
8	65cm- Rebar (D=20mm)	3	Sikadur-330	Araldite-2011	4, 4	4
9	65cm-Rebar (D=12mm)	3	Sikadur-330	Araldite-2011	4, 4	4
10	65cm-Rebar (D=12mm)	3	Sikadur-330	Sikadur-330	4, 4, 4	4, 2
11	65cm-7-wire Strand (D=12.5mm)	3	Sikadur-330	Sikadur-330	4, 4, 4	4, 2

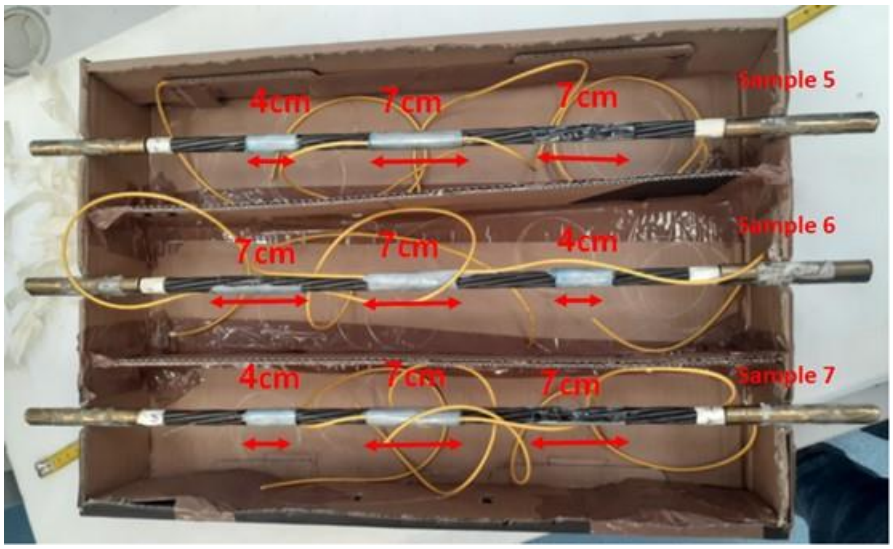

a) Sample 5 and 6, 7

b) Sample 8 and 9

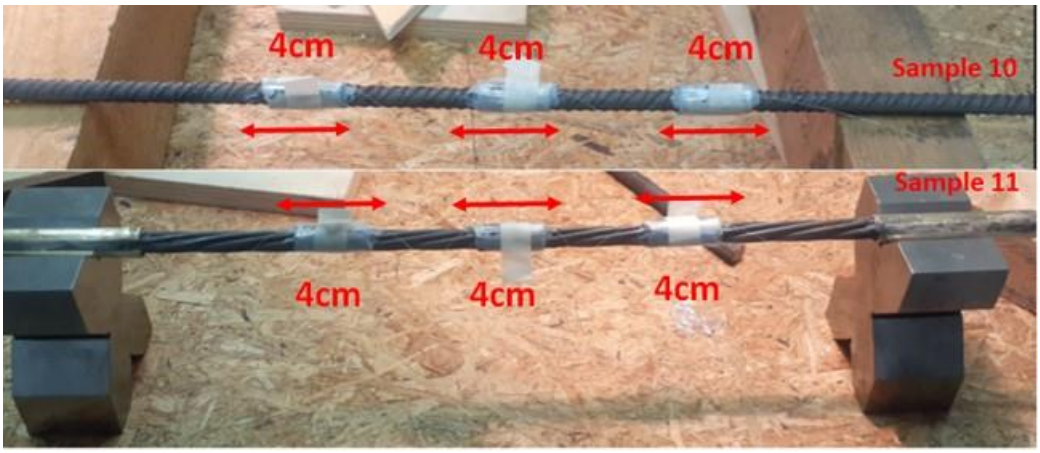

c) Sample 10 and 11

Figure 79. 11 samples equipped with smart saddle for tensile test

Samples 5, 6 and 7 were tested the diagram begins with negative values (Figure 80 b, f and j), indicating that the Fiber FBGs were under compression before the test commenced (note that the initial applied load is 0.1 kN, meaning there was no compression load on the specimen at the beginning). These negative values may be attributed to glue shrinkage. In Test01 on sample 5 (Figure 80 b), the mid and top smart saddle measurements coincide with each other, and the negative values are in agreement with the results from the extensometer. In this case, the difference between smart saddle measurements relative to the top smart saddle is 2% for the mid smart saddle and 20% for the bottom smart saddle. As it is clear, the measurement error compared with previous production procedures were generally improved. Again, no meaningful relation between smart saddle length and measurement accuracy was seen (Figure 80.d). This behavior remained constant for Test02 on sample 5.

In Test01 on sample 6 (Figure 80 d), it was noted that the middle smart saddle did not function properly. After around 300 seconds from the beginning of the test, some negative values were measured by the extensometer. Despite careful installation of the extensometer, it slid after several cycles, possibly due to the compression behavior of the strands. But smart saddles measured negative values from the beginning, the difference between smart saddle measurements relative to the top smart saddle is 28% for the bottom smart saddle which has remained constant for Test02 (Figure 80. h).

For Test01 on sample 7 (Figure 80. J), the maximum difference between smart saddle measurements relative to the top smart saddle is 13% for the bottom smart saddle and 30% for the middle smart saddle (Figure 80. j). But large value of negative values was measured by the top smart saddle indicating break or damage in this smart saddle. In Test02 for sample 7 (Figure 80. L), the difference between smart saddle measurements relative to the top smart saddle is 2% for the bottom smart saddle and 53% for the middle smart saddle (Figure 80.l).

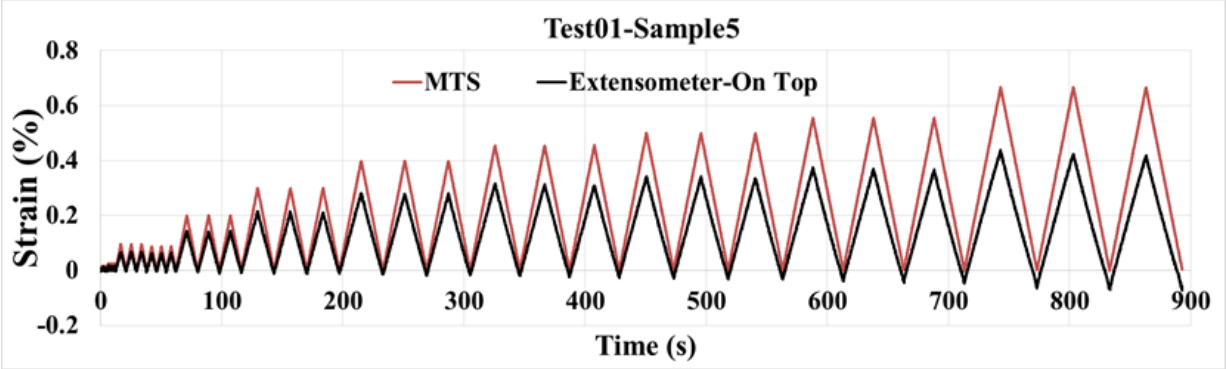

a) Extensometer and MTS machine strain results in Test01 on Sample5

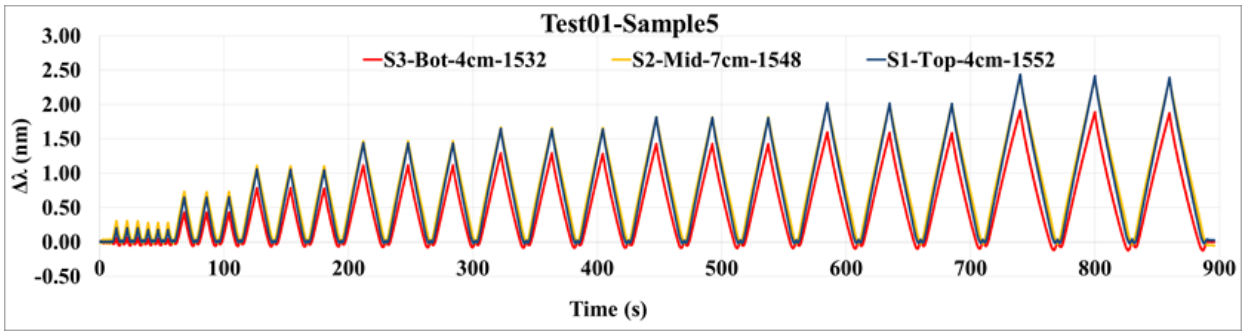

b) Wavelength variation measured by smart saddles in Test01 on Sample5

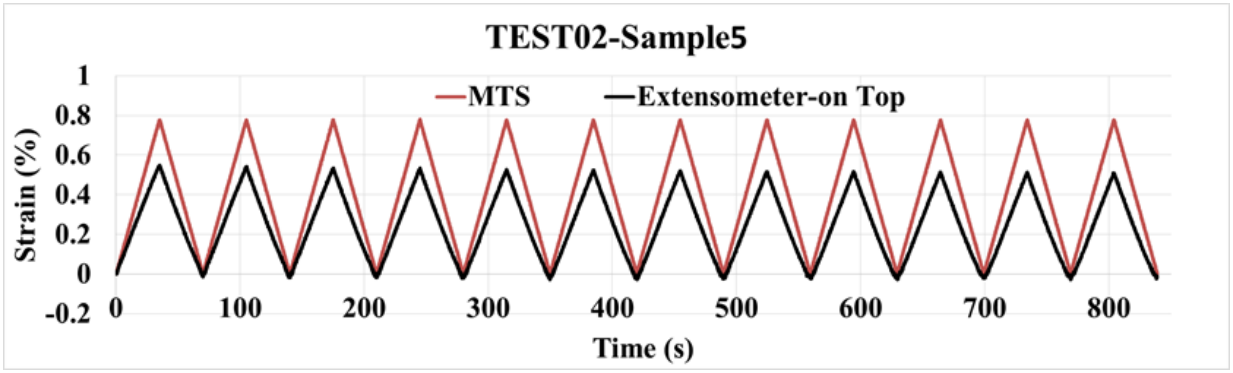

c) Extensometer and MTS machine strain results in Test02 on Sample5

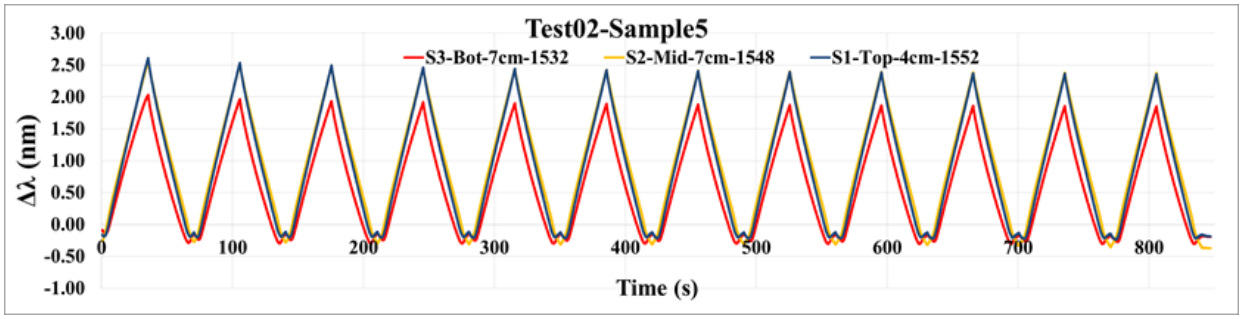

d) Wavelength variation measured by smart saddles in Test02 on Sample5

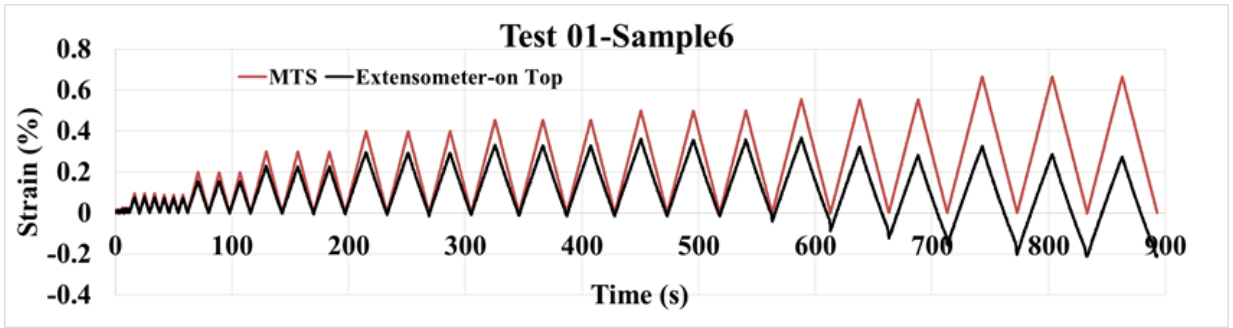

e) Extensometer and MTS machine strain results in Test01 on Sample6

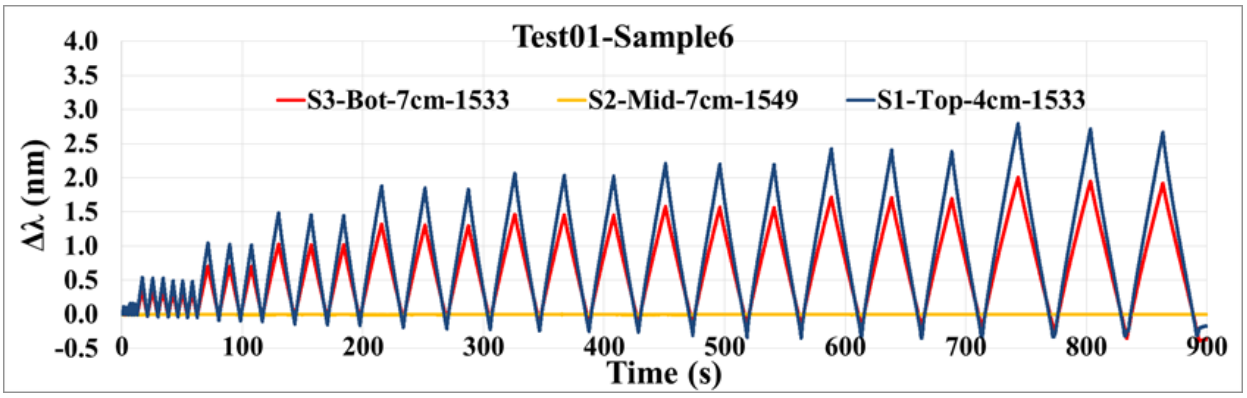

f) Wavelength variation measured by smart saddles in Test01 on Sample6

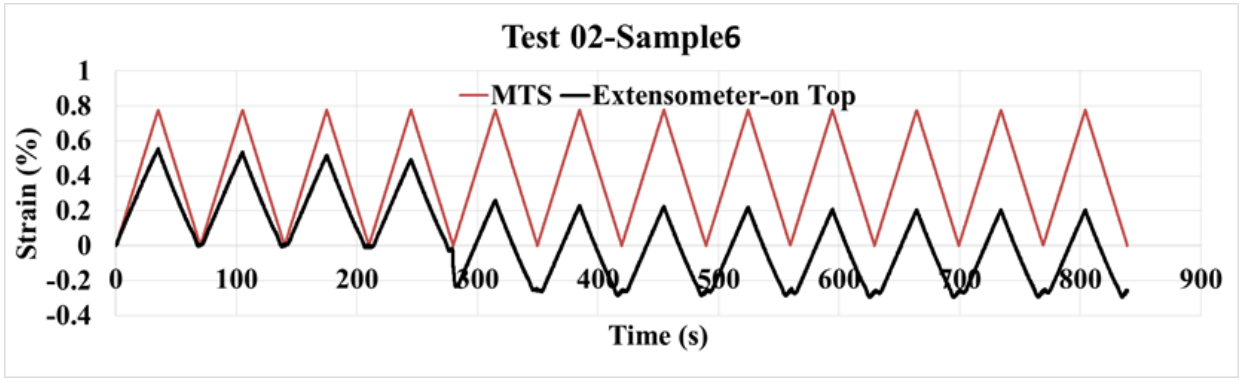

g) Extensometer and MTS machine strain results in Test02 on Sample6

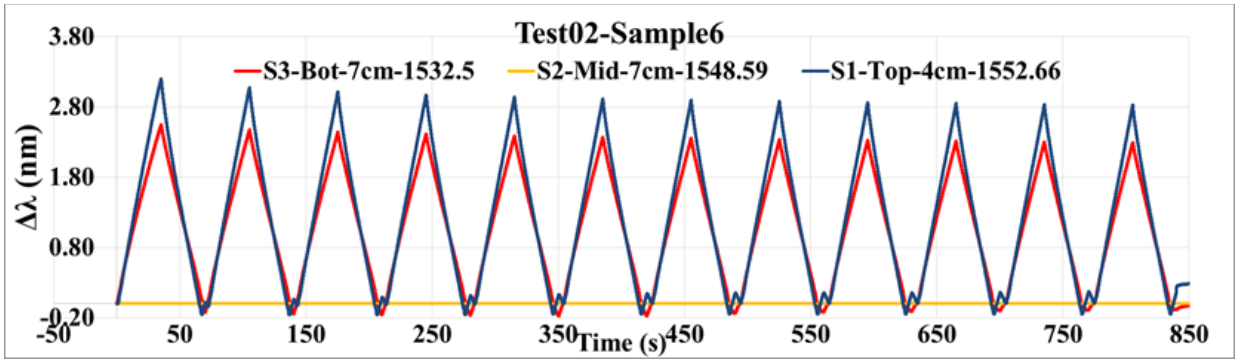

h) Wavelength variation measured by smart saddles in Test02 on Sample6

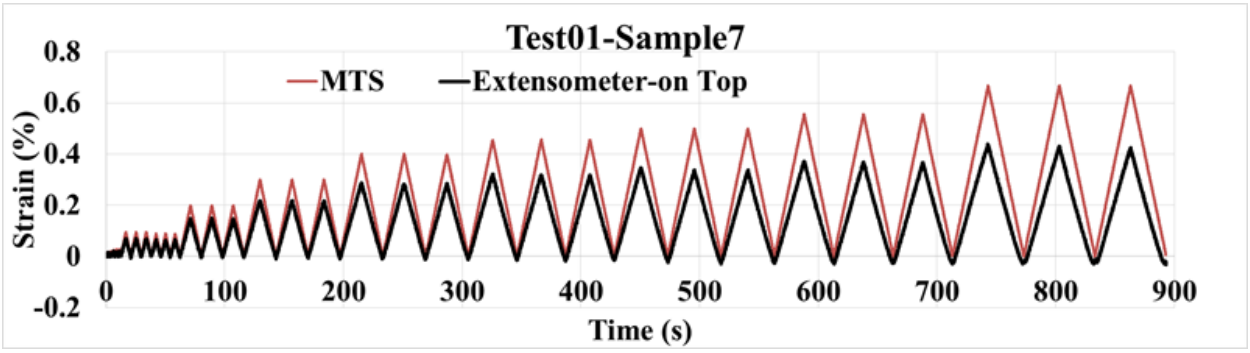

i) Extensometer and MTS machine strain results in Test01 on Sample7

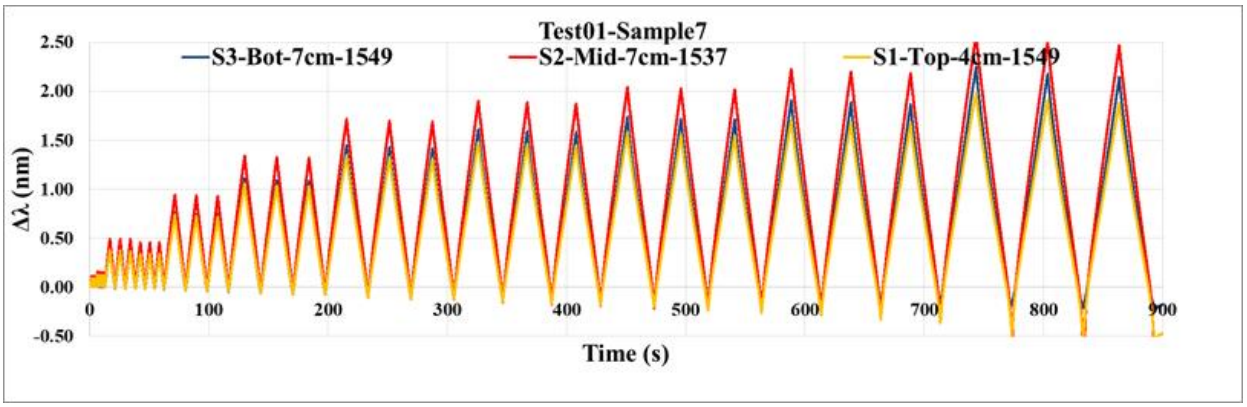

j) Wavelength variation measured by smart saddles in Test01 on Sample7

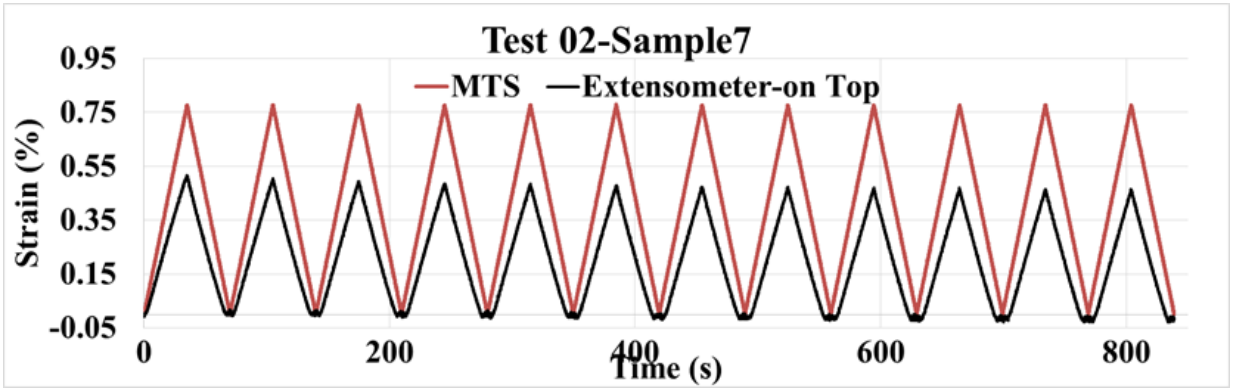

k) Extensometer and MTS machine strain results in Test02 on Sample7

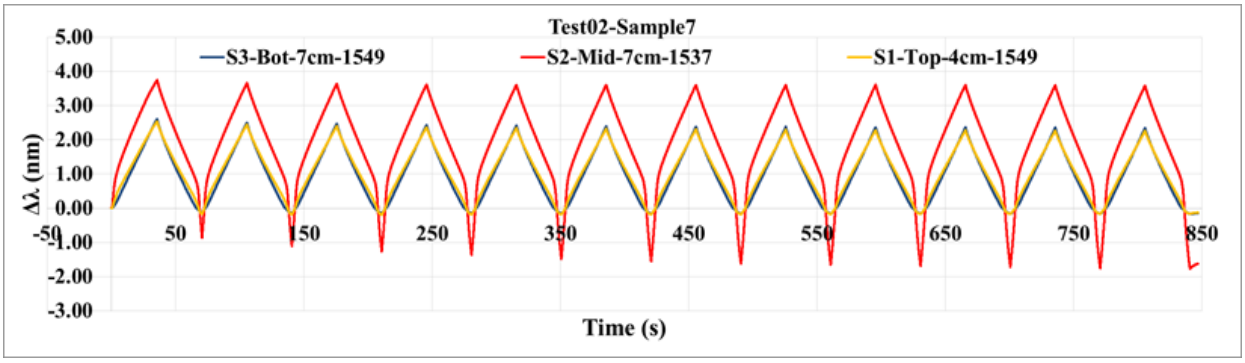

l) Wavelength variation measured by smart saddles in Test02 on Sample7

Figure 80. The tensile test results for samples 5,6, and 7, equipped with smart saddles produced in accordance with procedure #3 and attached to the Strands using Araldite-2011 glue

It is anticipated that the measurement quality will be improved for the rebar samples compared to the strand samples. This expectation arises from the fact that strands consist of seven separate wires, which, when under tension, could become turned/twisted around the center wire, adding complexity to the measurement process. To ensure that the results pertain to the performance of smart saddles produced based on production procedure #3, two rebar samples were prepared, and four smart saddles were produced according to production procedure#3 and attached to them using

araldite-2011. These rebar results are intended for comparison with those obtained from strand samples (5, 6 and7).

In Test01 on sample 8 (Figure 81.b), specifically on rebar ϕ20, the maximum error at peak loads between smart saddles is 12% (Figure 81. b & d). Additionally, negative values were measured by the smart saddles, while no compression was detected by the extensometer. In Test02 on sample 8 (Figure 81. d), the maximum error at peak loads between smart saddles is 10%. Interestingly, despite a constant load amplitude, the error increases. This suggests that damage may have occurred to the top smart saddle or its interface glue.

In Test01 on sample 9 (Figure 81.f), specifically on rebar ϕ12, the maximum error at peak loads between smart saddles is 3.5% (Figure 81. f & h). Again, negative values were measured by the Fiber Bragg Gratings (FBGs), while no negative values were recorded by the extensometer. This suggests a possible modest failure of the interface glue (Araldite-2011).

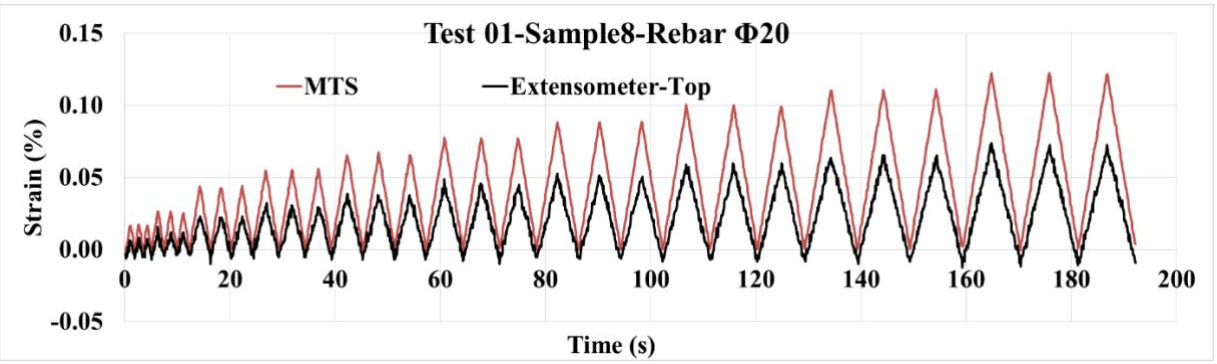

a) Extensometer and MTS machine strain results in Test01 on Sample8

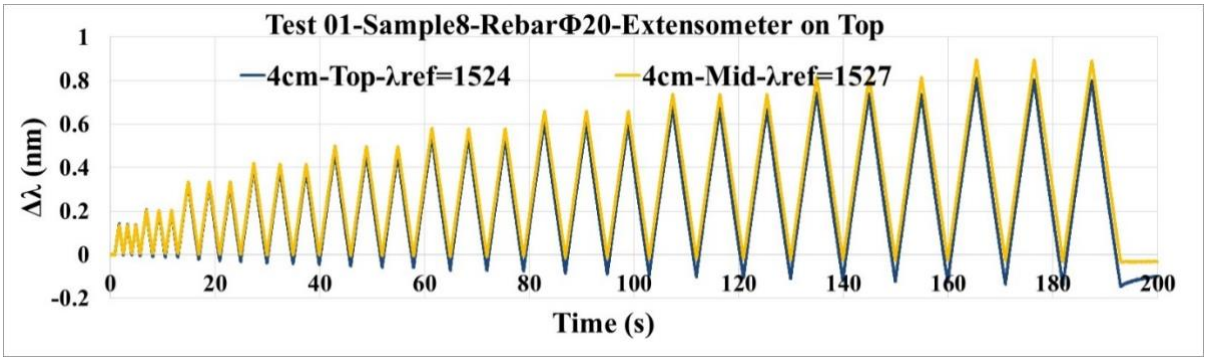

b) Wavelength variation measured by smart saddles in Test01 on Sample8

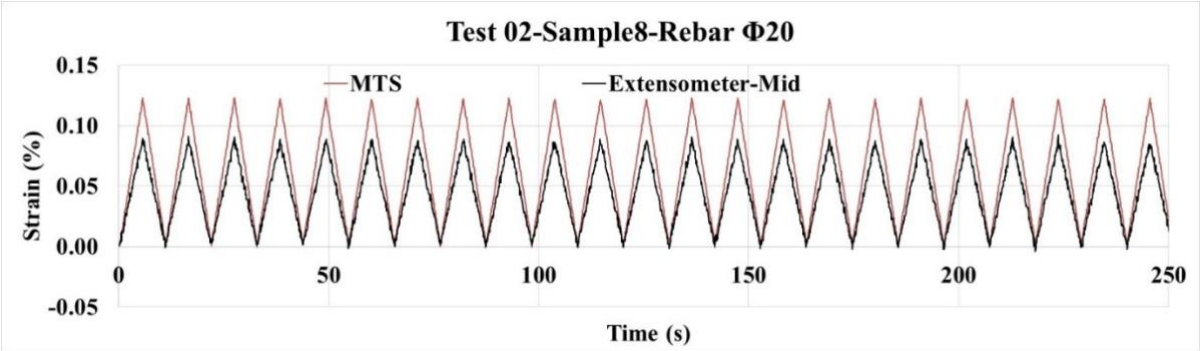

c) Extensometer and MTS machine strain results in Test02 on Sample8

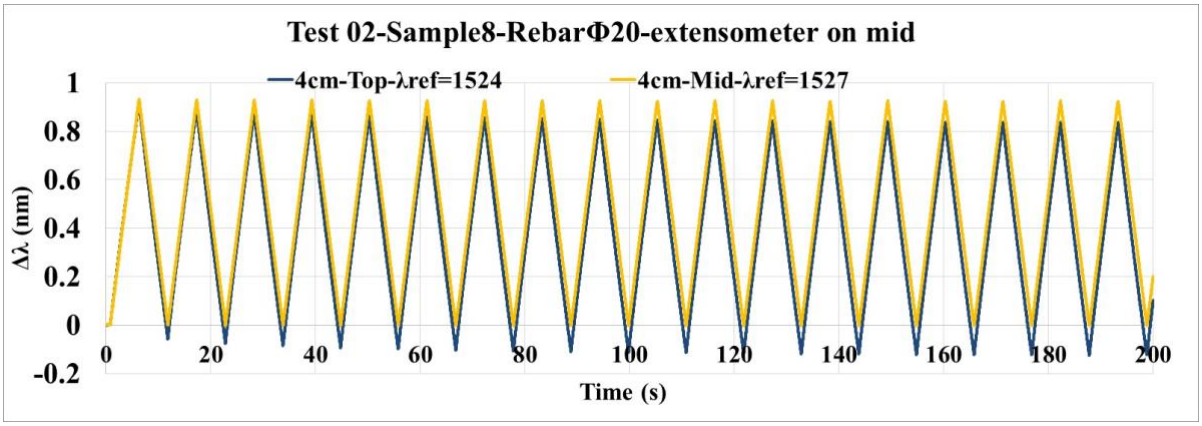

d) Wavelength variation measured by smart saddles in Test02 on Sample8

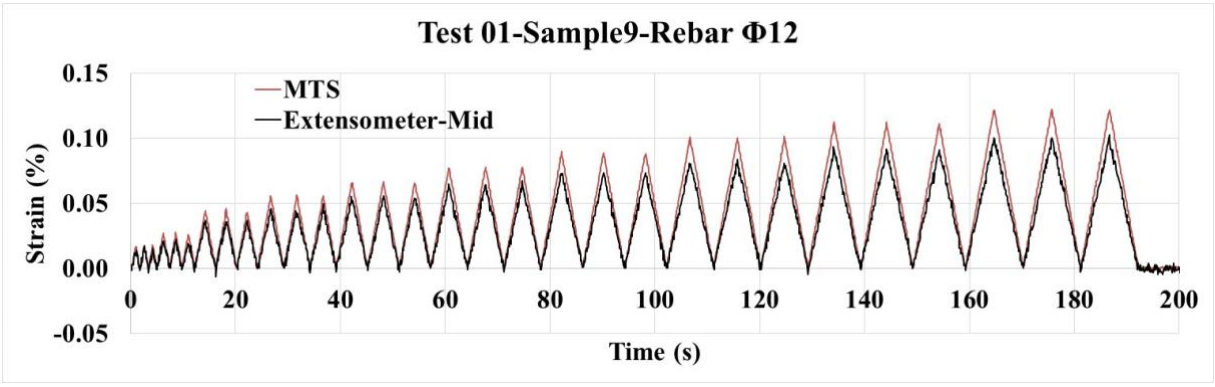

e) Extensometer and MTS machine strain results in Test01 on Sample9

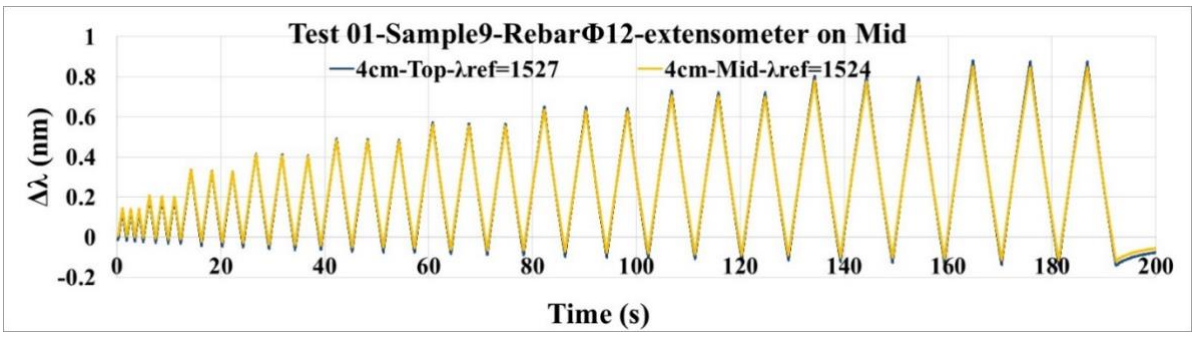

f) Wavelength variation measured by smart saddles in Test01 on Sample9

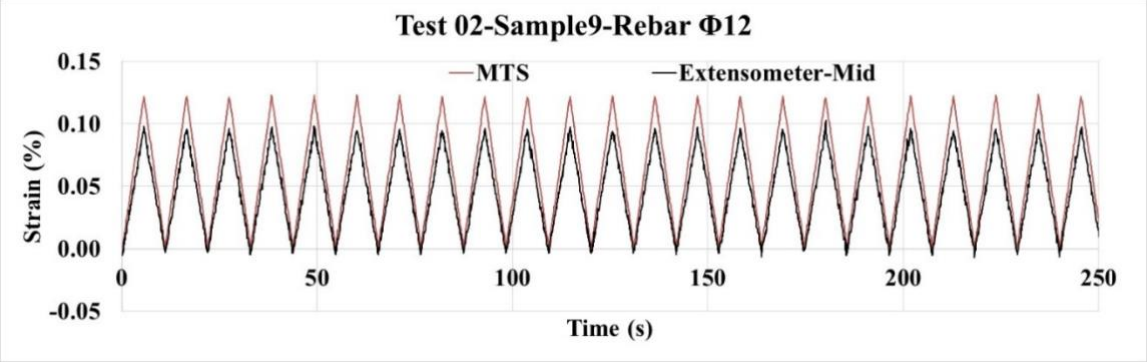

g) Extensometer and MTS machine strain results in Test02 on Sample9

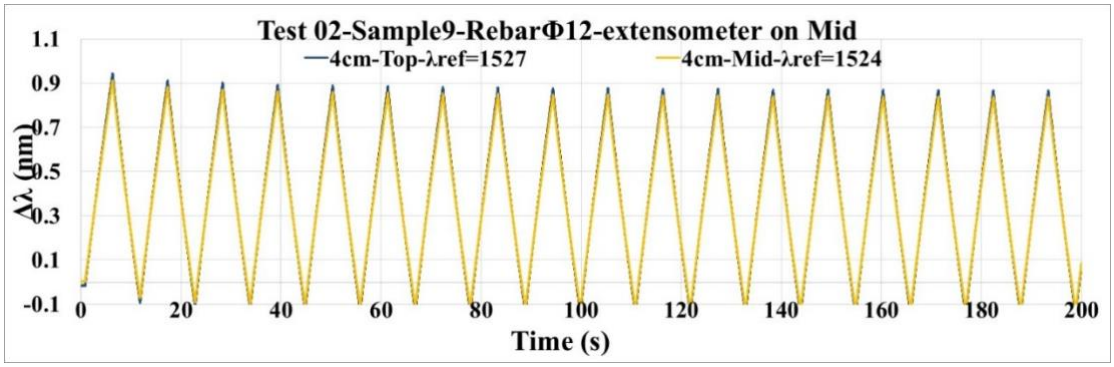

h) Wavelength variation measured by smart saddles in Test02 on Sample9

Figure 81. The tensile test results for samples 8 and 9, equipped with smart saddles produced in accordance with procedure #1 and attached to the Rebars using Araldite-2011 glue

Based on the results obtained from samples 8 and 9 (Figure 81), it can be concluded that production procedure #3 is satisfactory. However, to further enhance measurement quality, it might be beneficial to explore alternative interface glues. As a result, Sikadur-330 is utilized for both smart saddle production and as the interface glue for attaching the smart saddle to the strand. This change aims to evaluate how using Sikadur-330 affects measurement quality compared to the previous interface glue (Araldite-2011). In addition, the effect of the number of smart saddle layers on measurement performance and quality was examined by considering 2 and 4 smart saddle layers. Sample 10 is rebar ϕ12 and sample 11 is steel strand.

In Test01 on sample 10 (a rebar sample) (Figure 82.b), it was observed that production procedure #3 yielded minimal error between measurements. However, there were indications that the smart saddle experienced some negative values consistency with extensometer measurement. The position of the extensometer was systematically changed in each test, from top to bottom. Remarkably, no differences were observed between measurements, indicating consistent results regardless of the extensometer's position. Additionally, the difference between smart saddle measurements remained below 6% for strains up to 0.1%, which is half of the yielding strain of the rebar (0.2%). Notably, smart saddles with 2 layers exhibited the same measurement quality as those with 4 layers. This suggests that the number of smart saddle layers has no significant effect on the quality of measurement for the rebar (Figure 82.b).

In Test02 on sample 10 (a rebar sample) (Figure 82.d), the quality of measurements remained consistent with the previous test. Similarly, the difference between smart saddle measurements stayed below 4% for strains up to 0.1%, which is half of the yielding strain of the rebar (0.2%). Moreover, smart saddles with 2 layers exhibited the same measurement quality as those with 4 layers (Figure 82.d). It should be mentioned here that rebar's yielding strain is about 0.2%, thus the smart saddles are able to monitor strain until the rebar yielding which is beyond the service limit state criteria. It will be discussed further later.

In Test01 on sample 11 (a strand sample) (Figure 82.f), the difference between smart saddle measurements remains less than 6% for strains below 0.4%. However, upon surpassing strain levels beyond 0.4%, the difference increases, indicating a potential break in either the smart saddle or the interface glue (Sikadur-330). Notably, the error in the 2-layered smart saddle is greater than that in the 4-layered smart saddle. The performance of the smart saddle measurements has notably deteriorated after this test, suggesting that the smart saddles may be damaged, and their measurements are no longer reliable. However, it is important to note that the smart saddle measurement quality remains perfect for strains below 0.4%, and measurements within this range are considered reliable (*Figure 82*.f). The authors underline that during monitoring of element we will aspect strain below 0.2% for rebar and below 0.4% for strand.

In Test02 on sample 11 (a strand sample) (Figure 82.h), the difference between smart saddle measurements is 40% for the 2-layered smart saddle and 20% for the 4-layered smart saddle, indicating significant damage to the smart saddles from the previous test. Notably, the error has increased more in the 2-layered smart saddle, suggesting that it has experienced more damage compared to the 4-layered smart saddle. Despite this, it is important to note that the smart saddle measurement quality remains perfect for strains below 0.4%, and measurements within this range are considered reliable (*Figure 82*.h).

As a conclusion for this section, procedure #3 is recommended for smart saddle production. The tensile test results revealed that with an improved production procedure, the accuracy of FBG measurements increased, reducing the difference between measurements from 63% to only 4%. Smart saddles produced according to procedure #3 measured strain with acceptable accuracy, but the error between smart saddle measurements increased as the load amplitude increased. This indicates potential damage in the interface glue or smart saddle. Therefore, another tensile test was performed on smart saddles made only with Sikadur-330 resin for both impregnating the polyester paper and the interface glue. In this case, where only Sikadur-330 was used for both production and interface glue, the difference between smart saddle measurements was modest and constant (less than 4%) for all load amplitudes. This production procedure will then be used in the next chapter for mass smart saddle production for further testing on pre-stressed concrete beams.

It is possible to define a calibration factor between the measured saddle wavelength and the strain in the strand. This is achieved through the readings of local deformations on the strand or bar using

the extensometer placed at the location of the saddles. However, this calibration is ignored in this step to enable better comparisons between wavelength measurements in different samples.

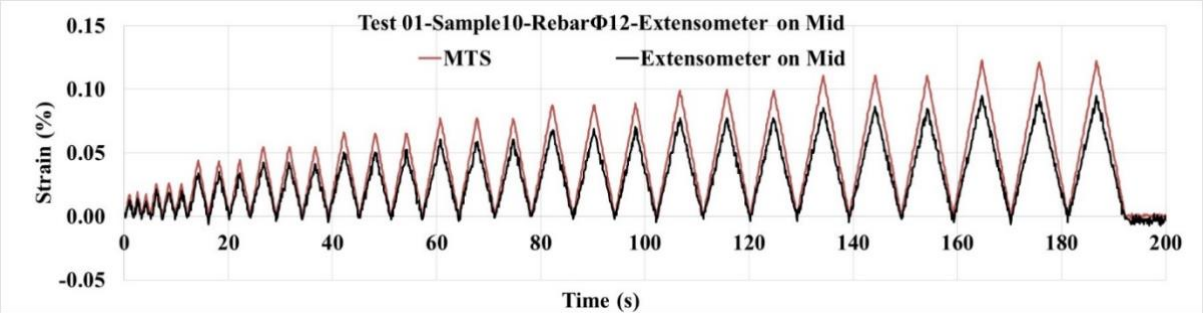

a) Extensometer and MTS machine strain results in Test01 on Sample10

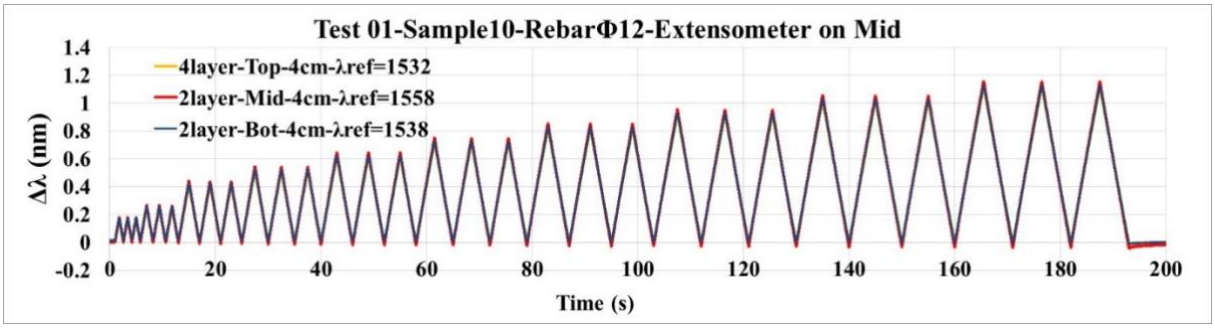

b) Wavelength variation measured by smart saddles in Test01 on Sample10

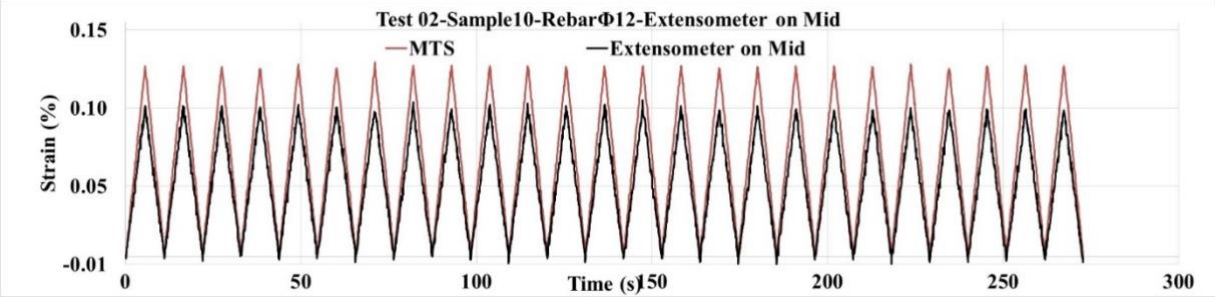

c) Extensometer and MTS machine strain results In Test02 on Sample10

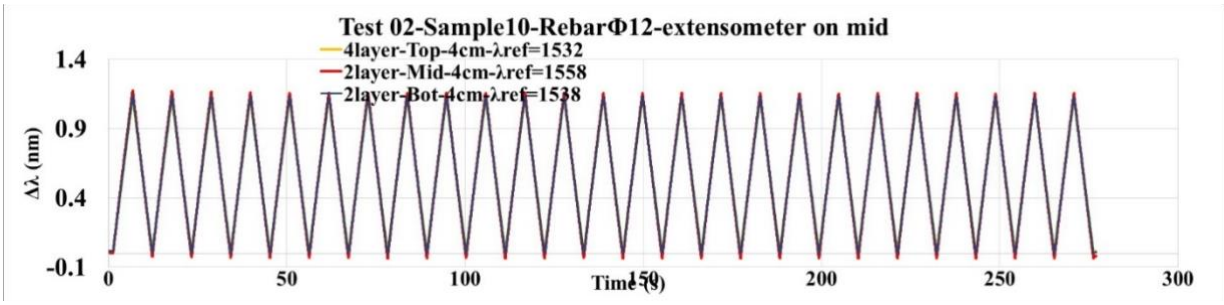

d) Wavelength variation measured by smart saddles In Test02 on Sample10

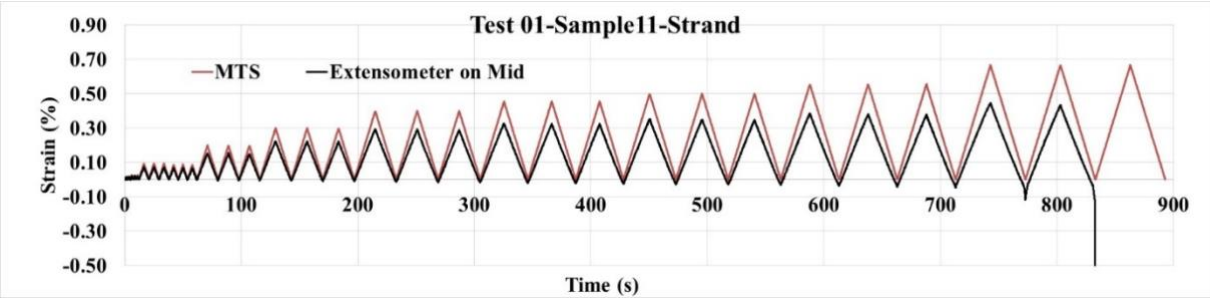

e) Extensometer and MTS machine strain results In Test01 on Sample11

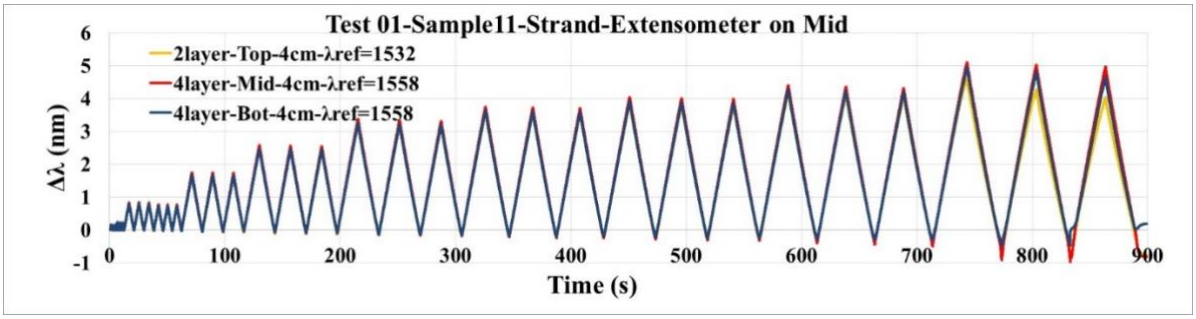

f) Wavelength variation measured by smart saddles In Test01 on Sample11

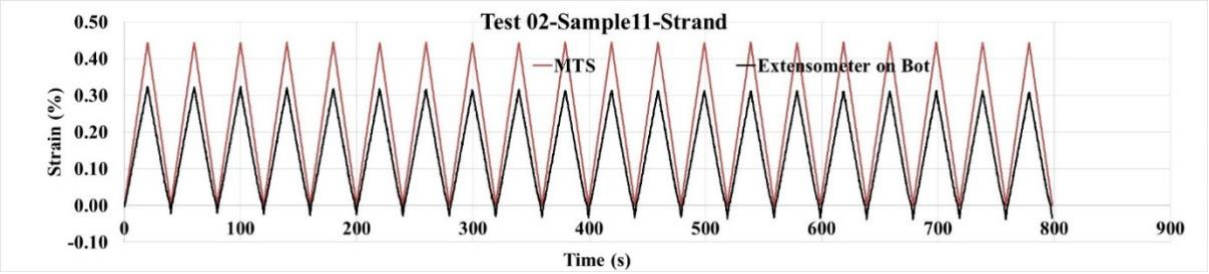

g) Extensometer and MTS machine strain results In Test02 on Sample11

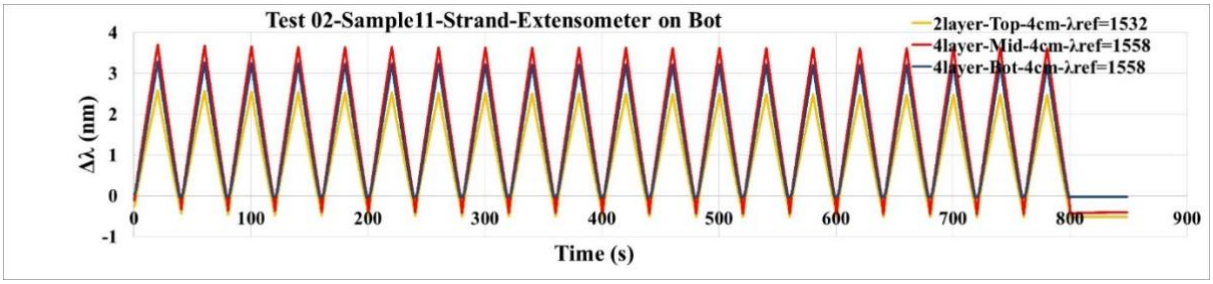

h) Wavelength variation measured by smart saddles In Test02 on Sample11

Figure 82. The tensile test results for samples 10 and 11, equipped with smart saddles produced in accordance with procedure #1 and attached to the strand and rebar using Sikadur-330 epoxy resin

Sensor arrangement for pre-stressed concrete beam bending test

As explained in the previous sections, the smart saddle is well-designed for strain measurement of the steel strands in pre-tensioned concrete elements. In this section, a study is presented to offer fundamental guidance for arranging smart saddles along the steel strand or steel reinforcing bars in one of Magnetti Building company's typical concrete beams (Figure 83) for structural health monitoring (SHM). The prefabricated beam has rectangular cross section and reinforcement detailing are provided in Figure 84. Vibration-based structural health monitoring involves assessing the structural integrity and condition of a system by analyzing its vibrational characteristics (mode shapes) (Anastasopoulos et al., 2018; Anastasopoulos et al., 2016; Farrar et al., 1994; Ndambi, Vantomme, & Harri, 2002; Unger, Teughels, & De Roeck, 2005). Therefore, deflection and mode shape identification of the system are important. For smart saddle applicability in SHM perspective, a 4-point test (Figure 84.a) on pre-stressed concrete beam has been designed and equipped with smart saddles along it to measure strain in different load levels. The test involves applying two concentrated loads on the top of the simply supported beam. This static system makes it possible to reproduce, although in an approximate way, the system of loads that the specimen is generally found to bear as a result of uniformly distributed loads. The prefabricated specimens are carefully placed into the T-frame system, resting on two supports that act as roller restraints eliminating any horizontal resistance, as per the static system considered. The beam applying the two upper loads will be punctually in contact with the specimen by means of two rollers in order to avert unintended local actions in the horizontal direction. On the support restraints, steel plate inserts will be provided between specimen and support in order to avoid local failure due to stress concentration.

a)

b)

c)

Figure 83. Magnetti Building Precast and Pre-stressed concrete products

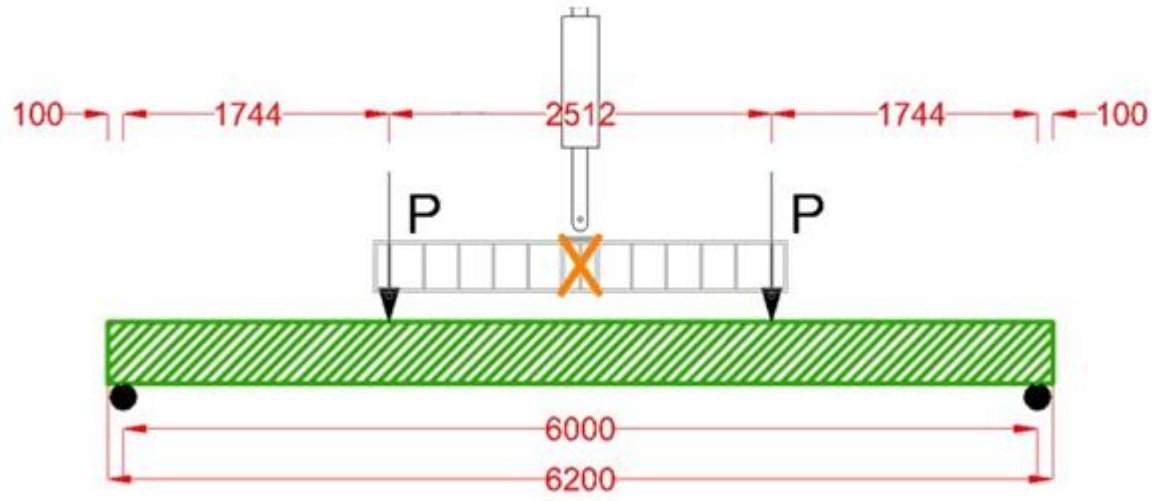

a) Beam Geometry and 4-point load test dimensioning in mm

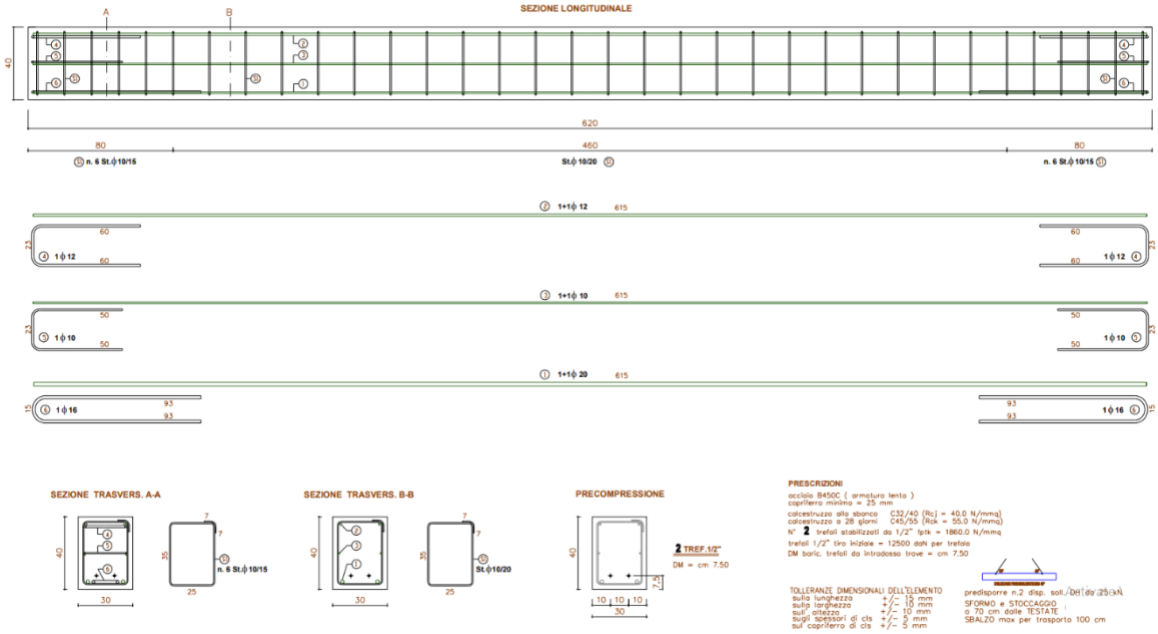

b) Beam reinforcement detailing

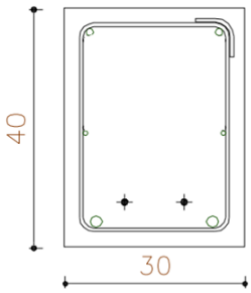

c) Beam cross section

Figure 84: Pre-stressed concrete beam detailing

For brevity, the next section focuses on calculating the deflection of the beam using smart saddle data. To achieve this, a pre-tensioned concrete beam is modeled in OpenseesPy software under a 4-point load test (Figure 84.a). The main objective is to simulate the inelastic behavior of the beam in different damage stages (concrete cracking, rebar and steel strand yielding and ultimate strength of concrete) and calculate the deformation of the beam using smart saddle data. An important consideration is the number of smart saddles required to reconstruct the beam deformation with acceptable accuracy. The reinforcement detailing of the beam is presented in Figure 84.b.

Numerical analysis in OpenseesPy software

The beam is modeled as a frame element within OpenseesPy (**Error! Reference source not found.**). Initially, the beam is subjected to a pre-tensioning stress of 1250 MPa. However, considering all losses due to creep, shrinkage, and elastic shortening of the concrete beam, the effective pre-tensioning stress reduces to 1107 MPa. This pre-stressing effect is accounted for on the beam as both moment and axial external loads.

The steel rebars are class of B450C and concrete class is C45/55 and steel strand is low relaxation Grade270. The mechanical properties of the steel and concrete materials are presented in Table 5 and Table 6.

Table 5. Mechanical Properties of steel materials

Item	Material	Module of Elasticity (GPa)	Yield stress (MPa) (fyk)	Ultimate Strength (MPa) (fuk)
1	Steel rebar	200	450	550
2	Steel strand	200	1674	1860

Table 6. Mechanical Properties of concrete

Item	Material	Module of Elasticity (GPa)	Characteristics compressive strength fck (MPa)	Characteristics ultimate strength fuk (MPa)	Strain at maximum strength (mm/mm)	Strain at ultimate strength (mm/mm)
1	Concrete C45/55	36.3	45	35	0.0024	0.0035

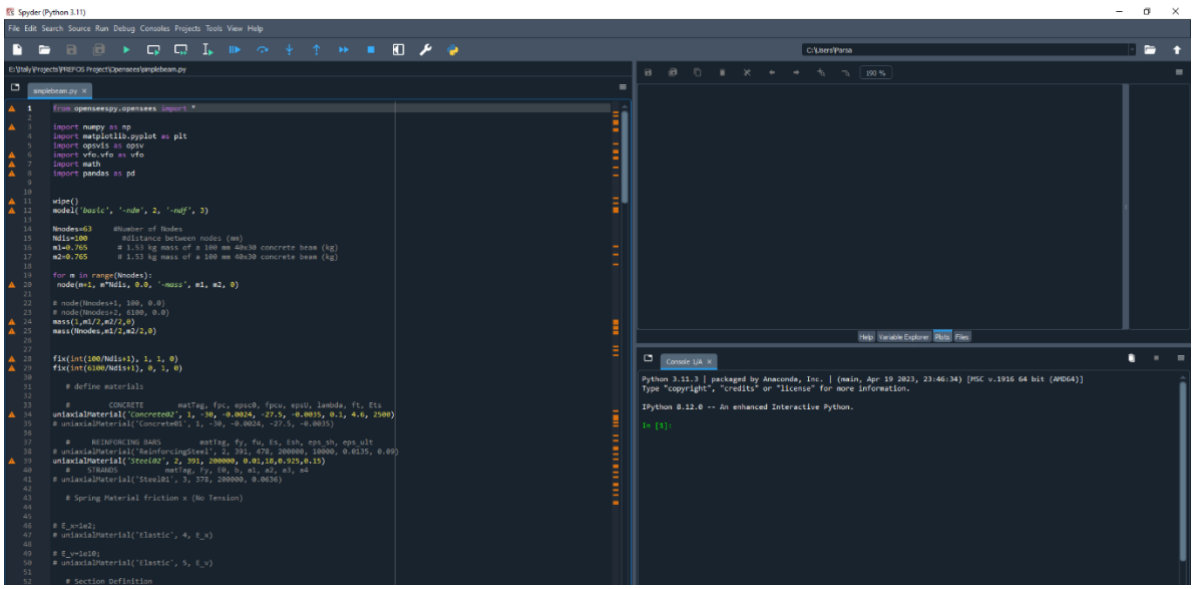

a) Python code for concrete beam modeling in OpenseesPy

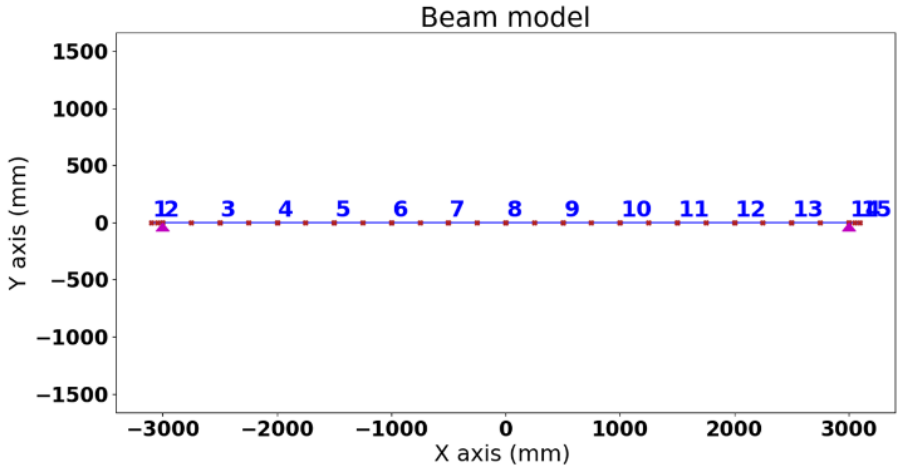

b) Beam model in OpeneseesPy

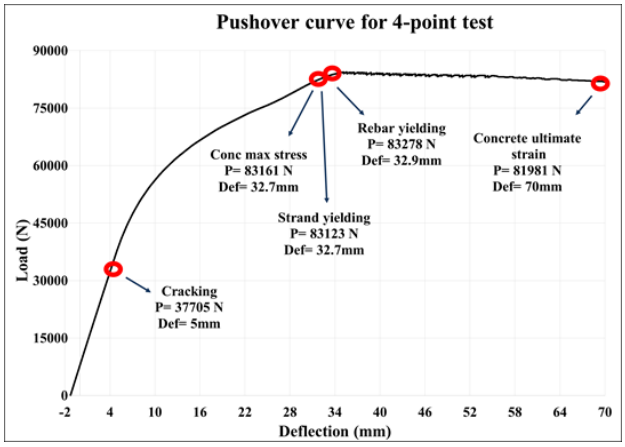

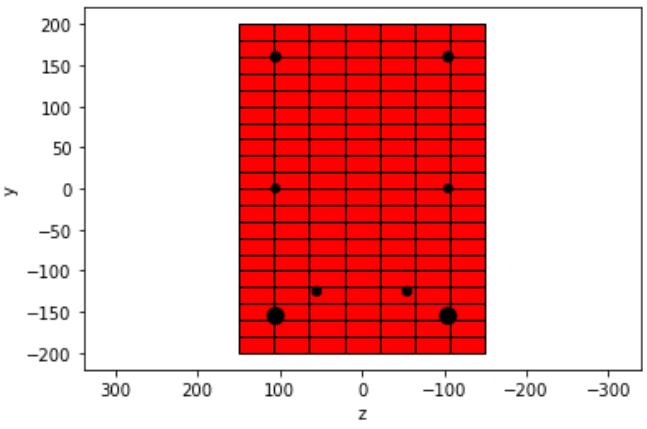

c) P load-Displacement curve d) Cross section of the beam in OpenseesPy

Figure 85. Pre-stressed concrete beam modelling in OpenseesPy and model response

The beam is loaded until reaching ultimate strength of concrete, and a load-displacement diagram is illustrated in **Error! Reference source not found.**.c. The yielding of the rebar and steel strands occurred relatively at the same load level. **Error! Reference source not found.**.c.

It should be mentioned here that the service limit state is defined based on the tensile stress limit, crack width limit, and deflection limit under service loads. The tensile stress in concrete is limited to the cracking stress, typically the mean tensile strength of the concrete for normal concrete. This limit is stricter for pre-stressed concrete, where no tensile stress is permitted in the concrete under service loads (Standard, 2004). Therefore, in the best situation, it can be concluded that the service limit state is equivalent to the cracking stage.

At each load level, corresponding to concrete cracking and rebar yielding, the static deformation and dynamic characteristics of the beam are extracted. To estimate the deflection and mode shape of the beam at each load stage, the curvature of the beam is determined using strain data at specific points along its length, referred to as 'integration points' (Figure 86). The strain data at each integration point can be measured by the smart saddle in real experiment or obtained from the numerical model in the top and bottom points on the cross-section of the beam. For example, the top point may coincide with the location of the top rebar, while the bottom point corresponds to the strand location. Curvature is then calculated using strain data from these points, based on Equation 1, where 'h' represents the distance between the top and bottom rebar or strands. Subsequently, the deflection of the beam can be computed using Equation 2.

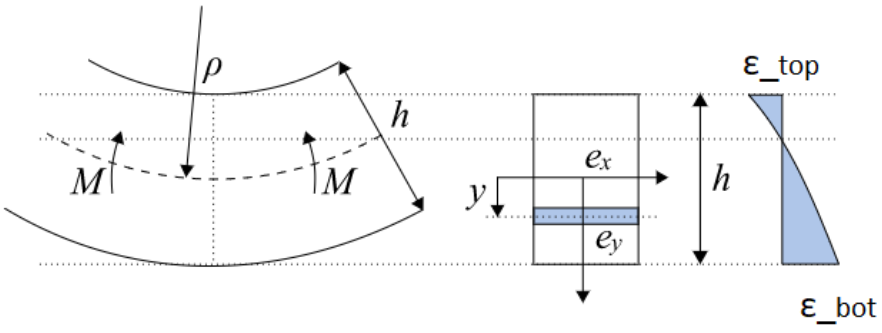

Figure 86. Strain distribution in beam section

$$Curvature = \varphi = \frac{\varepsilon_{top}+\varepsilon_{bot}}{h} \quad (1)$$

$$d(x) = \theta_A.x - \Delta = \theta_A.x - \int_A^B (x-z)\varphi(z)dz \quad (2)$$

$$\theta_A = \frac{1}{L}\int_0^L (L-z)\varphi(z)dz \quad (3)$$

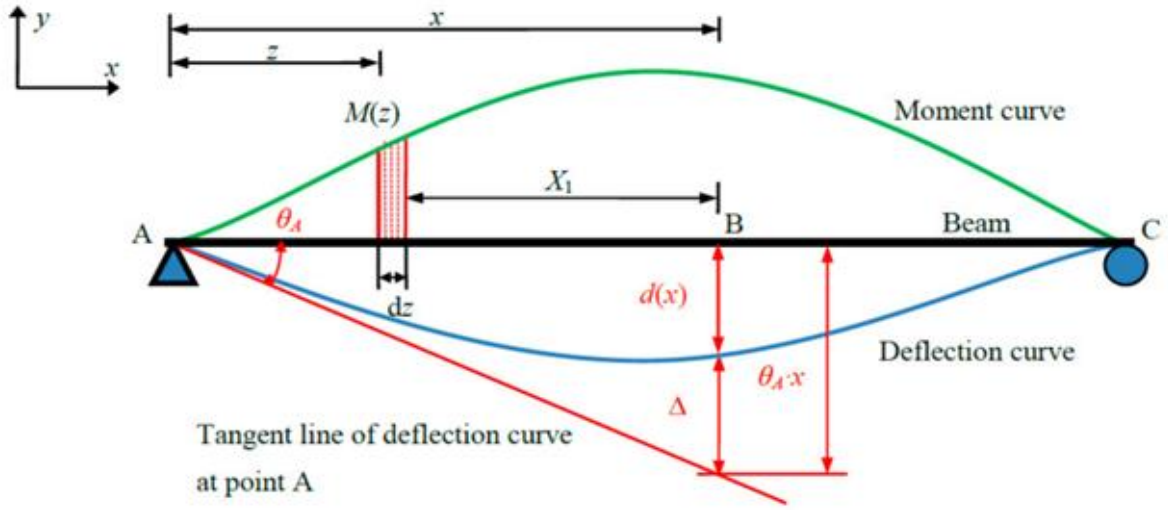

Figure 87. Beam deformation calculation method (Hong, Qin, Lv, & Fang, 2018)

The subsequent section presents the results of deflection and mode shape estimation, focusing on the variation in distance between integration points (smart saddles spacing) for different load stages or damage state of the beam (Figure 92). Obviously, by increasing the number of integration points (decreasing the distance between integration points), the accuracy of deflection or mode shape estimation increases. The distance of 5 cm between integration points is considered the reference for error calculation. The error related to the distance is summarized again in Figure 93. An important observation is that when the integration points or smart saddles are positioned at points where the curvature changes, the resulting reconstructed deflection or deformation achieves sufficient accuracy (**Error! Reference source not found.**, **Error! Reference source not found.**, **Error! Reference source not found.** and **Error! Reference source not found.** e, f and d). Hence, it is crucial to install smart saddles at strategic locations along the beam, where significant changes in curvature are anticipated. These locations typically include support points, concentrated point loads, and potential area for plasticization.

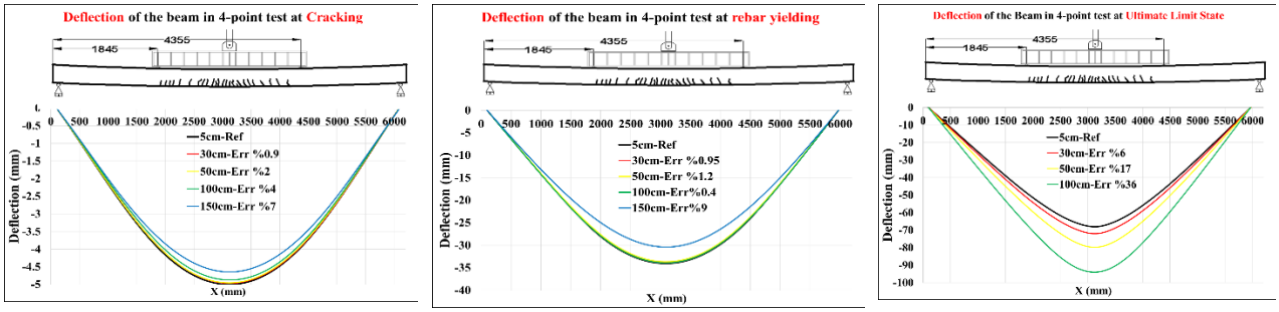

a) Deflection at cracking

b) Deflection at rebar yielding

c) Deflection at ultimate strength

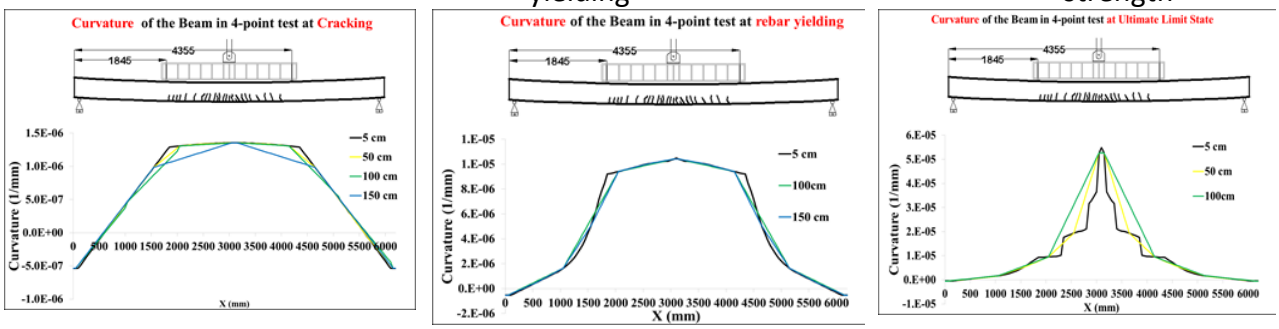

d) Curvature at cracking stage

e) Curvature at rebar yielding

f) Curvature at ultimate strength

Figure 88. Deflection and corresponding curvature diagram of the beam for three load stages

Reconstruction of the three first mode is demonstrated and illustrated in **Error! Reference source not found.**-**Error! Reference source not found.** for different integration points distance (30, 50,100 and 150cm). The results are provided for different load levels.

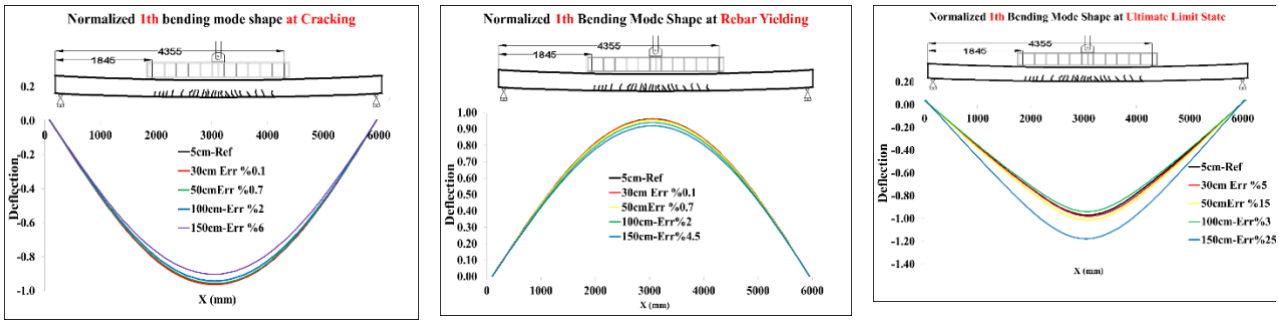

a) Deflection at cracking

b) Deflection at rebar yielding

c) Deflection at ultimate strength

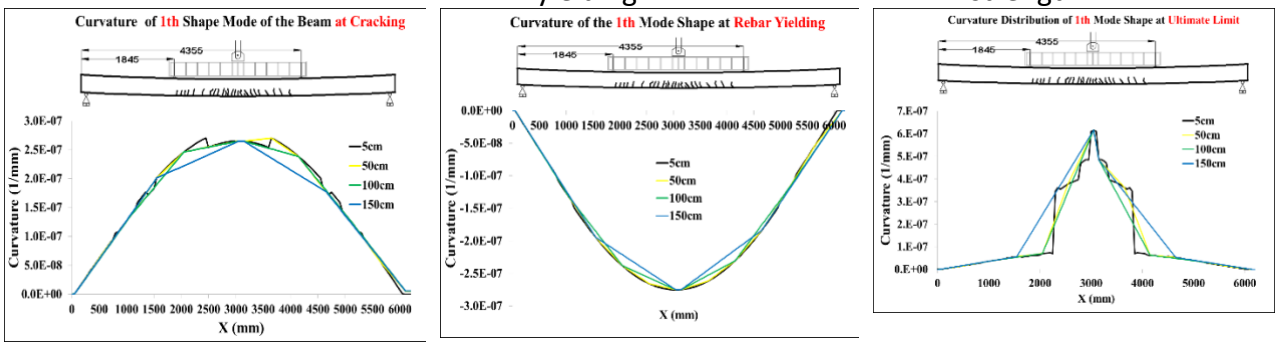

d) Curvature at cracking stage

e) Curvature at rebar yielding

f) Curvature at ultimate strength

Figure 89. First mode shape and corresponding curvature diagram of the beam for three load stages

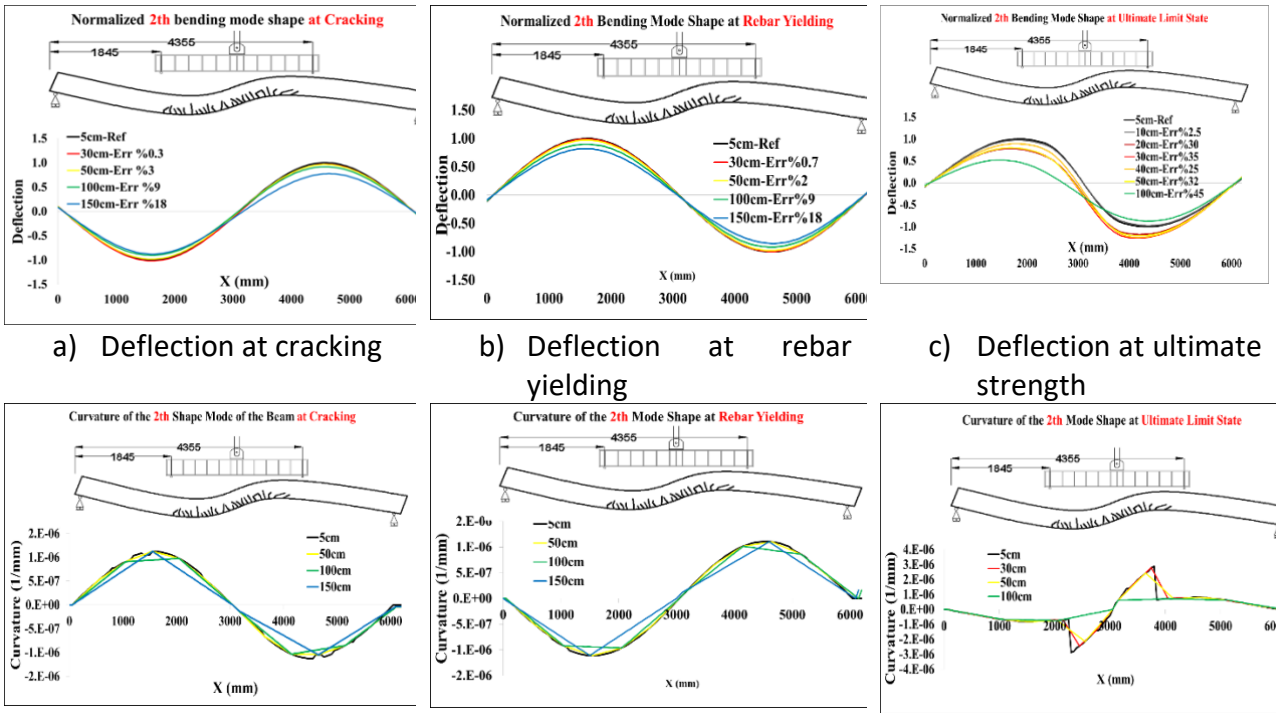

a) Deflection at cracking b) Deflection at rebar yielding c) Deflection at ultimate strength

d) Curvature at cracking stage e) Curvature at rebar yielding f) Curvature at ultimate strength

Figure 90. Second mode shape and corresponding curvature diagram of the beam for three load stages

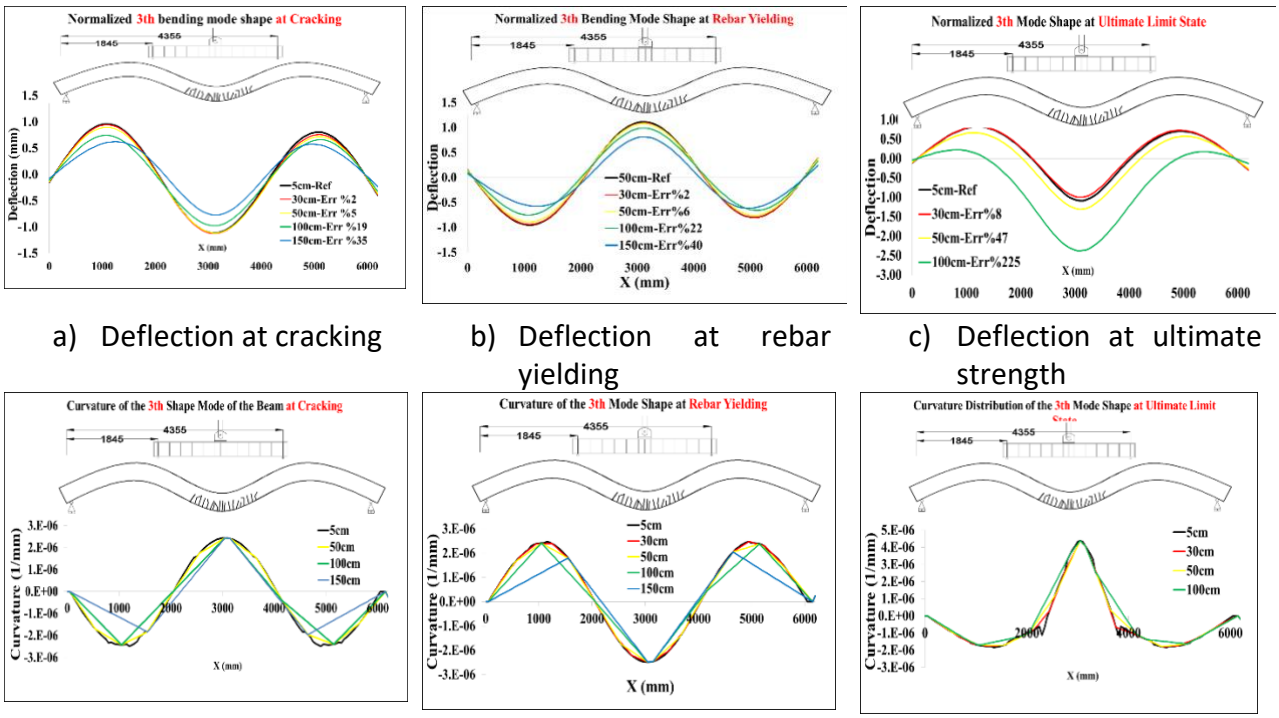

a) Deflection at cracking b) Deflection at rebar yielding c) Deflection at ultimate strength

d) Curvature at cracking stage e) Curvature at rebar yielding f) Curvature at ultimate strength

Figure 91. Third mode shape and corresponding curvature diagram of the beam for three load stages

The error percentages for deflection reconstruction using curvature at integration points relative to the reference are summarized in Figure 92. For a 50cm distance between smart saddles or integration points, the errors are %2, %1.2, and %16 for cracking, yielding, and ultimate states, respectively. For the first mode shape, the errors are %0.7, %0.7, and %5, and for the second mode shape, they are %2.7, %2.1, and %32. In the third mode shape, the errors are %5.4, %6.1, and %47. These results suggest that a 50cm distance between smart saddles is sufficient for reconstructing deflection and mode shapes with acceptable accuracy for beam dynamic identification in service limit state (cracking stage) which is the aim of this study. The smart saddles are also able to monitor strain beyond service limit state until rebar yielding (rebars' yielding strain =%0.22).

The curvature of the real beam is obtained using smart saddle strain data at top rebar and bottom rebar (Blue and Red smart saddles in Figure 93). For increasing the safety of measurement, two groups of smart saddles are considered for the strain monitoring of top and bottom bars and the distance between them is considered 100cm which together provide 50cm distance. Smart saddles with the same distance are considered for strain measurement of the steel strand (Green smart saddles in Figure 93). A group of smart saddles are also considered for the stirrup strain measurement with the same space. The distance between smart saddles is considered as the 50cm.

As the beam is symmetric for both load and geometry, the instrumentation is only considered for the half of the beam. This feature allows for the consideration of two distinct configurations for smart saddles for a single beam, resulting in cost savings for the project. The first one aligns with research goals where additional data is collected for improved data post-processing, while the second one is relevant to industry projects. In the first arrangement which is considered for the left side of the beam (Figure 93), an effort was made to ensure that additional smart saddles were available for measuring strain in stirrups, strands, and rebar. This is logical for research projects where chain rupture or unintentional loss of acquisition systems is a possibility. In the second half of the beam, another arrangement could be considered for the smart saddles. The second arrangement considers smart saddles located at specific points in which curvature changes significantly under static load or in mode shapes (support, point load location, ½, ¼ and 1/8 span) (**Error! Reference source not found.**, **Error! Reference source not found.**, **Error! Reference source not found.** and **Error! Reference source not found.** d, e and f). The second arrangement aims to reduce the number of smart saddles for industrial applications where productivity and instrumentation cost are critical. The goal of the suggested smart saddle configuration is to optimize measurement data for each component, including stirrups, strands, and longitudinal rebars. For industrial applications, the number of smart saddles can be tailored to the particular component of interest (stirrup, rebar, or strand) or the necessary accuracy. For the purpose of calculating curvature, deflection, and mode shape, the authors feel that one chain of smart saddles on the top rebar and one chain on the bottom rebar (or strand) is adequate.

Deflection Error (%) in the center of the beam related to FBG distance				
	Distance between FBG sensors			
	30 cm	50 cm	100 cm	150 cm
1. Cracking	0,9%	2,0%	4,0%	7,0%
2. Yielding	0,4%	1,2%	0,4%	9,0%
3. Ultimate	5,6%	16,0%	36,0%	-

a)

1th mode Error (%) in the center of the beam related to FBG distance				
	Distance between FBG sensors			
	30 cm	50 cm	100 cm	150 cm
1. Cracking	0,1%	0,7%	2,0%	6,2%
2. Yielding	0,1%	0,7%	2,0%	4,5%
3. Ultimate	2,5%	5,0%	3,0%	25,0%

b)

2th mode Error (%) in the center of the beam related to FBG distance				
	Distance between FBG sensors			
	30 cm	50 cm	100 cm	150 cm
1. Cracking	0,3%	2,7%	8,9%	18,0%
2. Yielding	0,7%	2,1%	8,9%	18,0%
3. Ultimate	35,0%	32,0%	45,0%	60,0%

c)

3th mode Error (%) in the center of the beam related to FBG distance				
	Distance between FBG sensors			
	30 cm	50 cm	100 cm	150 cm
1. Cracking	1,9%	5,4%	19,2%	35,0%
2. Yielding	1,9%	6,1%	22,0%	40,0%
3. Ultimate	8,0%	47,0%	225,0%	-

d)

Figure 92. Deformation (deflection and mode shapes) error relative to reference for different smart saddle spacing along the beam and for different beam state

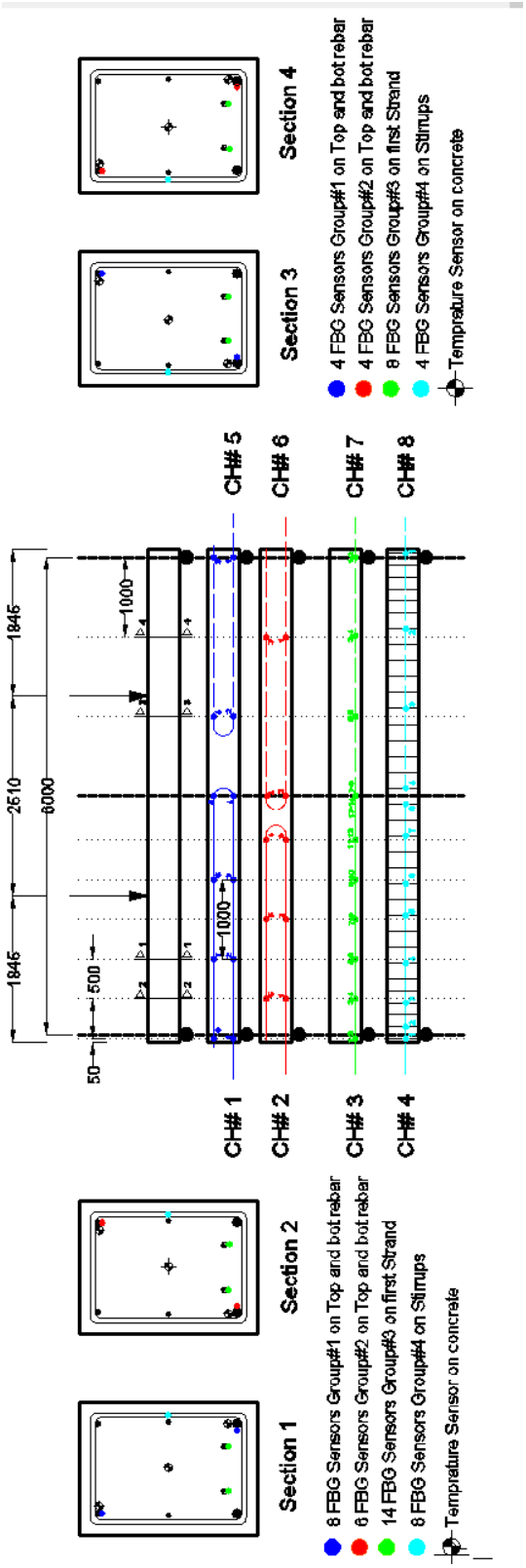

Figure 93. Possible Smart saddle arrangements along the beam on rebar, strand and stirrups for strain measurement

Experimental test protocol

For static and dynamic tests on the beam specimen, a protocol is developed here. To ensure safe execution, the test protocol for each precast element specimen consists of various cyclic tests carried out in controlled displacement at a moderate velocity of 0.01 mm/s.

Understanding the cyclic response is crucial to determining its energy dissipation and strain-rate sensitivity, as well as the effects of loading and unloading on the specimens. Beginning from the specimen rest position, each cycle aims to achieve the maximum deflection target before unloading to the rest position.

Initially, one or two cycles of cyclic testing are conducted with specimen behavior entirely recoverable, ranging from zero to a maximum displacement in the elastic region (far below the cracking deflection). These tests are repeatable numerous times and enable the operation of the fiber sensors positioned within the element as well as the test apparatus (acquisition systems configuration, proper wire connections, operational instruments, etc.) and test apparatus calibration to be verified.

To confirm measurement repeatability and system stability, cycle tests with increasing maximum displacement—much below the cracking deflection—against the entire elastic range are next conducted. The test procedure, which is frequently used to assess the stability of the specimen's reaction (stiffness and strength), consists of two or three cycles for each displacement amplitude.

Finally, cyclic tests were conducted once more with an increasing displacement amplitude to explore the serviceability limit state and induce damage to the specimens until the application of the cracking moment at sections. This test is aimed at validating the sensor capability to monitor beam behavior under service limit state conditions.

The response of the tested element is reconstructed after post-processing, starting from the data obtained from fiber sensors that measure strain on rebars and strands, in terms of section curvatures and beam deflections. These results are compared with numerical predictions and readings obtained from external measurement systems such as potentiometers or digital image correlation (DIC) systems. Additionally, the tests may include measurements of temperature variation along the specimens. Dynamic tests are incorporated into the test protocol to capture the modal shape and other natural properties of the specimen, such as period and damping.

Smart saddles attachment protocol

The fiber-optic sensor can read fiber strain up to 1%. However, the smart saddle presented here after its optimization can read with guaranteed accuracy and repeatability strand deformations up to 0.4%.

The maximum tensile strain on the strand after application of initial pre-tensioning load is estimated by calculation to be about 0.6% while the maximum strain capacity of the smart saddles is 0.4%. Therefore, if the saddles were glued on the unloaded strand, then there would be a saddle strain of 0.6% which is beyond the measurement capability of the smart saddles. This is a design problem that could not have been predicted prior to the production and development of smart saddles. However, one possible solution is to apply the saddles after the application of the pre-tensioning on the strand which greatly reduces the initial strain in the smart saddle. However, the proposed solution introduces a serious practical application problem in that for safety reasons one cannot operate on the strand when it is subject to load so the operation of gluing the saddles would be risky for the operator.

Excluding possible future automation of this process, which is not the subject of the present research, we propose a possible simple protocol to apply smart saddles on strand. The first step is to apply a modest pre-tensioning load on strand which guarantees that smart saddle positioning on the strand can be done in a safe condition. After smart saddle attachment and before hardening of the glue (curing time) the strand is then tensioned more up to actual level of the load which is preferred for pre-stressing concrete element. This makes it possible to have smart saddles attached on the strand before the pre-tensioning application and in the safe zone for operators and also have available the entire strain capacity for strain monitoring after service load application.

Another problem arises during the installation of smart saddles on strands or concrete casting, wherein the chain of smart saddles becomes sensitive to breakage if appropriate operational rules have not been well considered. In other words, the fiber might be damaged during concrete casting due to a lack of proper curvature for bending and moving the fiber out from the beam. Therefore, to prevent any unintentional fiber breakage, precise bending radius for fibers and appropriate clamping of the fiber chain at specified points are necessary.

Massive smart saddle production for concrete beam monitoring under bending load

In order to evaluate the smart saddle production performance for industrial purposes, an attempt was made to manufacture a large quantity of smart saddles to assess production efficiency and examine how mass production can impact the final product's quality. The objective was to produce 30 smart saddles, which was achieved by three people over the course of one week. The production process involved preparing 10 polyester tissues fixed on the table using tape and then affixing the fiber onto them according to the initial step of the production procedure. This step typically took approximately 6 hours. On another day, the polyester tissues were impregnated with skidder epoxy and wrapped around the plain bar to complete the saddle production. The following day involved cutting the saddles and commencing the first step of the production of the next 10 smart saddles.

Overall, mass production did not require an excessively long time to be completed manually; however, future studies to automate the process using machinery are highly recommended.

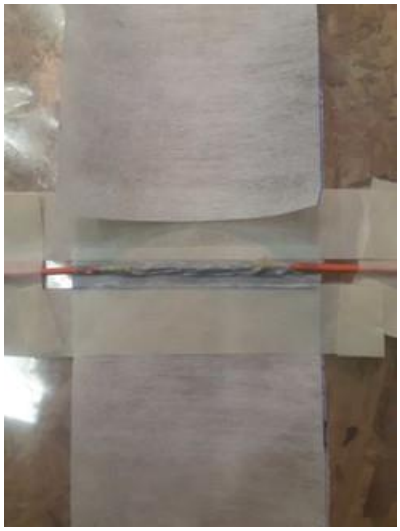

a) FBG + coating gluing to polyester paper

b) Applying the weight

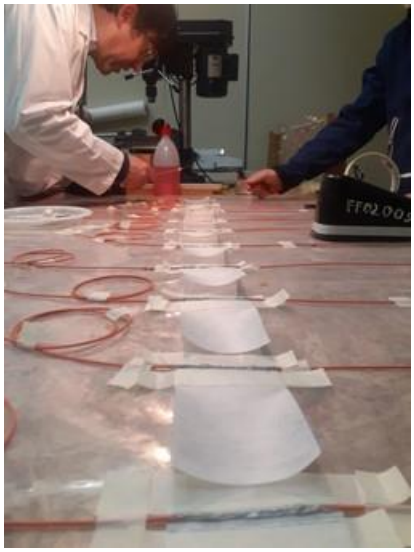

c) Mass production

d) Wrapping polyester paper

e) Wrapped smart saddle

f) Completed smart saddle

Figure 94 . Smart saddle production with coating layer for concrete beam instrumentation

Results summary

Overall, this research introduces a new smart saddle-shaped Fiber Bragg Grating (FBG) embedded element for measuring steel strand strain in steel strand and rebars in prefabricated concrete elements. Three different production procedures were investigated to achieve smart saddles with identical responses to strain loads, differing primarily in accuracy and production speed.

The first production procedure involves embedding FBG sensors in the second layer of tissue impregnated with Sikadur-330 glue, wrapped around the steel strand. This procedure is the basic production procedure. Different tests consisting of thermal, tensile, bending, and vibration tests have been performed on steel strands equipped with smart saddles to investigate the measurement capability of the smart saddle. These preliminary tests prove that smart saddles are able to measure strain variation of the steel strands, but some differences between performance of different specimens have been observed, which served as the basis for improving the production procedure.

The second procedure begins with laying the FBG on polyester tissue with a line of glue, applying 190 gr weight as a pre-tensioning load along the fiber, and then wrapping it around the strand following the previous procedure. The third procedure is similar but with minor modifications for enhanced production speed. For accuracy and performance measurement of the smart saddles produced according to the last procedure, two cyclic tensile tests were applied to 11 samples (8 steel strands and 3 steel reinforcing bars). The first load pattern involves increasing amplitude after every 3 cycles, while the second maintains a constant amplitude. Tensile tests in Roma Tre University revealed that with an improved production procedure, the accuracy of FBG measurements increased, reducing the difference between measurements from 63% to only 4%. Smart saddles produced according to procedure #3 measured strain with acceptable accuracy, but the error between smart saddle measurements increased as the load amplitude increased. This indicates potential damage in the interface glue or smart saddle. Therefore, another tensile test was performed on smart saddles made only with Sikadur-330 resin for both impregnating the polyester paper and the interface glue. In this case, where only Sikadur-330 was used for both production and interface glue, the difference between smart saddle measurements was modest and constant (less than 4%) for all load amplitudes. Results indicate that measurements up to 0.4% are reliable, with some damage occurring beyond this value. Smart saddles produced with Sikadur-330 and attached to the strand with Sikadur-330 are deemed reliable for strain measurements. In fact, strain measurements below 0.2% for rebars and 0.4% for strand are predicted for precise monitoring of elements in correspondence of service limit state. The service limit state is defined to ensure that the tensile stress in concrete remains below the cracking stress (which is typically the mean tensile strength of the concrete for normal concrete). This limit is stricter for pre-stressed concrete, where no tensile stress is permitted in the concrete under service loads. Therefore, it can be concluded that the service limit state is equivalent to the cracking stage in concrete elements while the smart saddles are able to measure strain until rebar yielding which is beyond the service limit State.

A recommended smart saddle length of 7 cm is proposed to adequately include the fiber sensor, necessary fiber parts to avoid excessive bending of the fiber part between the sensor and wire with cover, and part of the fiber wire with cover to ensure a strong connection between the fiber wire and the saddles. Shorter lengths could produce breakage of fiber or disconnection of the fiber wire from saddles, while longer ones may experience non modest bending moments on the saddles and therefore parasite stress that could compromise sensor readings in a deformed concrete beam.

A numerical study has been conducted on a pre-stressed concrete beam to investigate the effect of the number of smart saddles on the accuracy of reconstructed deflection or mode shape of the beam. For this purpose, the concrete beam has been modelled on the OpenseesPy platform under a 4-point bending test to capture strain, deflection, and dynamic characteristics of the beam at different load steps. The attempt is to reconstruct the deformed shape of the beam using strain data at specific points along the beam (integration points). By changing the distance between integration points, the accuracy of the reconstructed deformed shape is compared with the reference shape in terms of percentage. The results revealed that, for that specific beam, a 50cm distance between smart saddles could provide results with acceptable accuracy (around 6%) until the rebar and strand yielding stages.

The investigation brought to light a few issues that arose throughout the elements' industrial production process with consequences on the validation activities. The prototype chains' installation in or on a (actual) industrial prefabricated element is what poses the biggest challenges. This operation must be completed safely, must involve straightforward procedures, and professional workers should not be required for this particular task to reduce time and cost of production. A promising protocol to insert prototype chain of fiber sensor in prefabricated element during industrial production is proposed and discussed.

To assess the production process and quality, smart saddles have been produced in large quantities. It was determined that three individuals are required for the manual production of the smart saddle, and it takes roughly one week to prepare thirty saddles.

References

Anastasopoulos, D., De Smedt, M., Vandewalle, L., De Roeck, G., & Reynders, E. P. (2018). Damage identification using modal strains identified from operational fiber-optic Bragg grating data. *Structural Health Monitoring, 17*(6), 1441-1459.

Anastasopoulos, D., De Wilder, K., De Pauw, B., Nawrot, U., Geernaert, T., De Roeck, G., . . . Reynders, E. (2016). Identification of modal strains of a pre-stressed concrete beam during progressive damage testing. *8th Eur. Work. Struct. Heal. Monit. EWSHM 2016, 1*, 431.

Anastasopoulos, D., Moretti, P., Geernaert, T., De Pauw, B., Nawrot, U., De Roeck, G., . . . Reynders, E. (2017). Identification of modal strains using sub-microstrain FBG data and a novel wavelength-shift detection algorithm. *Mechanical Systems and Signal Processing, 86*, 58-74.

Barrias, A., Casas, J. R., & Villalba, S. (2016). A review of distributed optical fiber sensors for civil engineering applications. *Sensors, 16*(5), 748.

Berrocal, C. G., Fernandez, I., Bado, M. F., Casas, J. R., & Rempling, R. (2021). Assessment and visualization of performance indicators of reinforced concrete beams by distributed optical fibre sensing. *Structural Health Monitoring, 20*(6), 3309-3326.

Broth, Z., & Hoult, N. A. (2020). Dynamic distributed strain sensing to assess reinforced concrete behaviour. *Engineering Structures, 204*, 110036.

Deng, L., & Cai, C. (2007). Applications of fiber optic sensors in civil engineering. *Structural Engineering and Mechanics, 25*(5), 577-596.

Farrar, C. R., Baker, W., Bell, T., Cone, K., Darling, T., Duffey, T., . . . Migliori, A. (1994). *Dynamic characterization and damage detection in the I-40 bridge over the Rio Grande*. Retrieved from

Ferdinand, P. (2014). *The evolution of optical fiber sensors technologies during the 35 last years and their applications in structure health monitoring.* Paper presented at the EWSHM-7th European Workshop on Structural Health Monitoring.

Hong, W., Qin, Z., Lv, K., & Fang, X. (2018). An indirect method for monitoring dynamic deflection of beam-like structures based on strain responses. *Applied Sciences, 8*(5), 811.

Kim, J.-m., Kim, H.-w., Choi, S.-y., & Park, S.-y. (2016). Measurement of prestressing force in pretensioned UHPC deck using a fiber optic FBG sensor embedded in a 7-wire strand. *Journal of Sensors, 2016*.

Kim, J.-M., Kim, H.-W., Park, Y.-H., Yang, I.-H., & Kim, Y.-S. (2012). FBG sensors encapsulated into 7-wire steel strand for tension monitoring of a prestressing tendon. *Advances in Structural Engineering, 15*(6), 907-917.

Kim, S. T., Park, Y.-H., Park, S. Y., Cho, J.-R., & Cho, K. (2014). *Performance evaluation on core wire of smart strand for PSC structures.* Paper presented at the EWSHM-7th European Workshop on Structural Health Monitoring.

Kim, S. T., Park, Y., Park, S. Y., Cho, K., & Cho, J.-R. (2015). A sensor-type PC strand with an embedded FBG sensor for monitoring prestress forces. *Sensors, 15*(1), 1060-1070.

Le, T.-C., Phan, T. T. V., Nguyen, T.-H., Ho, D.-D., & Huynh, T.-C. (2021). A low-cost prestress monitoring method for post-tensioned RC beam using piezoelectric-based smart strand. *Buildings, 11*(10), 431.

Lupi, C., Felli, F., Dell'Era, A., Ciro, E., Caponero, M. A., Kalinowski, H. J., & Vendittozzi, C. (2019). Critical issues of double-metal layer coating on FBG for applications at high temperatures. *Sensors, 19*(18), 3824.

Mita, A., & Yokoi, I. (2000). *Fiber Bragg grating accelerometer for structural health monitoring.* Paper presented at the Fifth international conference on motion and vibration control (MOVIC 2000), Sydney, Australia.

Ndambi, J.-M., Vantomme, J., & Harri, K. (2002). Damage assessment in reinforced concrete beams using eigenfrequencies and mode shape derivatives. *Engineering Structures, 24*(4), 501-515.

Shen, S., Wang, Y., Ma, S.-L., Huang, D., Wu, Z.-H., & Guo, X. (2018). Evaluation of prestress loss distribution during pre-tensioning and post-tensioning using long-gauge fiber Bragg grating sensors. *Sensors, 18*(12), 4106.

Standard, B. (2004). Eurocode 2: Design of concrete structures—. *Part, 1*(1), 230.

Unger, J. F., Teughels, A., & De Roeck, G. (2005). Damage detection of a prestressed concrete beam using modal strains. *Journal of Structural Engineering, 131*(9), 1456-1463.

Uva, G., Porco, F., Fiore, A., & Porco, G. (2014). Structural monitoring using fiber optic sensors of a pre-stressed concrete viaduct during construction phases. *Case Studies in Nondestructive Testing and Evaluation, 2*, 27-37.

Wang, H.-P., Dai, J.-G., & Wang, X.-Z. (2021). Improved temperature compensation of fiber Bragg grating-based sensors applied to structures under different loading conditions. *Optical Fiber Technology, 63*, 102506.

Dissemination of the results and research products

To give adequate publicity to the project, two websites were created, one in the ENEA domain and the second in the web pages of the University of Rome, Department of Architecture.

The ENEA web site address is:

https://www.enea.it/it/progetti/progetti-nazionali/progetto-prefos.html

The main page of the ENEA Prefos project site can be found at this address:

https://architettura.uniroma3.it/ricerca/progetti-di-ricerca/prefos/

Publications in international journals and participation in conferences

Self – monitoring steel strands with FBG sensors technology for industrial production M. Capasso, R. Darban, D. Lavorato, C. Nuti, M.A. Caponero, C. Mazzotta, A. Polimadei, G. Terranova, P. Clemente, C. Failla, S. Signorini, F. Sonzogni. Convegno Luce, Imaging, Microscopia, Spettri di applicazione, LIMS2022 Workshop, ENEA C.R. Frascati (RM), 19-20 maggio 2022, LIMS 2022 Book of Abstracts, p.55

Self – monitoring precast RC beams industrial production with FBG sensors for quality control and real – time monitoring. M. Capasso, R. Darban, D. Lavorato, C.P. Contiguglia, M.A. Caponero, C. Mazzotta, P. Clemente, C. Failla, S. Signorini, F. Sonzogni, C. Nuti. Proceedings of Italian Concrete Conference 2022. Proceedings Aicap ICC 2022 conference, 12-15 October 2022 in Naples and Lecture Notes in Civil Engineering, vol **435**. Springer, Cham. DOI 10.1007/978-3-031-43102-9_48

Strain and vibration measurements by FBG sensors for engineering applications. A. Castaldo, M.A. Caponero, P. Clemente, C. Mazzotta, A. Polimadei, G. Terranova, M. Capasso, R. Darban, D. Lavorato, C. Nuti, S. Signorini, F. Sonzogni, C. Failla. Poster at 6th International Conference Frontiers in Diagnostic Technologies, ENEA C.R. Frascati (Rome), 19-21 October 2022 and 2023 JINST **18** C06030 DOI 10.1088/1748-0221/18/06/C06030

Appendix. A: Apparatus for load application

A steel frame system was designed for the application of the load on the beam in the PRISMA lab. In the new load application system, the jacks/actuators apply the load on the samples based on a displacement-controlled scheme which maximizes safety during the test. Therefore, the design philosophy of the experiment is not only based on controlling the stress in structural elements but also minimizing the deformation of the frame system to maximize the accuracy of the load application and extract any possible unfavorable deformation that can affect the load history application. The perfect experiment design can be defined as a system in which the deformation of the system is zero, with deformation only occurring due to the specimen/sample. However, designing such a system could be expensive. Thus, attempts are made here to provide an acceptable combination of stress control and minimizing deformation in the system.

The system consists of a steel beam (HE320B steel profile) connected to a steel column in the span and connected to the reaction wall on one end. At the other end of the beam, a connection detail is considered for future extension of the beam or adding a column on this side of the beam (Figure 99.a). The actuator can be positioned vertically along the span between the column location and the free end of the beam. The maximum capacity of the actuator (250 kN) is applied to the beam, and static responses (stress and deformations) are obtained using SAP2000 software (.b, c and d). For accurate modeling, the beam and stiffeners are modeled as shell elements, and bolts are considered as uniaxial link elements. Compression-only boundary conditions are considered for the column base and the beam connection to the wall. The beam-column connection is modeled precisely using plates and compression-only links. This detailed modeling makes it possible to calculate the elastic deformation of the system precisely.

Different load application scenarios are also controlled for possible undesirable load application. For the sake of brevity, the detailed calculations are not discussed here, the steel materials are of type S355, and the bolts are of class 8.8 based on the UNI5737 standard. In the following Figures 94, general shape of the system and stress and deformation of the system under load application of maximum capacity of the actuator. The results show that the maximum stress is below the yield stress (fy =355 MPa) and located near beam-column connection bolts while the average stress outside of the bolted area is below 40 MPa. The maximum deflection of the steel T-frame at point which actuator is located is small (about 1.9 mm). Various arrangements of the column location are also controlled, incorporating different possible load application scenarios. Additionally, the T frame will facilitate unobstructed Digital Image Correlation (DIC) readings along the entire beam to capture deformations and cracks. The system geometries are shown in figure 95.

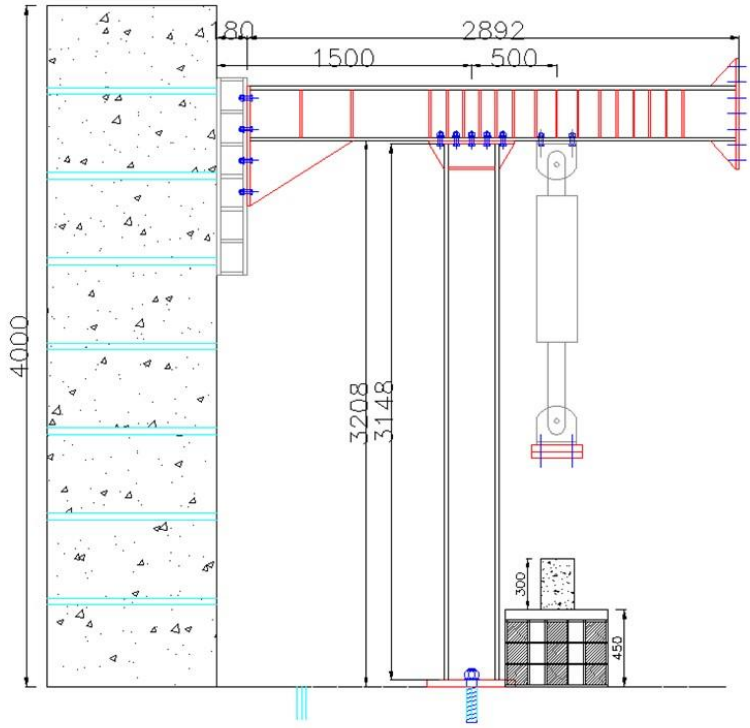

a) Geometry of the steel T-frame system for 4-point bending test (in mm)

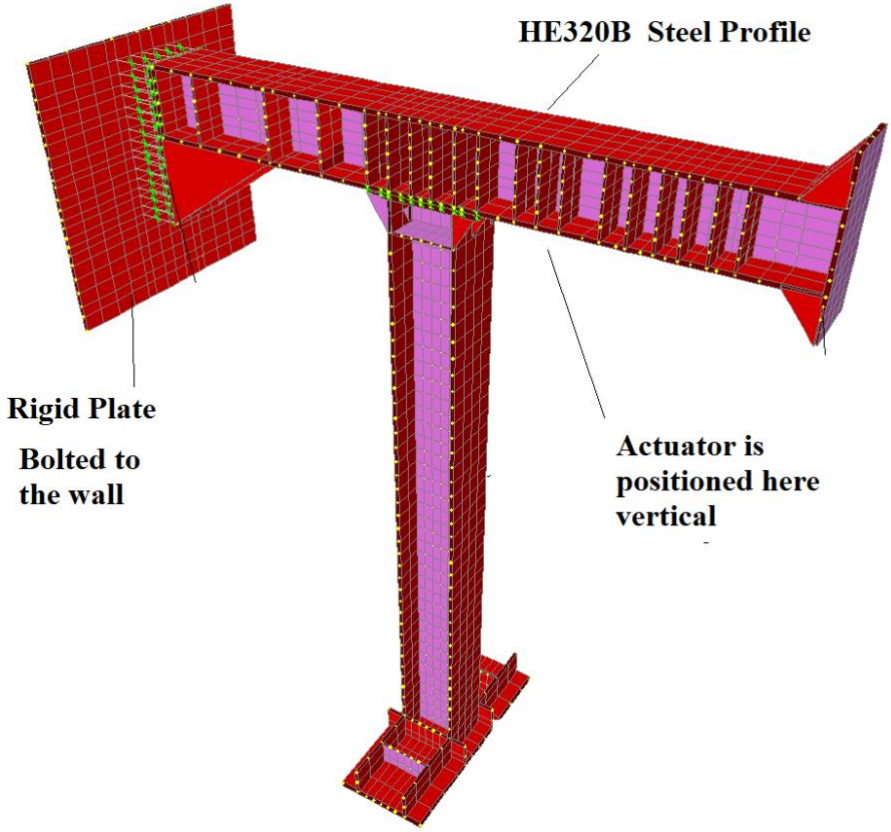

b) Geometry of steel frame system

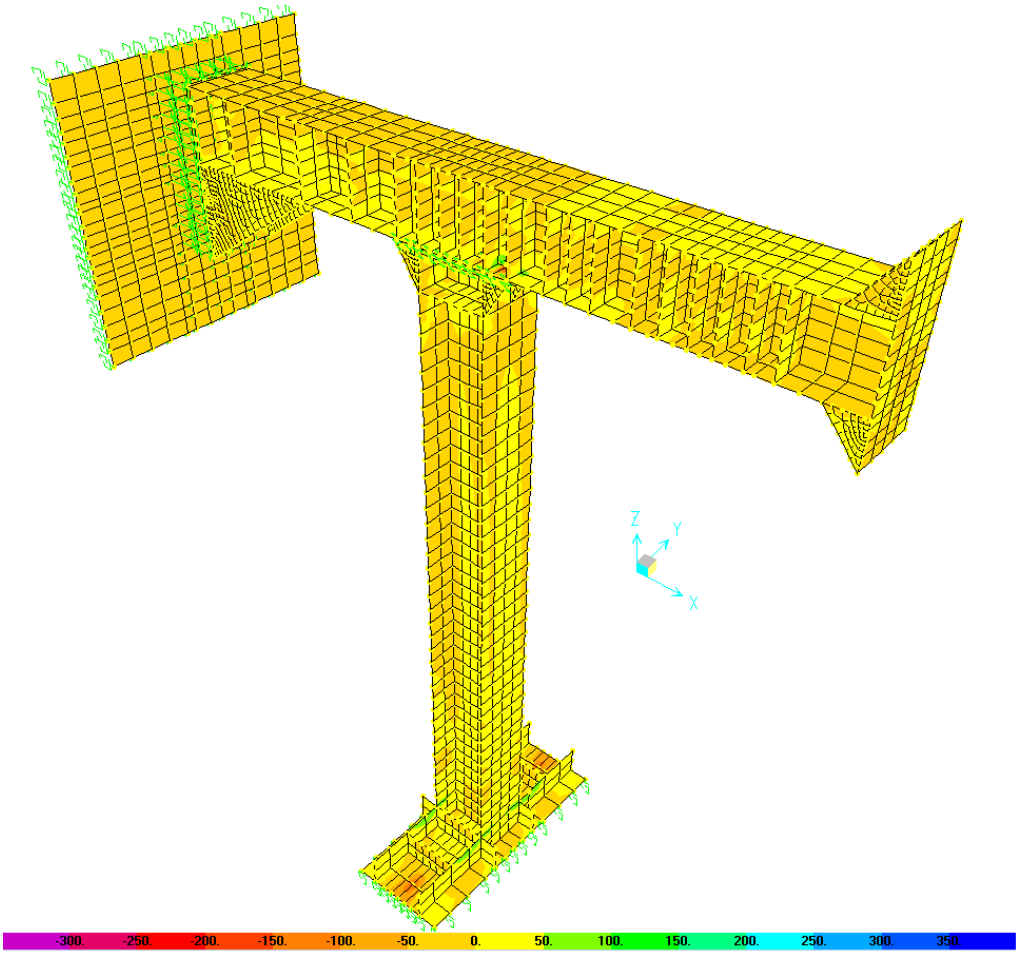

c) Sap2000 F.E.M. model of the frame system: static responses stress in local axes 1 direction (MPa)

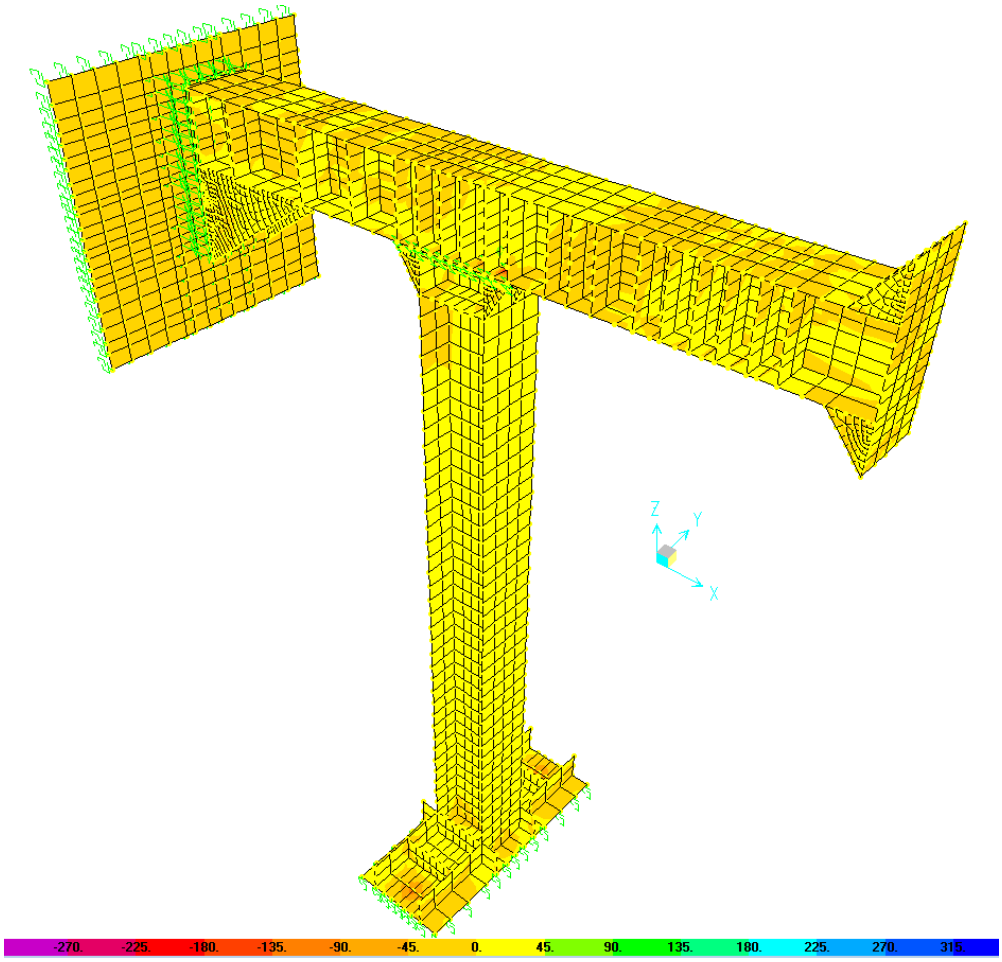

d) Sap2000 F.E.M. model of the frame system: static responses stress in local axes 2 direction (MPa)

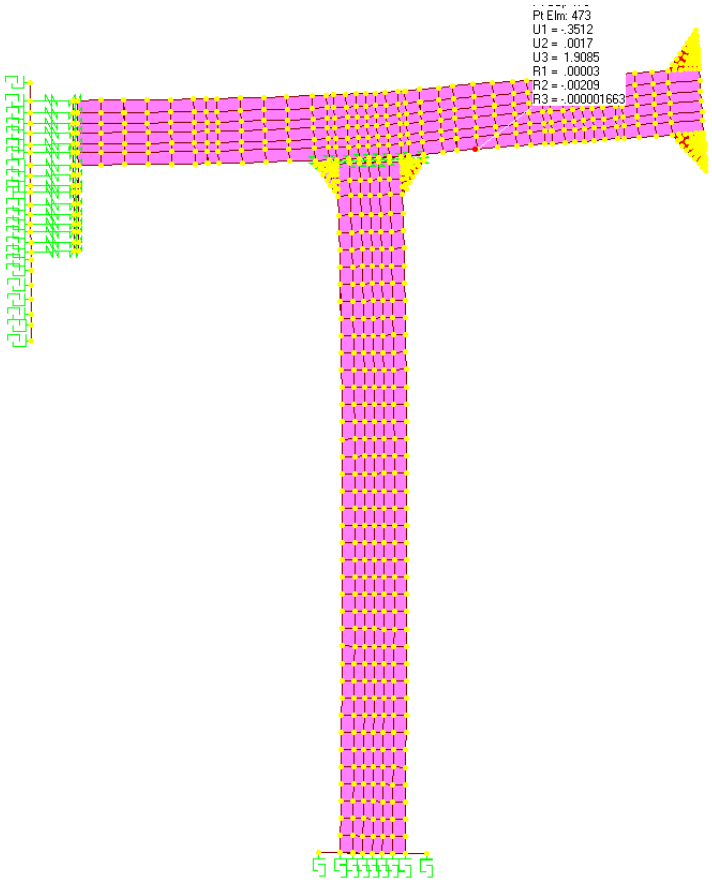

e) Vertical displacement of the system (in mm) under maximum load application of the actuator (250kN)

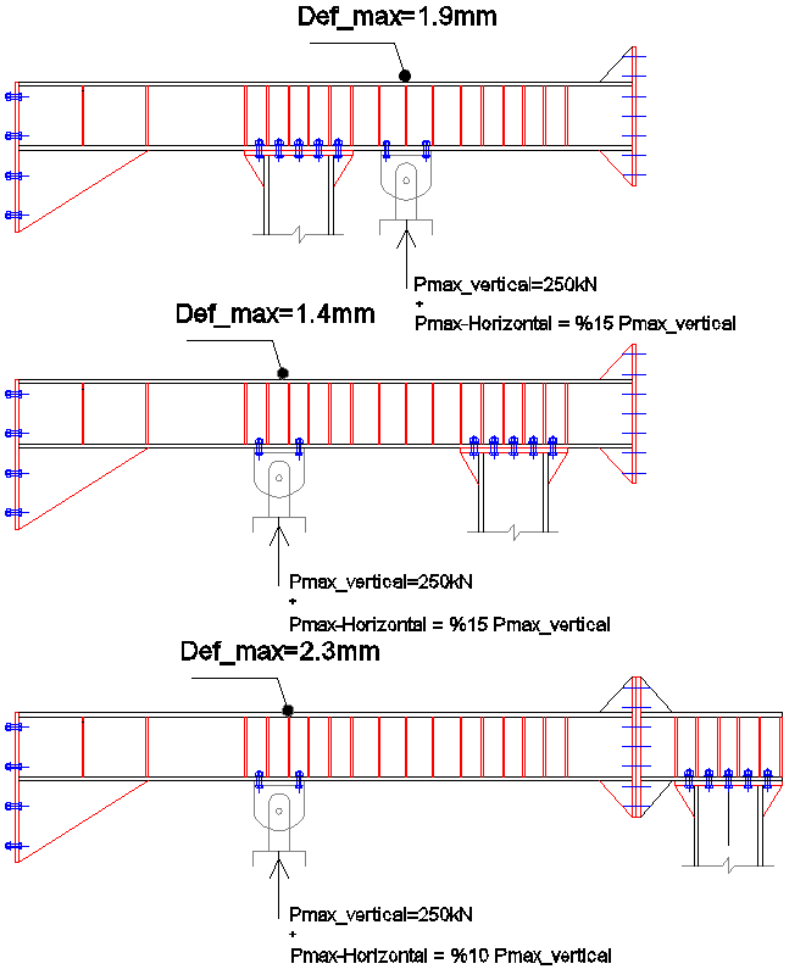

f) Deflection of the system in actuator point for different arrangement of the column-actuator

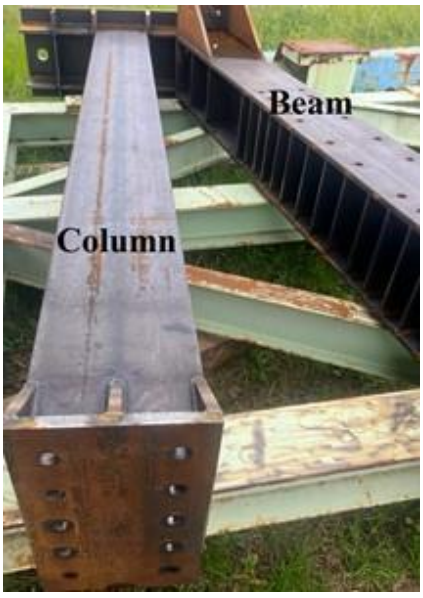

g) Constructed Steel T-frame system

ISBN: 978-88-8286-477-4

enea.it